博 士 学 位 論 文

Study on the Characterization and Grinding
Process of "Soft-and-brittle" Functional Materials

("軟脆" 機能材料の特性評価および研削
加工技術に関する研究)

平成 25 年度

茨城大学大学院理工学研究科

生産科学専攻

杭 偉

Abstract

As a typical multi-functional material, single crystal lithium tantalate ($LiTaO_3$ or LT) exhibits its excellent piezoelectric and pyroelectric properties, and has now found many applications, such as pyroelectric detectors and SAW (surface acoustic wave) substrates. Although LT is known as a very brittle material, however, detailed summaries of its mechanical properties and machinability are not readily available yet. Hence, the objective of this Ph. D thesis is to characterize property of LT crystal and understand its influence on the grinding process.

This Ph. D thesis consists of seven chapters. In chapter 1, the background and objective of this research are addressed. From the mechanical properties point of view, LT crystal has been newly categorized into "soft-and-brittle" materials with the other family members like KDP and CAF_2. The "soft-and-brittle" character makes those materials difficult to be machined by established processes. In order to fulfill the increasing demands of applications for those materials, it is essential to characterize property of LT crystal and understand its influence on the machining process.

Conducted in chapter 2 is a survey of machining technology of functional materials, it can be concluded that most of researches about the fabrication of functional materials focuses on geometry accuracy, sub-surface damage, cutting mode, tool wear and so on. There is none available report about the influence of physical properties on machining process. Hence, one of the objectives in this research is the influence of LT mechanical and physical properties on its machining process.

Aiming to determination of the mechanical property of LT, a new robust data analysis procedure is proposed in Chapter 3 for indentation tests. Following this data analysis procedure, the mechanical properties of materials can be computed accurately at $\mu N \sim mN$ range of load which is essential for "soft-and-brittle" materials like LT.

In order to clarify and understand the fundamental mechanical properties of LT, micro/nano indentation tests are then conducted in the chapter 4 to evaluate its mechanical properties. The obtained results are also used to categorize the functional materials, to understand LT's behaviors in elastic, plastic (ductile) and brittle regimes and to analyze the influences on their machinability in the machining process.

In the chapter 5, a wafer grinding model is firstly established for the analysis and calculation of specific energy of material removal and the distribution of grinding force. A series of grinding experiments were carried out on $LiTaO_3$ and Si for the evaluation of specific energy of material removal. After discussed in association

with results of indentation, it is found that the hardness of LT is only 83% of Si, however, the specific energy of LT is 147.46 J/mm^3 and 44% larger than that of Si which had well agreed with the indentation results. Both the grinding and indentation results indicated a fact that LT is so brittle that no or very limited extra energy was demanded to make the cracks propagate once the crack was initiated, while a certain extra energy was required for Si. The calculation results indicated a fact that the grinding force of LT is larger than that of Si at the same distance from the center of wafer. The increasing rate of consumed power played a very important role in the machining of LT. Compared with the grinding results of Si, the increasing rate in the LT grinding experiments had a linear relationship with the increase of feed rate at the same experimental conditions which indicated a fact that the physical properties may play a more important role in the grinding process.

The content of chapter 6 is firstly focuses on the physical properties of LT like piezoelectric and pyroelectric effects and their influences on grinding performance. In order to suppress the piezoelectric and pyroelectric effects induced by polarization during grinding of LT, control of coolant temperature and use of electrolyte solution are also purposely were tried in this chapter. The results suggest that the physical properties of LT could be the main factors which dominate the grinding process.

Given in chapter 7 is the summary of this thesis.

Contents

Chapter 1 Introduction

1.1 Introduction of Lithium tantalite (LiTaO$_3$ or LT)

Compared with single crystalline silicon (Si) which is the traditional core material of semiconductor, Lithium tantalite (LiTaO$_3$ or LT) has recently drawn considerable attentions because of its unique characteristics, such as optical, piezoelectric and ferroelectric properties [1].

Unlike covalently bonded silicon crystalline, as shown in Fig. 1.1 and Table 1.1, LT takes triangular space group R3c ion bonding structure, and presents strong anisotropic aspect. In the paraelectric phase above the Curie temperature, the Li atoms lie in an oxygen layer that is c/4 away from the Ta atom, and the Ta atoms are centered between oxygen layers. It is known that three cleavage planes in LT crystal are; $(01\bar{1}2)$, $(1\bar{1}02)$ and $(\bar{1}012)$. LT are thus presents much different characters from Si for the difference of interatomic bonding. As the results, LT seems much more brittle and softer than Si. With a comparison of silicon shown in Table 1.1 [2, 3], LT exhibits unique electro-optical, pyroelectric and piezoelectric properties combined with a wide transparency range and high optical damage threshold. These properties make LT well-suited for numerous applications including electro-optical modulators, pyroelectric infrared detectors, surface acoustic wave (SAW) substrates and piezoelectric transducers etc.
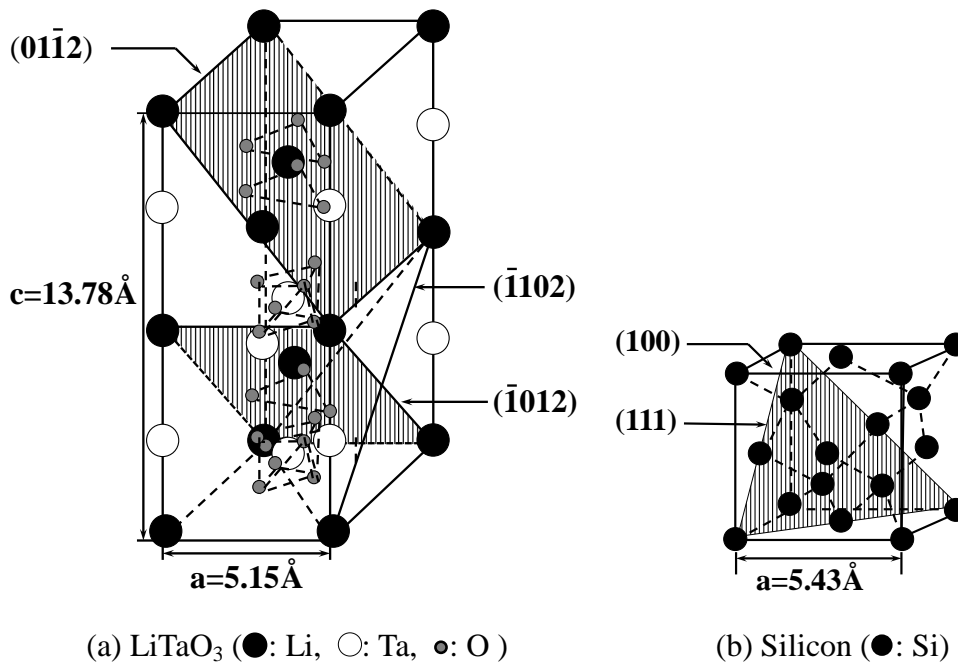

(a) LiTaO$_3$ (●: Li, ○: Ta, ◓: O)   (b) Silicon (●: Si)

Fig. 1.1 The crystal structure of LiTaO$_3$ (a) and Silicon (b)

Table 1.1 Summary of properties for LT and Si

	LiTaO$_3$	Silicon
Density (g/cm^3)	7.45	2.33
Crystal symmetry	Triangular space group 3m	Diamond cubic
Lattice spacing (nm)	a=0.515 c=1.378	a=0.543
Melting point (°C)	1650	1414
Thermal conductivity(mW/cm°C)	46	1300
Poisson ratio v	0.25	0.22-0.28
Electro-optic coefficients pm/V @633 nm, high frequency	r_{33}=33 r_{22}=20 r_{13}=8	-
Piezoelectric strain constant (*10^{-11} C/N)	d_{22}=2.4 d_{33}=0.8	-
Pyroelectric coefficient (10^{-6} *C*m^{-2} *K^{-1})	-230	-
Solubility	Insoluble in water	

Electro-optic modulator (EOM) is an optical device which is used to modulate a beam of light. Depending on the device configuration, the following properties of the light wave can be varied in a controlled way: phase, polarization, amplitude, frequency, or direction of propagation. Modulation bandwidths extending into the gigahertz range are possible with the use of laser-controlled modulators [4].

Such materials like LT changes its optical properties when it is subjected to an electric field resulted from electrodes. This change is caused by forces that distort the positions, orientations, or shape of the molecules of LT. The electro-optic effect which is defined by the electro-optic coefficients is variable in accordance with the refractive index of LT resulting from applied electric field.

Shown in the Fig. 1.2 is the schematic illustration of EOM. The simplest EOM consists of a crystal, like LT, whose refractive index can be controlled by the local electric field. That means that if LT is exposed to an electric field, light speed can be changed when the light goes through the waveguides on the LT surface. As the phase of the light leaving the crystal is directly proportional to the period of time for light to pass through LT waveguide, therefore, the phase of the laser light through an EOM can be controlled by changing the electric field in the crystal.
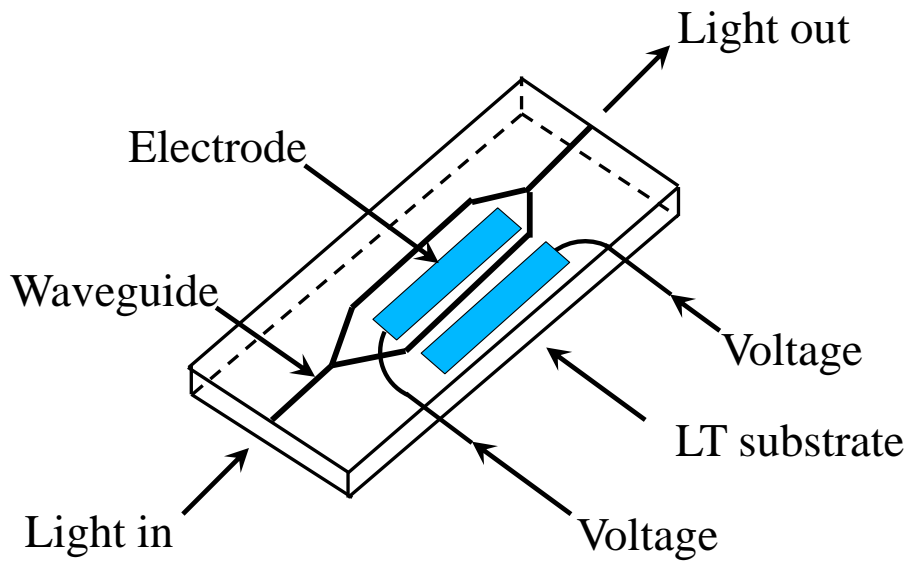
Fig. 1.2 The schematic illustration of Electro-optic modulator

The electric field can be created by placing a parallel plate capacitor across the crystal.　The phase modulation depends linearly on the index of refraction, which in turn depends on the electric field inside the paralleled plates, or the potential applied to the EOM.

Shown in the Fig. 1.3 is configuration of Pyroelectric Infrared Detectors (PIR). PIR is a device which convert the changes in incoming infrared light to electric signals.　Pyroelectric materials are characterized by having spontaneous electric polarization, which is altered by temperature changes when infrared light illuminates the pyroelectric elements [5].

　When light radiation (LR) is applied to a thin LT crystal (thickness<40μm), its temperature increased. Turning on the light radiation an electrical charge is generated

Fig. 1.3 The configuration of Pyroelectric infrared detectors

by heating, turning off the light radiation the crystal cools down and an opposite charge is generated. These very small electrical charges are generally converted within the de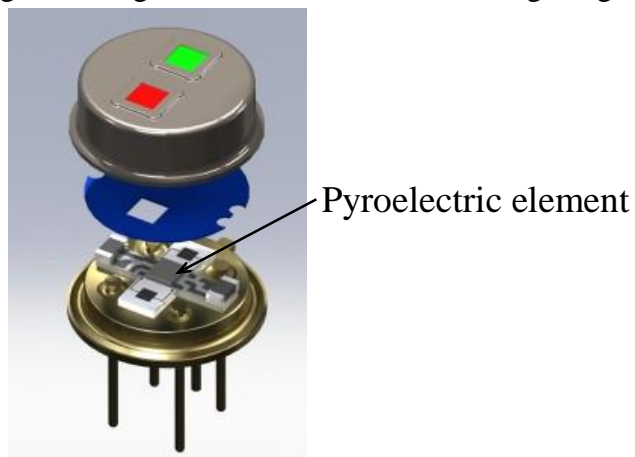tector to voltage signal by use of extremely low noise and low leakage Field Effect Transistors (FET) or CMOS operational amplifiers.

A LT detector can be used with long term stability to very exactly measure infrared radiation (IR).   As the pyroelectric element reacts to a change of the IR, the detector must always be used with a modulated radiation source. Since LT detectors operate on a thermal phenomenon they have a very broad spectral response - between 100 nm to over 1000 μm without any cooling like other semiconductor detectors. Most common applications are motion detection, NDIR gas analysis, flame detection with spectroscopy and radiometry also possible.   Pyroelectric detectors are able to measure signals up to several kHz with high performance.

Interdigital Transducer (IDT)

Piezoelectric effect substrate (LT)

Surface acoustic wave generated and moving either direction of wafer
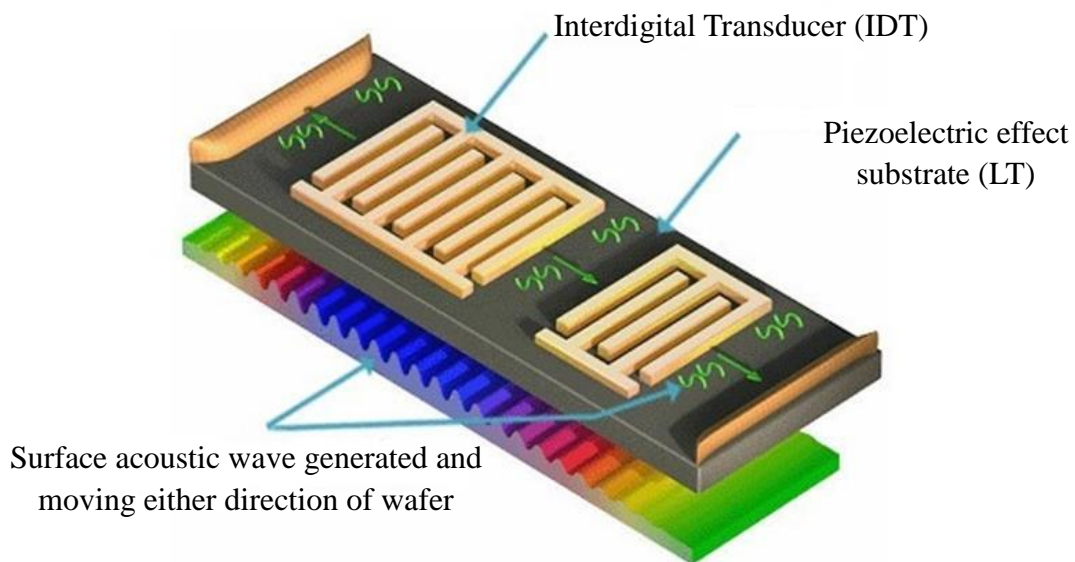
Fig. 1.4 The structure of surface acoustic wave filter

Surface acoustic wave (SAW) filters are the dominant technology for RF front-end filters in almost all wireless phones.   Shown in the Fig. 1.4 is the structure of surface acoustic wave filter.   As shown in Fig. 1.4, SAW devices generate and detect surface acoustic waves using interdigital transducers (IDT) on the surface of a piezoelectric effect substrate. In this way, the pitch, line width as well as the thickness of substrate is the main factors determining the center frequency of the filter and the shape of the passband.   Nowadays, the LT substrate is the main choice for such substrate.   For this reason, thinner LT wafer associated with high surface quality are increasingly demanded by wireless communication industry [6].

Fig. 1.5 The configuration of a piezoelectric transducer

The Fig. 1.5 is the configuration of a piezoelectric transducer. As shown in Fig. 1.5, a piezoelectric transducer is a device which transforms one type of energy to another by using of 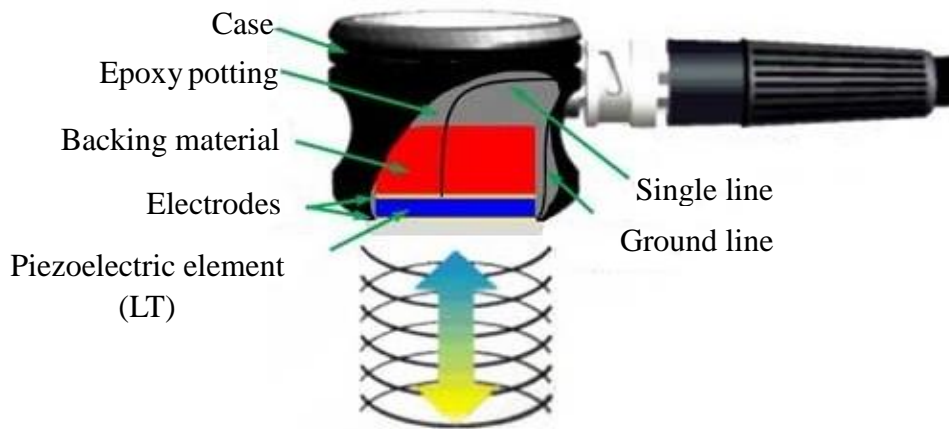the piezoelectric effects of certain crystals like LT. When a piezoelectric material such as LT is subjected to stress or force, it generates an electrical potential or voltage proportional to the magnitude of the force. This makes this type of transducer ideal as a converter of mechanical energy or force into electric potential. A piezoelectric transducer is also able to convert the electric energy to mechanical energy if it is used reversely [7].

The high sensitivity of piezoelectric transducers makes them useful in microphones, where they convert sound pressure into electric signal, in precision balances, in accelerometers and motion detectors for ultra-fast response. They are also used in non-destructive testing and in many other applications requiring the precise sensing of motion or force [8].

The piezoelectric effect also works in reverse, in that a voltage applied to a piezoelectric material will cause that material to bend, stretch, or otherwise deformation. This deformation is usually very slight and proportional to the voltage applied, and such inverse effect offers a method of precision movement on the micro scale. A transducer may, therefore, be used as an actuator for the exact adjustment of fine optical instruments, lasers, and atomic force microscopes.

1.2 Summary of available machining process

Though LT has a numerous applications resulted from its unique characteristics, however, little work has been carried out on its fabrication or machining process. According the literature survey, only the chemical-mechanical-polishing (CMP) has

been use to machining LT.

Chemical-mechanical polishing (CMP) has originally emerged as a key technology for deep-submicron integrated circuit (IC) device manufacturing to achieve both local and global planarity of Si wafer surfaces. CMP has been routinely applied to planarize the inter-level dielectric (ILD) and the damascene metallization process for photolithography of silicon[9].

Only report on CMP was made by Wei who has applied this machining process [10]. She reported that the surface roughness of LT could be less than 5 nm by CMP under a suitable test condition. However, the obvious shortcomings like low machining efficiency and bad profile accuracy with the work-piece size increased restrain its application.

Because there is none report about the machining process of LT except CMP. Hence, according to the similar mechanical properties, the view is focused on the machining of other family member like potassium dihydrogen phosphate (KDP) and CaF_2. Namba [11] reported that KDP inorganic optical crystal for laser fusion was machined by single point of diamond turning (SPDT), and a super-smooth surface with the roughness of 1.09nm (RMS) was obtained. Meanwhile, Tie [12] reported that the surface roughness of KDP crystals by single point diamond turning technique can be achieved at 0.86 nm. However, the procedure of single point diamond turning isn't really suited for mass production due to its tool wear and low productivity. Though the influence of orientation is introduced by Zhao [13], however, most of the current researches focuses on the achievement of good surface geometry of work-piece. There is none report about the influence of physical properties on machining process. The detailed literature survey is presented in chapter 2.

Literature shows that the research works about the machining of CaF_2 are also limited. Only Yan [14] reported that continuous chips and ductile-cut surfaces with nanometric roughness were generated by diamond turning at a feed rate of 1 μm/min by a tool with appropriate negative rake angle under dry cutting conditions. The surface roughness R_a is 2.4 nm.

As far as the knowledge the author had, the available machining processes for LT and similar functional materials are still limited. Meanwhile, the available machining processes are yet good enough to fulfill the increasing requirement of these "soft-and-brittle" materials. Hence, LT is chosen as the typical material for "soft-and-brittle" materials in this thesis to study its mechanical and physical properties, and their influences on machining process.

1.3 Research objective

As a typical multi-functional single crystal material, LT has recently drawn considerable attentions because of its excellent properties and wider application. However, little work has been carried out for its machining process. Its mechanical properties including the hardness, elastic modulus and fracture toughness are still not very clearly until now. Foremost, because of its inherent properties for example low hardness and fracture toughness, the cracks are very easily to generate on the LT surface during the machining process, and resulted in the wafers broken. In order to solve these problems, the research objectives are shown as follows:

(1) Characterization of LT and other the traditional hard-and-brittle materials according to their mechanical properties.

(2) Research on the influence of LT mechanical and physical properties on its machining results.

1.4 Thesis strategy and structure

This dissertation is to characterize $LiTaO_3$ and to understand the influence of properties on the machining process. The structure of the dissertation is arranged with the following contents:

- In chapter 1, the introduction and background of this research are illustrated. As a typical "soft-and-brittle" function material, LT is chosen for current study. The literature survey about available machining methods of LT, KDP and CaF_2 reveals that the available machining processes for these materials are still limited and not good enough to fulfill the increasing requirement.

- The literature survey about the machining process of functional materials is illustrated in chapter 2. From the results obtained in this chapter, it can be concluded that most of the current researches focuses on the geometry accuracy, sub-surface damage, cutting mode, tool wear, the influence of orientation on machining. There is none report about the influence of physical properties on machining process. Hence, one of the main objectives in this research is given to study the influence of LT physical properties on its machining process.

- Aiming to determining the mechanical property, a new robust data analysis procedure is proposed in Chapter 3. The basic mechanical properties like elastic

modulus and indentation hardness strongly depend on the contact stiffness, the contact area and the accuracy with which they are determined. Firstly, described in this chapter was a comparison of three approaches to estimate the contact stiffness. From the experimental results, it is concluded that the contact stiffness computed from the curve fitting method is most reliable and robust. Subsequently in this chapter, a new procedure for computation of the contact area was proposed by use of multivariable estimation via a least square fitting. Finally, indentation tests on silicon and aluminum were conducted to verify that the proposed procedure is not only valid for a variety of materials from hard-brittle to soft-ductile, but also robust and applicable to indenters with imperfect geometry. Following this data analysis procedure, the mechanical properties of typical brittle materials can be computed and usable for the analysis of material characterization in the next chapter.

- In order to clarify and understand the fundamental mechanical properties of LT, micro/nano indentation tests are conducted in the chapter 4 to evaluate elastic modulus, hardness and fracture toughness. Other two typical single crystals of silicon and sapphire are chosen for comparison. For most materials including metals, ceramics, crystals and amorphous, the hardness was found to have a simple power law relation with the elastic modulus and described as $H=E^n$. The power n is introduced as a new index which can be used to not only rank those materials in an order of hardness, but also categorize materials into groups of "ductile" or "brittle". Subject to the new index n and fracture toughness K_{IC}, the "brittle materials" are able to be further classified into two sub-groups. Sapphire who have $1 < K_{IC} < 10$ and $0.5 < n < 0.7$ belong to "hard-and-brittle" materials, whereas LT can be characterized as a new category of "soft-and-brittle" materials with $K_{IC} < 1$ and $0.2 < n < 0.5$. Silicon crystal fell at the boundary of these two sub-groups. The obtained results are also analyzed and discussed to understand their behaviors in elastic, plastic (ductile) and brittle regimes and the influences on their machinability in the machining process in this chapter.

- In the chapter 5, a wafer grinding model is firstly introduced. The theoretical analysis to calculate the specific energy of material removal and grinding force are subsequently proposed following this grinding model. After the theoretical analysis, the grinding experiments for silicon and LiTaO$_3$ were carried out on the precision machine UPG-150 with SD3000 diamond grinding wheel. After discussed in association with results of indentation, it is found that the hardness of LT is only 83% of Si, however, the specific energy of LT is 147.46 J/mm^3 and

44% larger than that of Si which had well agreed with the indentation results. Both the grinding and indentation results indicated a fact that LT is so brittle that no or very limited extra energy was demanded to make the cracks propagate once the crack was initiated, while a certain extra energy was required for Si. The calculation results indicated a fact that the grinding force of LT is larger than that of Si at the same distance from the center of wafer. The increasing rate of consumed power played a very important role in the machining of LT. When it was above critical line, cracks were initiated and resulted in wafer broken. Compared with the grinding results of Si, the increasing rate in the LT grinding experiments had a linear relationship with the increase of feed rate at the same experimental conditions which indicated a fact that the physical properties may play a more important role in the grinding process.

- The theoretical analysis about the influence of physical properties on the crack initiation is firstly presented in chapter 6. The theoretical results suggested that the physical properties like pyroelectric and piezoelectric effect may play more important role than its mechanical properties in crack initiation and propagation on LT surface. For $LiTaO_3$, the cracks are possible to generated by the inner stress resulted from piezoelectric reverse effect and grinding wheel. Because it is rich in plasticity, LT demands larger specific energy for material removal. As the most machining energy is eventually converted into heat, LT undergoes a rapid rise in temperature during the grinding process, thus highly risks in thermal shock. As a kind of typical pyroelectric and piezoelectric material, electric charge is very easily accumulated in the change of temperature during the grinding process and stress from grinding wheel. Eventually, the cracks were initiated by joint interaction between piezoelectric reverse effect and mechanical stress. Following the theoretical analysis about the influence of physical properties on the grinding performance, the grinding tests about how to suppress the influence of physical properties on machining results were also carried out in this chapter. In order to suppress the change of temperature on the grinding process of $LiTaO_3$, the effective cooling methods were investigated in this chapter. Subsequently the research on suppression of the spontaneous polarization effect on LT surface by use of the electrolyte coolant in the grinding experiments was also carried out.

- In the chapter 7, the conclusions of this dissertation are summarized.

References

[1] V. Rastogi, P. Baldi and I. Aboud: "Effect of proton exchange on periodically poled ferroelectric domains in lithium tantalite", *Optical Materials*, Vol.15, Iss.1, (2000), pp.27-32.

[2] Information on: http://www.almazoptics.com/LiTaO$_3$.html

[3] Information on: http://design.caltech.edu/Research/MEMS/siliconprop.html

[4] Information on: http://en.wikipedia.org/wiki/Electro-optic_modulator.

[5] Information on: http://www.eoc-inc.com/pyroelectric_detectors.htm.

[6] Information on: http://www.google.com.hk/imgres?grefurl=http://itf.co.kr/tech/ /tech/image/sub3_2.GIF

[7] Information on: http://www.ndt-ed.org/EducationResources/CommunityCollege/ Ultrasonics/EquipmentTrans/piezotransducers.htm.

[8] Information on: http://www.ndt-ed.org/EducationResources/CommunityCollege/ Ultrasonics/EquipmentTrans/piezotransducers.htm

[9] Slurries Nathan C. Crawforda, S. Kim R. Williamsb, David Boldridgec *et.al:* "Shear thickening and defect formation of fumed silica CMP slurries", *Colloids and Surfaces A: Physicochemical and Engineering Aspects,* 436 (2013), pp.87– 96

[10] Wei xi, "Research on the chemical mechanical polish on LiTaO$_3$ wafer", *Master thesis*, (2004), Guangdong University of Technology.

[11] Yoshiharu Namba，Masanori Katagiri，Masahiro Nakatsuka："Single point diamond turning of KDP inorganic nonlinear optical crystals for laser fusion", *Journal of the Japan Society of Precision Engineering*, Vol.64 Iss.10, (1998), pp.1487-1491.

[12] Guipeng Tie, Yifan Dai, Chaoliang Guan *et.al* : "Research on subsurface defects of potassium dihydrogen phosphate crystals fabricated by single point diamond turning technique", *Optical engineering*, Vol.52, Iss. 3, (2013), p.1–6.

[13] Qingliang Zhao, Yilong Wang, Guang Yu, *et.al*: "Investigation of anisotropic mechanisms in ultra-precision diamond machining of KDP crystal", *Journal of material processing technology*, Vol.209, (2009), pp.4169-4177.

[14] Jiwang Yan, Jun'ichi Tamaki, Katsuo Syoji , Tsunemoto Kuriyagawa: "Single-point diamond turning of CaF_2 for nanometric surface", *International Journal of Advanced Manufacture Technology,* Vol. 24, (2004), pp. 640–646.

Chapter 2 Literature review of the machining process of functional materials

Several machining procedures like cutting, grinding and polishing have been successfully used in the fabrication of functional materials like ductile and brittle materials.   Hence, a literature survey of machining process of functional material is conducted in chapter 2.

2.1 Cutting

Nowadays, turning method especial single point diamond turning (SPDT) is widely used in the fabrication of mirror-quality surfaces of functional materials. Diamond turning is a multi-stage process. Machining processes are carried out by using a series of CNC lathes.   Shown in Fig. 2.1 is an external view of SPDT lathe [1].

From the literature survey, it is found that that SPDT is mainly applied to machine those ductile materials like Aluminum.   The Fig. 2.2 is measurement of diamond turned Al surface reported by Hamilton [2]. As shown in Fig. 2.2, it was found that an extremely smooth Al surface with roughness R_a of 0.66nm and RMS of 0.82nm was achieved by SPDT.

For the fabrication of brittle materials, not only the geometry accuracy but also cutting mode has been attracted enough concerns from researchers.   And the cutting mode is determined by the relationship between the given depth of cut (DOC) and
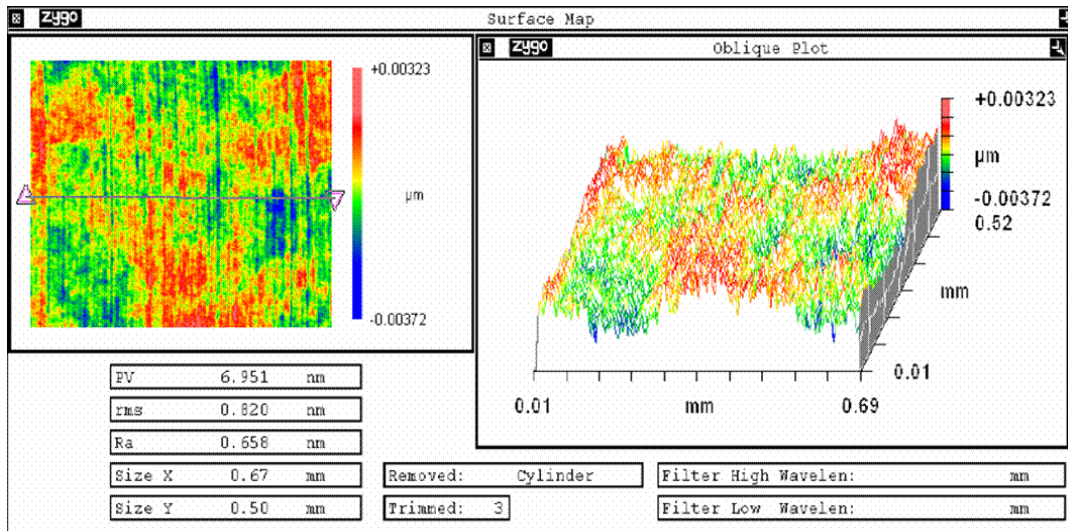

Fig. 2.1 The external view of SPDT lathe

Fig. 2.2 The measurement of diamond turned Al surface

critical DOC of material.

For most "hard-and-brittle" materials, the critical cutting depth d_c is predicable by Bifano's formula [3]:

$$d_c = \beta \frac{E}{H}\left(\frac{K_{IC}}{H}\right)^2 \tag{2.1}$$

Where β is constant subjected to material and takes β= 0.15-0.16 for most "hard-and-brittle" materials [4]. E, H and K_{IC} refer to elastic modulus, hardness and fracture toughness respectively.   The Fig. 2.3 is the SEM topography of machined area of ductile regime, ductile to brittle transition and brittle regime.   As shown in Fig. 2.3 [5], the depth of cut (DOC) stands for how deep the tool is engaged into the work-piece.   From the current researches about brittle materials like silicon, it can be
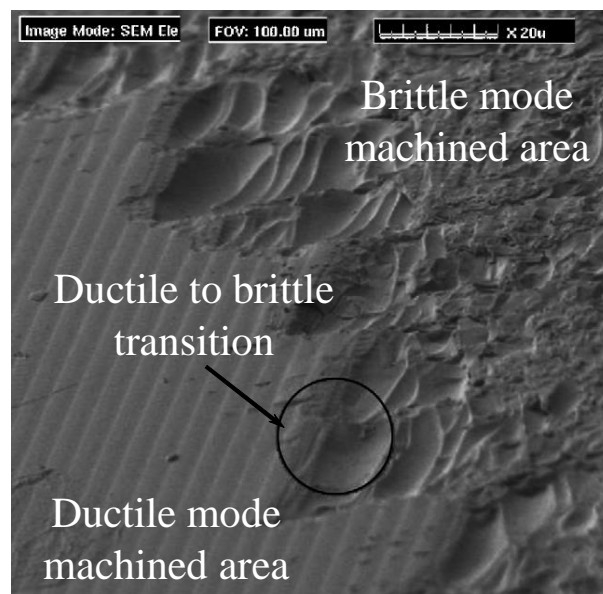

Fig. 2.3 The SEM topography of machined area of ductile regime, ductile to
brittle transition and brittle regime

13

concluded when DOC doesn't exceed the critical depth of cut which is determined by properties of individual material, then cutting can be controlled in the ductile mode. As shown in Fig. 2.3, when the area is cut in ductile mode, a series of cutting marks can be clearly observed and good surface finish can be achieved. And a few fractures appear when the increased DOC is around critical depth of cut. This mode is in transition from ductile to brittle machining. Finally, when the DOC is increased above the critical depth of cut, this surface is machined at brittle mode, where cracks are initiated.

As well as machining mode, the material property also has an influence on the machining performance. In order to clarify the influence of material properties on cutting performance, a series of diamond cutting experiments were carried by Zhao [6]. The Fig. 2.4 is the variation of cutting force on different crystal planes. From the Fig. 2.4, it is noted that cutting force has an obvious variation under the same test condition. The only difference in cutting is difference of orientation of work-piece.
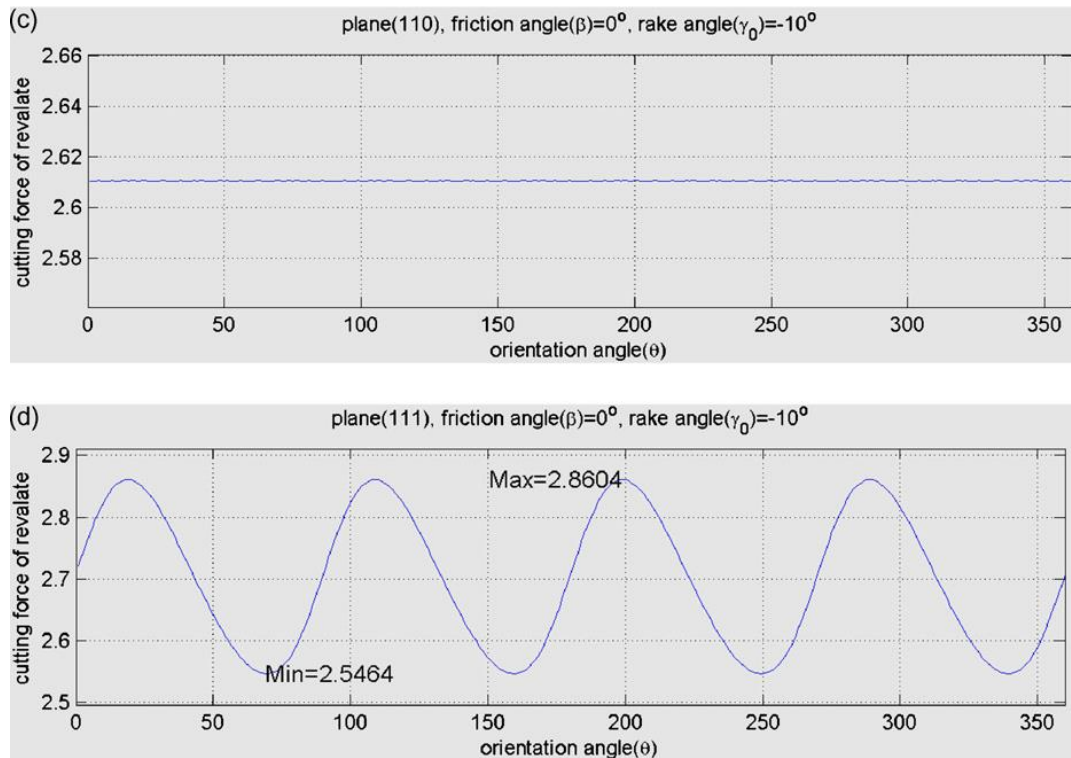

14
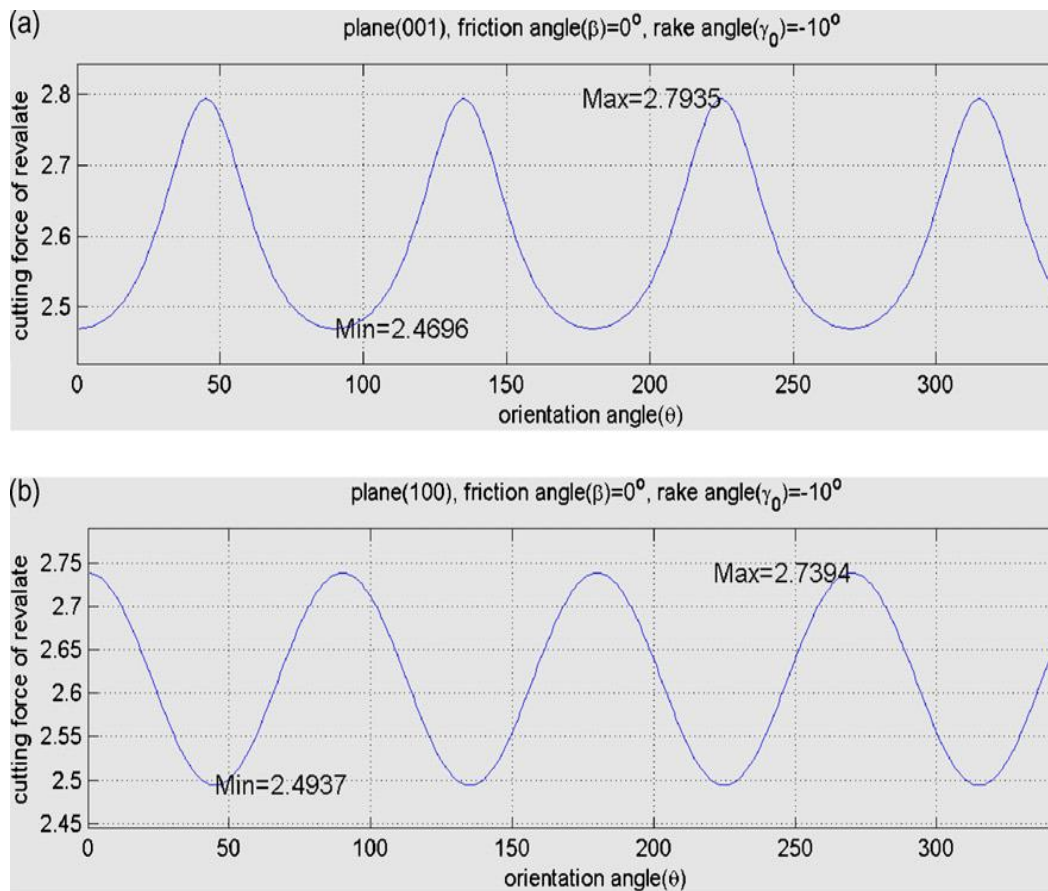
Fig. 2.4 Variation of cutting force on different crystal planes (a) (001) crystal plane, (b) (100) crystal plane, (c) (110) crystal plane, and (d) (111) crystal plane.

It can be concluded that material anisotropy has an effect on the cutting performance.

The Fig. 2.5 is tool wear land on the rake face and flank face. As shown in Fig. 2.5 [5], during the cutting process, the friction and temperatures between the diamond tool and work-piece increased and contributed to enlarge wear land on both rake face and flank face of cutting tool.

The Fig.2.6 (a) and (b) are the diamond cutting of silicon performed at ductile and brittle mode reported by Yan [7]. Firstly, brittle mode cutting was performed at an undeformed chip thickness of 900 nm under dry condition. Fig. 2.6 (a) showed that a SEM photograph after cutting by a diamond cutting tool for 7.62 km. The entire edge has been covered with micro-chipping which are a few micrometers in size. Next, ductile mode cutting was performed at an undeformed chip thickness of 90 nm. Fig. 2.6 (b) is an SEM photograph of diamond cutting tool after cutting for 7.62 km. The wear lands on both rake and flank faces. Tool radius is covered with numerous micro grooves oriented along the cutting direction and a step structure can be observed on the wear land. This phenomenon indicates that the several tool wear occurred at both brittle and ductile cutting mode.

The phenomenon of diamond tool wear also reported by Goel [8], on diamond turning of single crystal 6H-SiC at a cutting speed of 1 m/s with an ultra-precision diamond lathe machine, to elucidate the microscopic origin of ductile-regime
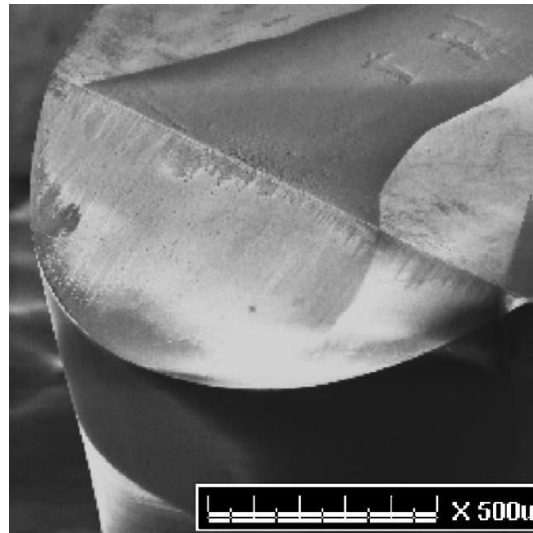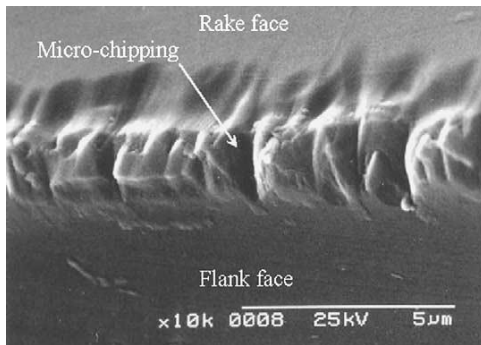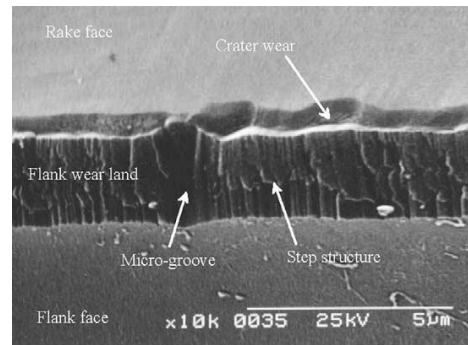
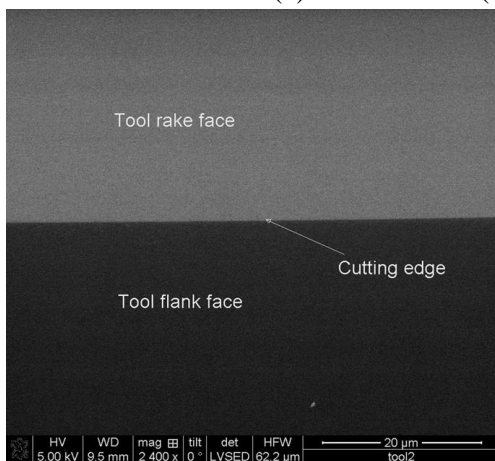Fig. 2.5 The tool wear land on the rake face and flank face

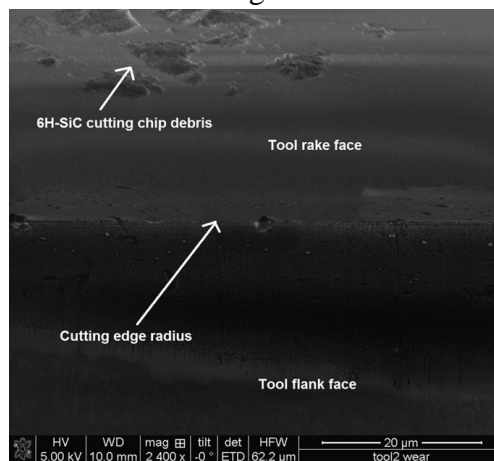(a)Brittle mode   (b) Ductile mode

Fig. 2.6 SEM photographs of the cutting distance of 7.62 km after
(a) brittle mode (b) ductile mode cutting

(a) Before cutting   (b) After cutting distance of 1 km

Fig. 2.7 The SEM topography of diamond tool (a) before cutting and (b) after
cutting distance of 1km

machining.   The Fig. 2.7 (a) and (b) are the SEM topography of diamond tool (a) before cutting and (b) after cutting distance of 1km.   It can be seen that before cutting, the cutting edge was extremely sharp and both tool flank face and tool rake face were prepared extremely fine without any visible wear marks on the edge or the surface of the tool.   Fig. 2.7(b) shows the SEM image of the diamond tool on the same magnification after 1 km of cutting length.   It can be seen that the cutting tool has started to show wear marks on the flank face and the edge radius has started to lose its sharpness. In some areas recession of the cutting edge is also visible. Besides recession of the cutting edge, significant wear marks on the tool flank face can also be seen.

As a conclusion based on this section, turning of functional materials mainly focuses on geometry accuracy, machining mode, the influence of functional material's orientation on its machining process and tool wear.

2.2 Grinding

As a typical fixed-abrasive machining method, grinding method is widely applied in precision machining.   Grinding is the machining process which utilizes hard abrasive particles as the cutting medium to remove material and generate new surface.   Grinding is traditionally regarded as a final machining process in the production of components requiring smooth surfaces and fine tolerances.   There are numerous grinding types which vary according to the shape of the wheel and kinematic motions of work-piece and wheel head [9].   Here, the focus is placed on

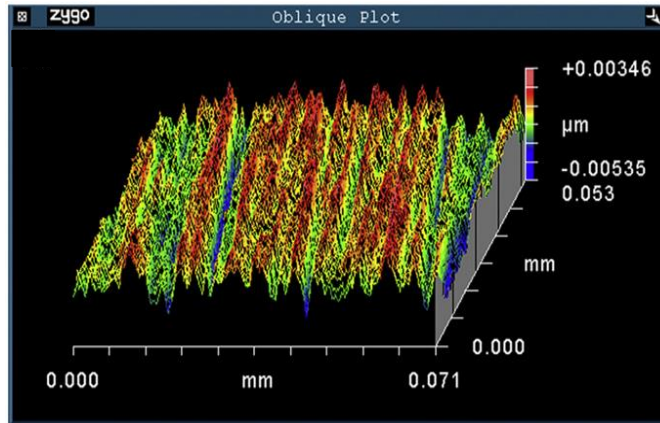Fig. 2.9 The configuration of wafer grinding machining tool

Fig. 2.10   Surface topographies of the ground silicon samples by the ZYGO profiler.
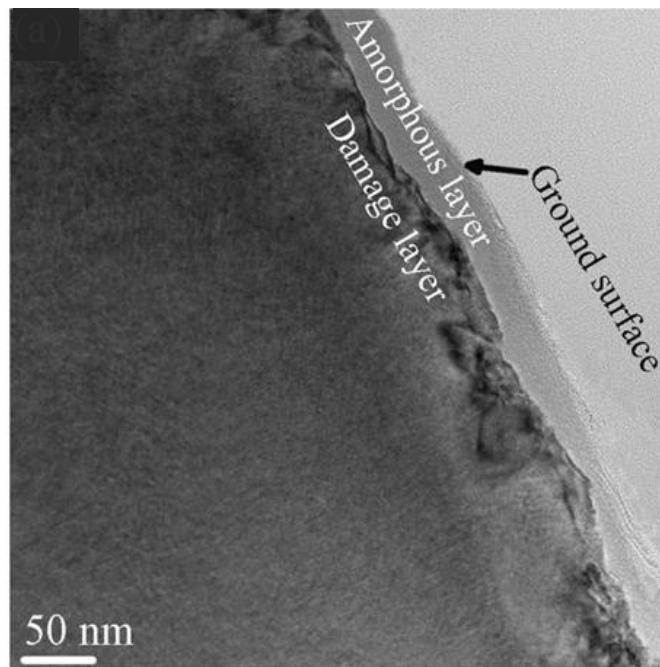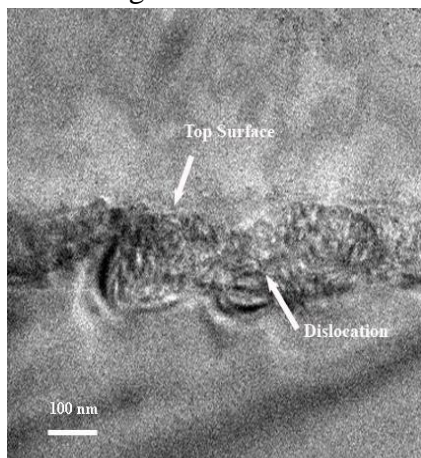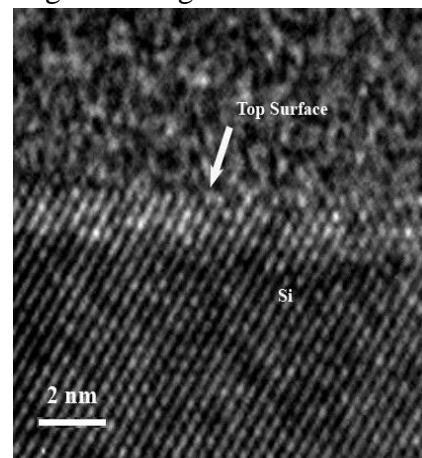

Fig. 2.11   Cross-sectional TEM images of the ground silicon

(a) By SD5000   (b) By CMG

Fig. 2.12 TEM images of silicon wafers fabricated by different wheels

Ra=0.456nm	Ra=0.562nm	Ra=72.890nm

<p style="text-align:center">(a) By CMG   (b) By CMP   (c) By SD800</p>
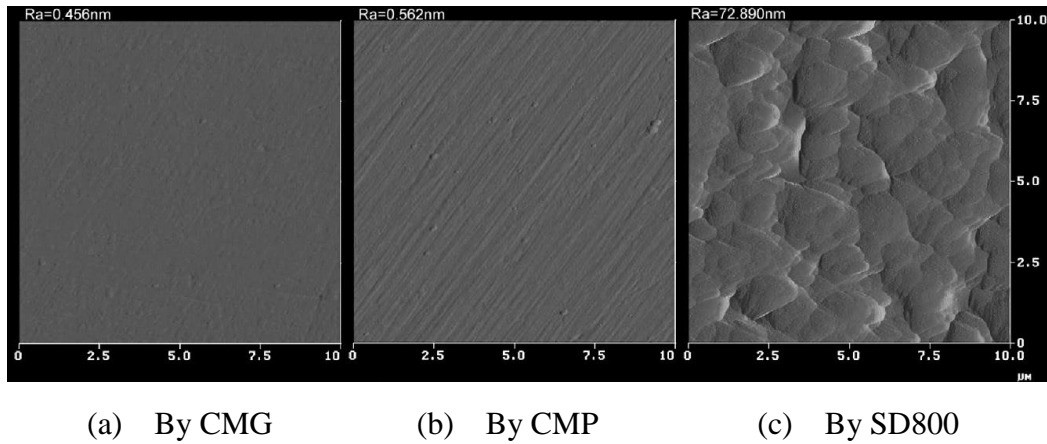
<p style="text-align:center">Fig. 2.13 The AFM figures of silicon wafers machined at different conditions</p>

wafer grinding.　Shown in Fig. 2.9 is machine tool which is developed by our laboratory for the fabrication of ϕ300 mm silicon.

By use of the latest technologies in ultra-precision engineering and the concept of ductile mode machining [3], grinding tests to achieve good surface roughness and less sub-surface damaged were reported.

Zhang [10] reported a vitrified bond diamond wheel with mesh size of 12000 was performed in the grinding of silicon wafers.　The Fig.2.10 is surface topographies of the ground silicon samples.　As shown in Fig. 2.10, the good surface roughness of 0.9±0.1 nm in R_a and 8.8±1.2nm in PV were achieved when the feed-rate is 6 μm per minute.　And then, the sub-surface of the ground wafer was examined using cross-section TEM.　It was found that the ground subsurface consisted of an amorphous layer and a damage layer as shown in Fig. 2.11.　The Fig.2.11 is cross-sectional TEM images of the ground silicon.　The damaged layer was still clearly observed from sub-surface of ground wafers.

The sub-surface damage or damaged layer which is developed by high stress during the process and remains on the surface of substrate after the process, becomes a critical problem for grinding process.　In order to overcome this problem, Zhou proposed a new grinding method which defined as chemo-mechanical grinding (CMG) and merges the advantages of fixed abrasive machining and CMP [11].

The Fig.2.12 (a) and (b) are the TEM images of silicon wafers fabricated by different wheels.　As shown in Fig. 2.12(a), a silicon wafer was machined by SD5000.　In the crystalline region below the top face, dislocations can be clearly seen.　However, after CMG, none dislocations can be observed under the top surface of the silicon wafer as shown in Fig. 2.12(b).

Not only a defect-free fabrication but also a good surface quality was able to obtained by CMG grinding.　Shown in Fig. 2.13(a)−(c) were the AFM image of 10

μm×10 μm quarts glass substrate surfaces, respectively finished by CMG, CMP and SD800.　CMG offered an extremely smooth surface (a) with roughness R_a <0.5nm slightly better than CMP. On the other hand, CMP left abrasive cutting marks on the surface (b) although its roughness was as same as that of CMG.　Whereas, a clear asperity was confirmed on the surface (c) by SD800.　It can be concluded that the geometrical accuracy and surface quality of quartz glass by CMG was the best in the three machining procedures.

As a conclusion for this section, the research of grinding of functional materials always focuses on geometry accuracy and sub-surface damaged.

2.3. Polishing

As the typical free-abrasive machining method, polishing is often used for creation of a smooth surface also as the final process to create a defect-free surface.

The Fig.2.14 is the configuration of polishing machine tool.　As shown in the Fig. 2.14, a wafer rotating with a carrier or chuck is pressed face down onto a rotating polishing pad while polishing slurry containing abrasive particles and chemical reagents flows in between the wafer and the polishing pad.　The combined action of polishing pad, abrasive particles and chemical reagents results in material removal and smoothing of the wafer surface.　From the literates addressed, the defect-free and good quality surface can be obtained by the polishing process.

The investigation on subsurface damage induced by chemical mechanical polishing on single crystal CdZnTe (111) was reported by Zhang [12].　Fig. 2.15 (a)-(e) shows the cross-section HRTEM micrographs of CdZnTe (111) after CMP with different magnification scales.　The surface after CMP is very smooth, free of any cracks, even at nanoscale magnification (Fig. 2.15(a)–(b)). When the magnification scale is 5 nm, the structure of single crystal lattice is much identified, and the
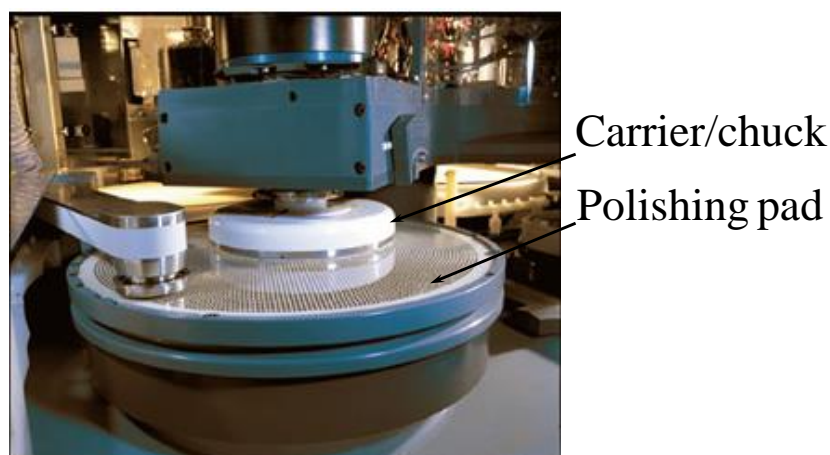

Carrier/chuck

Polishing pad

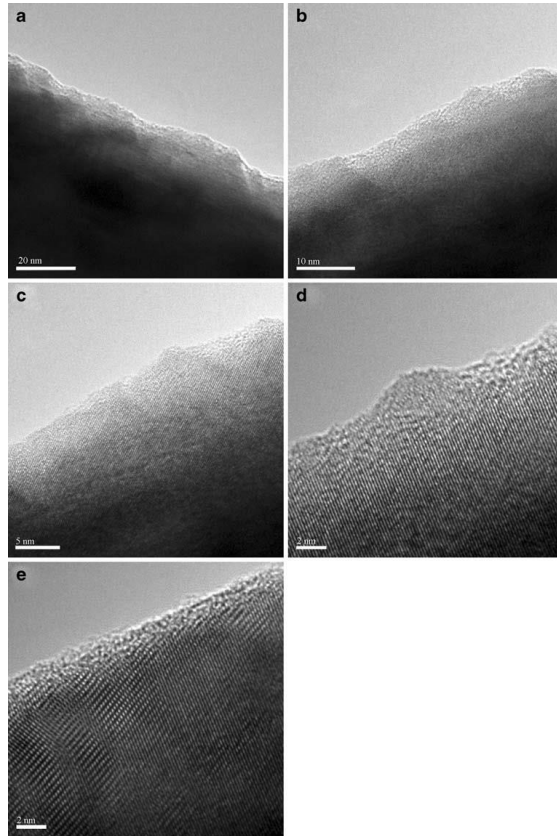Fig. 2.14 The configuration of polishing machine tool

Fig. 2.15 Cross-section HRTEM micrographs of CdZnTe (111) single crystal after CMP with scales of (a) 20 nm, (b) 10 nm, (c) 5 nm, (d) 2 nm, and (e) 2 nm
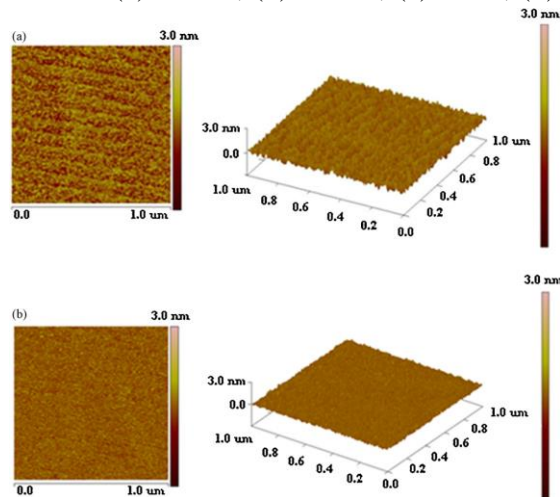

Fig. 2.16 Polished surfaces of (a) traditional CMP and (b) UFV–CMP observed by the AFM.

amorphous layer induced by CMP is only about 2 nm (shown in Fig. 2.15(c)). With further magnification, the single crystal lattice becomes clearer (shown in Fig. 2.15(d)–(e)). The single crystal lattice remains very perfect after CMP machining, and there is no any sub-surface damage left, excluding the 2 nm amorphous layer. As well as none sub-surface damage, good surface finish was also obtained from the polishing process.

21

Xu [13] reported the sapphire substrates were polished by traditional chemical mechanical polishing (CMP) and ultrasonic flexural vibration (UFV) assisted CMP (UFV-CMP) respectively with different pressures.   The surface roughness (root mean square, RMS) of the polished sapphire substrate of UFV-CMP is 0.83Å measured by the atomic force microscopy (AFM), which is much better than 2.12Å obtained using the traditional CMP.   And the surface flatness of UFV-CMP is 0.12 nm, which is also better than 0.23 nm of the traditional CMP.   The results show that UFV-CMP is able to improve the MRR and finished surface quality of the sapphire substrates greatly.   The polished surfaces of traditional CMP and UFV-CMP are shown in Fig. 2.16.

In conclusion, the researches of polishing functional materials always focuses on geometry accuracy and sub-surface damaged.

2.4 Summary

Compared with the main task in in chapter 1 which emphasized on the crystal structure, properties, application of LT, the literature survey about the machining process of functional materials are illustrated in chapter 2.

In the survey, it is found that good surface quality of several brittle or ductile materials like silicon and Al can be obtained from SPDT.   However, tool wear and sub-surface damage on machined surface compress wider application of SPDT. The good surface quality and better profile accuracy are obtained from grinding procedure which is performed in the ductile regime.   Though, the sub-surface damage is still able to be observed on the ground surface.   However, a new grinding method named CMG is proposed to solve this problem.   Polishing is a good method to achieve defect-free surface.   However, the disadvantages like low machining efficiency and bad profile accuracy with the work-piece size increased restrain its application.

From the survey of cutting, grinding and polishing, it can be concluded that most current processes focus on geometry accuracy, sub-surface damage, cutting mode, the influence of functional material's orientation, tool wear and so on.   There is none report about the influence of physical properties on machining process.   Hence, one of the main objectives in this research is given to study the influence of LT physical properties on its machining process.

The material property is also very important for achieving a perfect surface. However, until now the basic mechanical properties of LT are still unknown. A robust procedure to analyses the mechanical properties of LT will give in next chapter.

Reference

[1] Information on: http://www.diverseoptics.com/

[2] Hamilton; "Surface generation in ultra-precision single point diamond turning of aluminum".

[3] T. G. Bifano, T. A.Dow and R. O. Scattergood, "Ductle-regie grinding: A new technology for machining brittle materials", *ASME J. Eng'g for Industry*, Vol. 113, No. 2, (1991), pp. 184-189.

[4] H. T. Young, H. T. Liao, and H. Y. Huang, "Novel method to investgate the critical depth of cut of ground silicon wafer," *Journal of Material Process. Technology.*, Vol.182, pp. 157-162, 2007.

[5] Ming Zhou, B.K.A. Ngoi, M.N. Yusoff and X.J. Wang; "Tool wear and surface finish in diamond cutting of optical glass", *Journal of Material Process Technology*, Vol. 174, (2006), pp. 29-33.

[6]. Qingliang Zhao, Yilong Wang, Guang Yu *et.al*; "Investigation of anisotropic mechanisms in ultra-precision diamond machining of KDP crystal", *Journal of material process technology*, Vol. 209, (2009), pp. 4169-4177.

[7] Jiwang Yan, Tooru Asami, Hirofumi Harada *et.al*: "Impurities detection by optical techniques in KH_2PO_4 crystals", *Precision engineering*, Vol.33 (2009), p.378–386.

[8] Saurav Goel, XichunLuo, PaulComley, *et.al*: "Brittle–ductile transition during diamond turning of single crystal silicon carbide", *International Journal of Machine Tool & Manufacture*, Vol. 65, (2013), pp.15-21.

[9] Information on: http://en.wikipedia.org/wiki/Grinding (video_gaming).

[10] Zhenyu Zhang, FengweiHuo, YueqinWua *et.al*: "Grinding of silicon wafers using an ultrafine diamond wheel of a hybrid bond material", *International Journal of Machine Tool & Manufacture*, Vol. 51, (2011), pp.18-24.

[11] Libo Zhou, Takeshi Shiina, Zhongjun Qiu *et.al*: "Research on chemo-mechanical grinding of large size quartz glass substrate", *Precision Engineering*, Vol.33, (2009), pp.499–504.

[12] Zhenyu Zhang, Hang Gao, Wanqi Jie, Dongming Guo *et.al*: "Chemical mechanical polishing and nanomechanics of semiconductor CdZnTe single crystals", *Semiconductor. Science. Technology.* Vol.23, Iss.10, (2008),

[13] Wenhu Xu, Xinchun Lu, Guoshun Pan *et.al*: "Ultrasonic flexural vibration assisted chemical mechanical polishing for sapphire substrate", *Applied surface science*, Vol. 256, (2010), pp.3936-3940.

Chapter 3 Robust data analysis procedure for nano/micro indentation

The elastic modulus E and hardness H are two most important parameters used for evaluation of the mechanical properties of materials. The instrument and measurement procedure are very critical for precise estimation of the values of E and H. The most extensively used method is load-displacement sensing indentation, in which no image of indent impression is required. Recently, many efforts have been made in developing micro/nano indentation for probing the mechanical properties of materials and thin films on the sub-micron and nano-scale[1-4].

When a small indentation is made at sub-mN load and nanometer displacement, however, the measured load-displacement data becomes unstable because it always contains a certain degree of noise. The instability of acquired data will directly affect the calculation results of the elastic modulus and hardness. In addition, due to blunting and roundness at the tip of indenter, the contact area calculated from a perfect geometry is no longer valid especially in case of micro/nano indentation. A proper procedure of data analysis and compensation is thus essential to determine the values of elastic modulus and hardness with high accuracy and precision. Reported in this chapter is a robust approach of data analysis for determining the contact stiffness and contact area. Comparisons of results are made on different test materials (silicon vs. aluminum) with different geometries of indenters (brand new vs. blunted), to demonstrate the stability and reliability of the proposed approach for data analysis in micro/nano indentation.

3.1 Theoretical expression of hardness and elastic modulus at micro/nano indentation

Micro/nano indentation test performs indenting a specimen by a very small load using a high precision instrument, which records both load and displacement simultaneously and continuously. Fig. 3.1 (a) is a schematic representation of load-displacement curve, where F_{max} is the peak load, h_{max} is the indenter displacement at the peak load, h_p is the final depth of the contact impression after unloading. Fig. 3.1 (b) shows a cross-section of the corresponding indentation and identifies the parameters used in the subsequent analysis. h_c is the contact depth of indenter at the peak load and h_s is the displacement of the surface at the perimeter of the contact. Thus, the relationship of $h_{max} = h_c + h_s$ is satisfied. Upon unloading, the elastic displacements are recovered, and final depth of residual indent impression is left as h_p. Fig. 3.1 (c) is the top-view of the residual indent impression by a Berkovich type indenter, where the solid line envelopes the indent area which
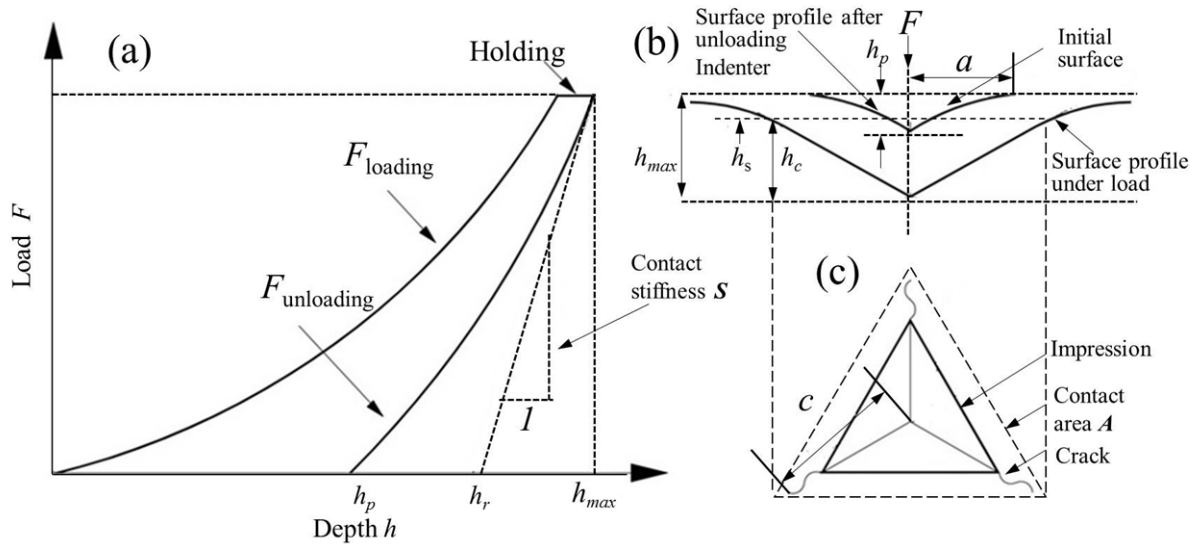
Fig. 3.1 A schematic representation of an indentation.   (a) load-displacement curve, (b) cross-section of indentation process, (c) residual indent impression corresponds to the final depth h_p.   On the other hand, the contact area A which corresponds to the contact depth h_c is unobservable upon unloading, but should be slightly larger than the indent area as shown by the broken line.

During indentation, the compliance of the specimen and the indenter tip can be combined as springs in series.   Therefore,

$$\frac{1}{E_r} = \frac{(1-v_s^2)}{E_s} + \frac{(1-v_i^2)}{E_i} \tag{3.1}$$

Here, E_r is the "reduced modulus", E is the elastic modulus, v is the Poisson ratio, and suffix i and s refer to the indenter and specimen respectively.

The reduced modulus was first related to the contact stiffness of indentation by Sneddon [5] who yielded,

$$E_r = \frac{\sqrt{\pi}}{2} \frac{S}{\sqrt{A}} \tag{3.2}$$

where S is the contact stiffness and A the contact area.   Later, Pharr, Oliver and Brotzen [6] proved that Eq. (3.2) is a robust equation which applies to indenter with a wide range of geometries.

The indentation hardness is simply defined as;

$$H = \frac{F_{max}}{A} \tag{3.3}$$

It should be noted that hardness evaluated using Eq. (3.3) may be different from that of the conventional definition in which the contact area is determined by direct measurement of the size of residual indent impression.   In the micro/nano indentation analysis the hardness is calculated utilizing the contact area at peak load

whereas in conventional tests the area of the residual indent after unloading is used.

From Eq. (3.2) and (3.3), it is easy to understand that both values, elastic modulus as well as indentation hardness, strongly depend on the contact stiffness S, the contact area A and the accuracy with which they are determined. Unfortunately, the contact stiffness S and the contact area A are unable to be directly derived from the acquired load-displacement data. A proper analysis procedure is therefore essential to get reliable contact stiffness and contact area.

3.2 Micro/nano indentation instrument and experimental procedure

The micro/nano indentation instrument used in this study was Shimadzu DUH-W201, as shown in Fig. 3.2 (a). Its specifications are listed in Table 3.1. A diamond Berkovich indenter was used for indentation tests. Shown in Fig. 3.2 (b) was a brand new indenter. Its tip angles of each side were 115°01', 115°05' and 115°08' respectively. The departure from a perfect Berkovich indenter was very limited, and its effect on the area function was described in the section 3.5. Fig. 3.2 (c) was a blunted indenter which was used to investigate the effect of tip wear on the area function and results of calculated elastic modulus and hardness.

Two kinds of specimens were chosen for this study. One was the single crystal Si wafer [100], represented hard-and-brittle and anisotropic materials. The other
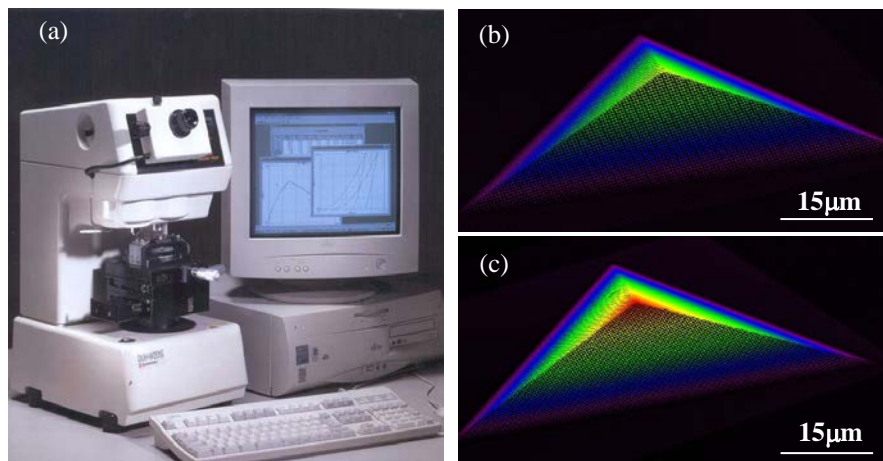

Fig. 3.2 (a) indentation instrument, (b) brand new indenter, (c) blunted indenter

Table 3.1 Specifications of indentation instrument

Load range	0.1-1960 mN
Load accuracy	±19.6 μN
Indentation depth range	0-10 μm
Indentation depth resolution	10 nm
Indenter type	Berkovich, Vickers and Knoop

Table 3.2 Test conditions

Workpiece	Silicon [100], Aluminum alloy A4043 (5%Si, 0.8%Fe, 0.3%Cu contained)								
Applied load [mN]	2.5	5.0	7.5	10.0	15.0	20.0	23.0	26.6	31.5	37.25
Loading rate [mN/s]	0.18	0.36	0.54	0.72	1.08	1.45	1.66	1.92	2.28	2.70
Repeated count	10 times for each specified load									
Indenter type	Brand new and blunted Berkovich indenters (new indenter applied to both Si and Al, blunted indenter applied to Si)									
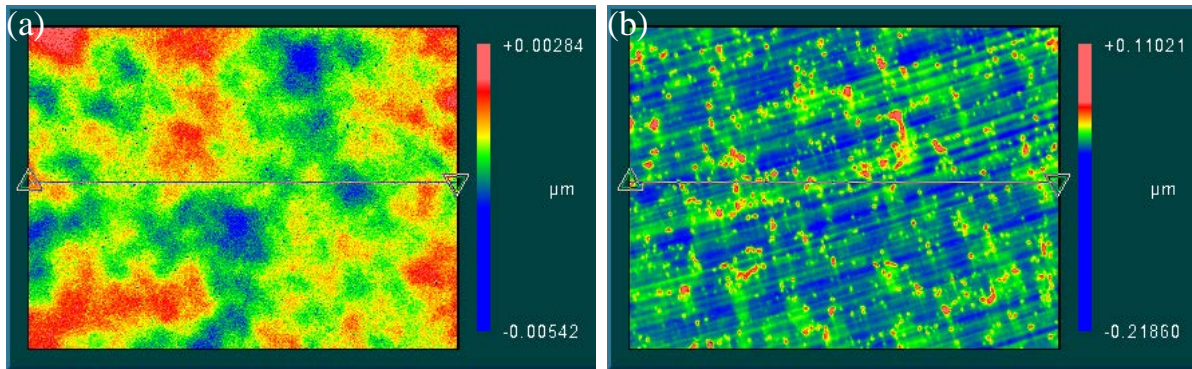
Fig. 3.3 Specimens of (a) crystal Si wafer (Ra=0.56nm)，(b) Aluminum (Ra=5.92nm)

was aluminum alloy A4043 (5%Si, 0.8%Fe, 0.3%Cu contained), represented soft-ductile and isotropic materials. As shown in Fig. 3.3, the test surfaces of both specimens were mirror finished up to roughness $R_a < 6$ nm, prior to indentation tests.

The indentation tests were conducted at room temperature. The indenter was loaded at a constant rate until reaching the specified peak load, held for 5 seconds, and then unloaded at the same rate. For each specimen, separate peak loads ranging from 2.5mN to 1000 mN were investigated. Cracks were found on Si specimen when the peak load exceeded 40 mN. In this paper the data obtained from the peak load below 40 mN were used for subsequent analysis. The loading/unloading rate also varied in proportion to the peak load to assure that all indentation tests were conducted in the same period of 33 seconds. At least 10 indentations were made at each peak load. Each indent was separated by 10 ~ 25 μm to avoid possible interference between neighboring events. The specific indentation conditions were listed in Table 3.2.

The brand new indenter was used to conduct indention tests on Si and Al, whereas the blunted indenter was used for silicon specimen to investigate the effect of tip geometry imperfection.

## 3.3 Analysis procedure of determining contact stiffness S

The contact stiffness S is given as the slope of the unloading curve which is usually nonlinear;

$$S = \frac{\mathrm{d}F}{\mathrm{d}h} \tag{3.4}$$

The contact stiffness is not only used to calculate the elastic modulus, but also to provide a physically justifiable procedure for determining the contact depth h_c which is used in conjunction with the indenter tip area function to establish the contact area in the subsequent section.

A standard procedure to accomplish the estimation is to perform a linear fitting to a fraction of the upper portion of the unloading curve and use its slope as an estimate of the contact stiffness. Two drawbacks of this method are worthy to note. First, the estimated contact stiffness varied significantly, depending on how much of the unloading data is used in the linear fitting. Normally, the estimated contact stiffness decreases with an increasing in fraction of unloading data used for fitting [7]. Second, even most indentation instrument manufacturers use upper 30% of unloading data for linear fitting and estimation of the contact stiffness [8], the estimated value still varies significantly because load/unload-displacement data are unstable and always contain a certain degree of noise when small indentations are made at a scale of sub mN load and nm displacement.

An example of load/unload-displacement curve obtained at indentation test on Si surface was shown in Fig. 3.4, in which peak load of $F_{max}= 5$ mN was applied. Due to the instability of the instrument and the environment, a large fluctuation in acquired data was observed. The contact stiffness was estimated by the above-mentioned
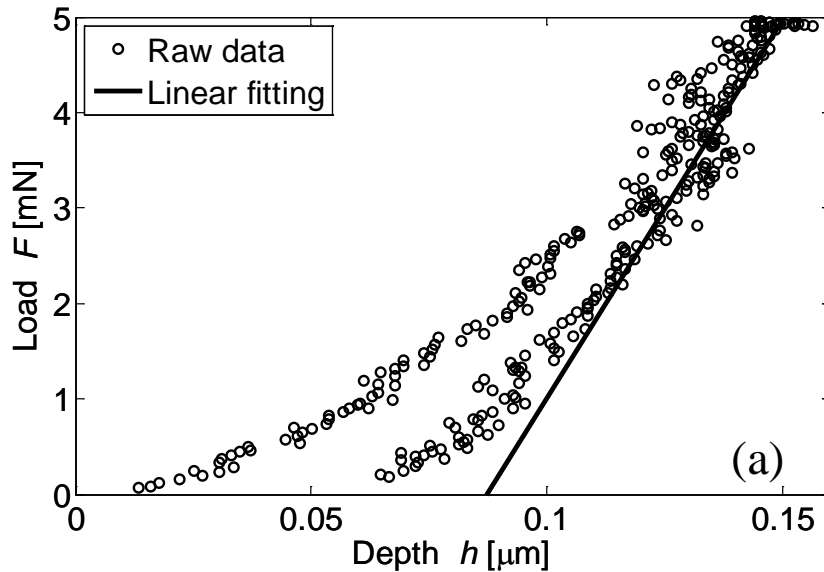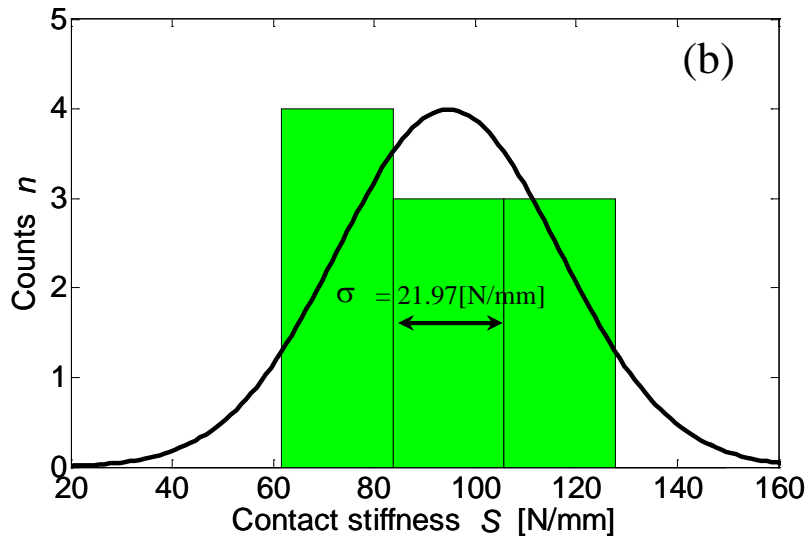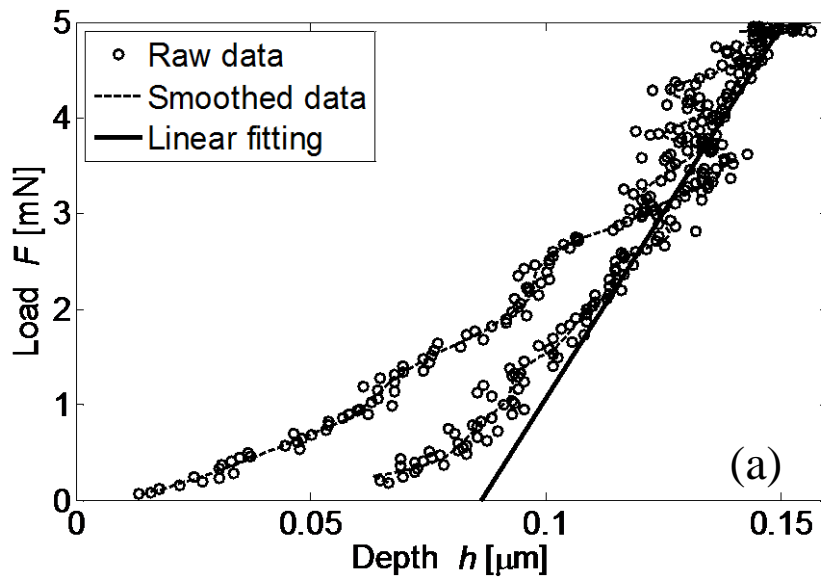
Fig. 3.4 (a) raw data and linear fitting of upper 30% data, (b) contact stiffness and its distribution

standard procedure and its slope was presented in (a) with a solid line. The distribution of estimated contact stiffness was given in (b), where its standard deviation was as large as 29.02 [N/mm].

In order to solve this problem, two kinds of alternative procedures of data analysis were compared and discussed in this section. The first is to smooth (or de-noise) the acquired data prior to linear fitting. Here, a digital low-pass filter was developed by use of discrete wavelet transform (DWT) [9] and applied to the acquired raw data. The result obtained from the same unloading data of Fig. 3.4 was shown in Fig. 3.5 (a), where the response of DWT filter was presented by a narrow line.
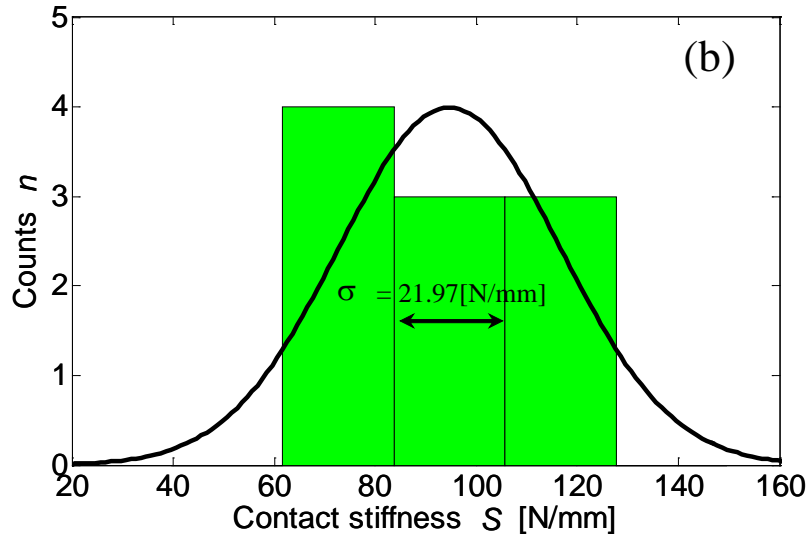
Fig. 3.5 (a) raw data and linear fitting of upper 30% data, (b) contact stiffness and its distribution

The upper 30% of filtered data were then used for linear fitting and estimation of the contact stiffness, in the same way used in standard procedure. The distribution of estimated contact stiffness was given in (b), where its standard deviation was 21.97 [N/mm], smaller than that obtained by the standard analysis procedure. Instead of linear fitting, second, Oliver and Pharr to perform a non-linear curve fitting based on the observation that unloading data are well described by a simple power law relation [7]. The actual relationship used to describe the unloading curve for stiffness estimation is

$$F = \alpha(h - h_{\mathrm{p}})^{m} \tag{3.5}$$

where α and m are constants, h_{p} is the final depth of indent impression after complete unloading. Three parameters α, h_{p} and m are all determined by a least square fitting procedure. The contact stiffness is found by analytically differentiating Eq. (3.5) at the peak displacement as

$$S = \frac{\mathrm{d}F}{\mathrm{d}h} = \alpha \cdot m(h_{\max} - h_{\mathrm{p}})^{m-1} \tag{3.6}$$

The solid line shown in Fig. 3.6 (a) was resultant curve fitted to the same unloading data given in Fig. 4 where α, h_{p} and m were estimated to be 333.19, 0.046 and1.86 respectively. The contact stiffness was calculated by Eq. (3.6) and its distribution was plotted in Fig. 3.6 (b). It is found the standard deviation is about one third of that obtained from the standard analysis procedure of linear fitting. The average value and standard distribution of contact stiffness obtained by above-mentioned three analysis procedures are summarized in Table 3.3. Examining these results, it can be
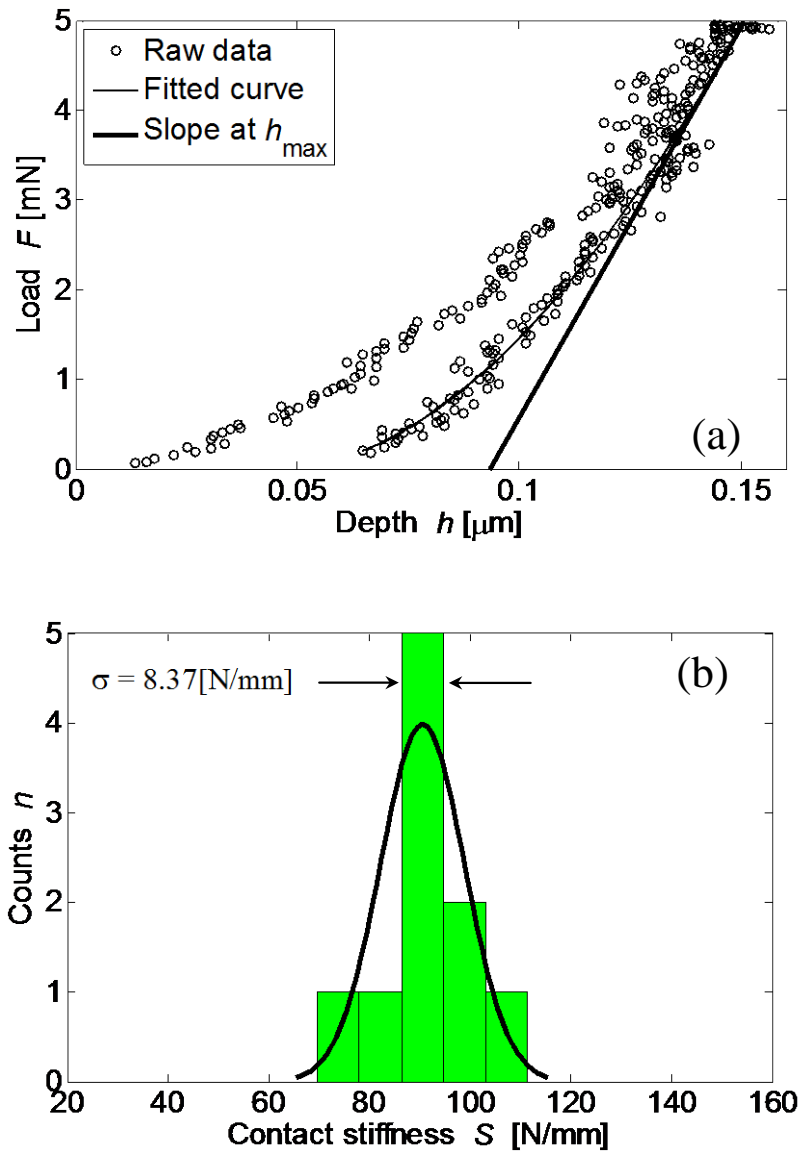
31

Fig. 3.6 (a) smoothed data and linear fitting of upper 30% data, (b) contact stiffness and its

distribution

Table 3.3 Summary of contact stiffness calculated by three approaches

Contact stiffness [N/mm]	The standard analysis procedure	Smoothing and linear fitting	Curve fitting
Average	86.54	94.70	90.58
Standard distribution	29.02	21.97	8.37

Examining these results, it can be concluded that the contact stiffness computed from the curve fitting method is most reliable and robust, and thus used in the rest data analysis of this paper.

3.4 Analysis procedure of determining tip area function A

Another important practical consideration is how well the contact area A is determined, since computation of both elastic modulus and hardness are significantly dependent on the accuracy of contact area through Eq. (3.2) and (3.3). For a Berkovich indenter, the contact area A is expressed in polynomia [7] which is called as tip area function;

$$A = C_0 h_c^{2} + C_1 h_c + C_2 h_c^{1/2} + C_3 h_c^{1/4} + C_4 h_c^{1/8} + ... + C_8 h_c^{1/128} \qquad (3.7)$$

where C_0 through C_8 are constants. h_c is the contact depth of indenter. For a Berkovich indenter, it is given by Oliver and Pharr [7] as;

$$h_c = h_{max} - 0.75 \frac{F_{max}}{S} \qquad (3.8)$$

The lead term of Eq. (3.7) describes an ideal shape of Berkovich indenter, while the others describe deviations from Berkovich geometry due to blunting at the tip or any possible reasons. For a triangular pyramid indenter with tip angle of 115°, the value of C_0 is often referred to 24.5 in many reports [6, 7, 10], but it may not always be true due to the inaccuracy of tip angle of indenter. Most micro/nano indentation instruments require the tip angle of indenter to be finished within 115°±15', or 114.75°~115.25°. Fig. 3.7 plots C_0 as a function of tip angle based on a geometrical calculation. It is found that the C_0 could vary from 22.66 to 25.24 during the tolerable range of tip angle. Therefore, C_0 needs to be specified according to the tip angle of indenter actually used, and takes 24.29 for the brand new indenter used in this study. The standard procedure, in which the tip geometry is assumed to be ideal,
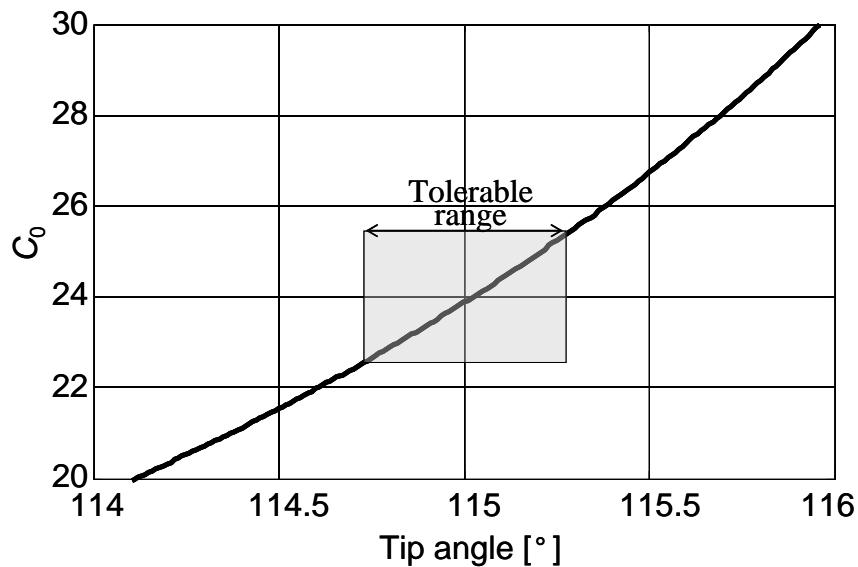

Fig. 3.7 Relationship between tip angle and C_0

is often negatively affected by "size effect" when small load is applied.

In order exclude the effects of tip geometry deviation, the constants C_1 through C_8 need to be compensated via serial experiments with indenting depth from small to large. Oliver and Pharr proposed a method [7] to estimate those constants as well as E_r by literately fitting A vs. h_c. However, it is tedious and time consuming. Here, we propose a new procedure for determining the area function based on multivariable estimation via a least square fitting.
The analysis begins by rewriting Eq. (3.2) as;

$$S = \frac{2}{\sqrt{\pi}} E_r \sqrt{A} = \frac{2}{\sqrt{\pi}} E_r \sqrt{24.29 h_c^{\,2} + C_1 h_c + C_2 h_c^{\,1/2} + C_3 h_c^{\,1/4} + ... C_8 h_c^{\,1/128}} \qquad (3.9)$$

where E_r and C_1 through C_8 are variables to be estimated. The contact stiffness S and the corresponding contact depth h_c are pre-determined using the procedure mentioned in the previous section and Eq. (3.8) respectively. Each load-displacement data results in a pair of (S, h_c). A series of indentation with different loads, consequently, can constitute a relationship between S and h_c. By least square fitting the curve expressed in Eq. (3.9) to those (S, h_c), variables E_r and C_1 through C_8 are able to be estimated.

3.5 Experimental results and analysis

Fig. 3.8 (a) showed the relationship between S and h_c obtained at indentation experiments on Si. It was found that the contact stiffness increased with an increasing in contact depth, or indentation load. The solid line represented the fitting curve by the procedure above-mentioned, where the variables were estimated to be E_r =155.1911 GPa, $C_1 = -0.0022$, $C_2 = -0.0009$, $C_3 = -0.0005$, $C_4 = 0.1778$ respectively. The rest C_5 through C_8 were negligible. Therefore, the tip area function for Si was estimated as;

$$A_{\text{Si}} = 24.29 h_c^{\,2} - 0.0022 h_c - 0.0009 h_c^{\,1/2} - 0.0005 h_c^{\,1/4} + 0.1778 h_c^{\,1/8} \qquad (3.10)$$

Fig. 3.8 (b) shows the same results but obtain at the indentation experiments on Aluminum. The tip area function estimated for Aluminum was;

$$A_{\text{Al}} = 24.29 h_c^{\,2} + 0.0034 h_c + 0.0033 h_c^{\,1/2} + 0.0013 h_c^{\,1/4} + 0.0266 h_c^{\,1/8} \qquad (3.11)$$

Both estimated area functions were plotted in Fig. 3.9, together with that of ideal Berkovich indenter. Above results suggested two facts. First, the brand new indenter had little deviation fromthe ideal tip of indenter, yet a certain degree of roundness or imperfection was found when the detail was zoomed up. If the difference in depth between the ideally sharp tip and the round tip is taken into consideration, an actual tip always has a larger contact area than an ideal tip at the same contact depth.
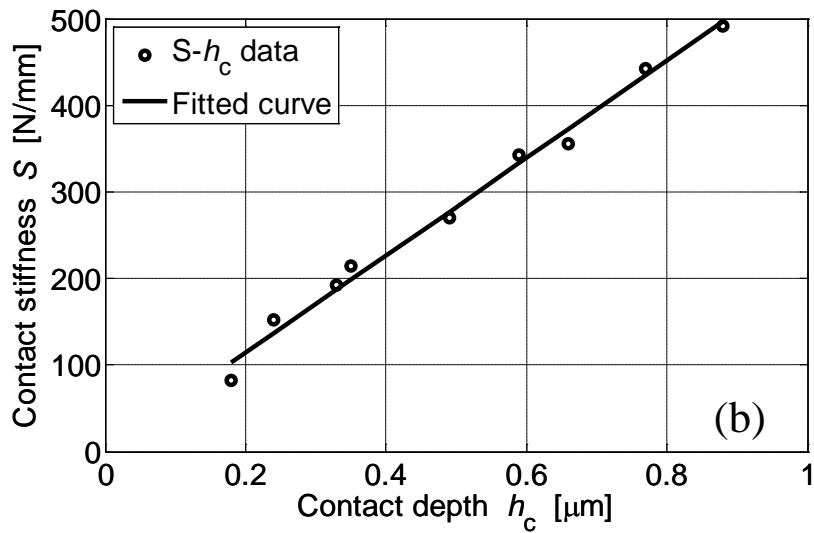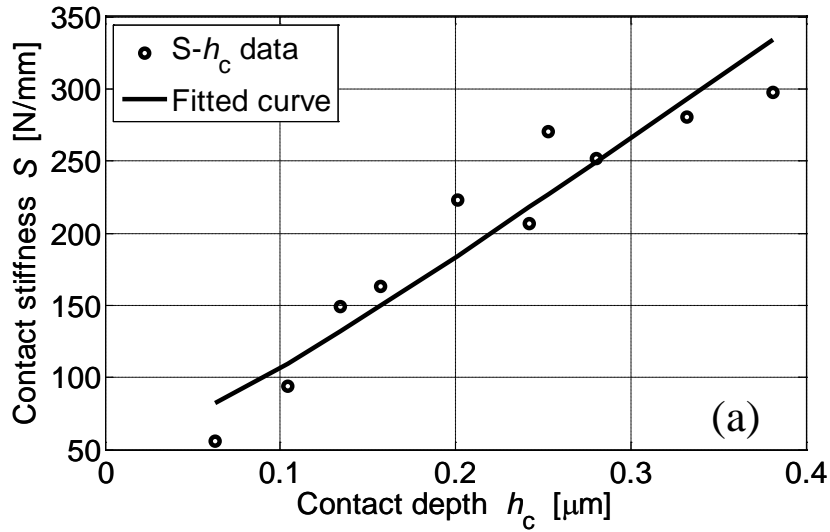
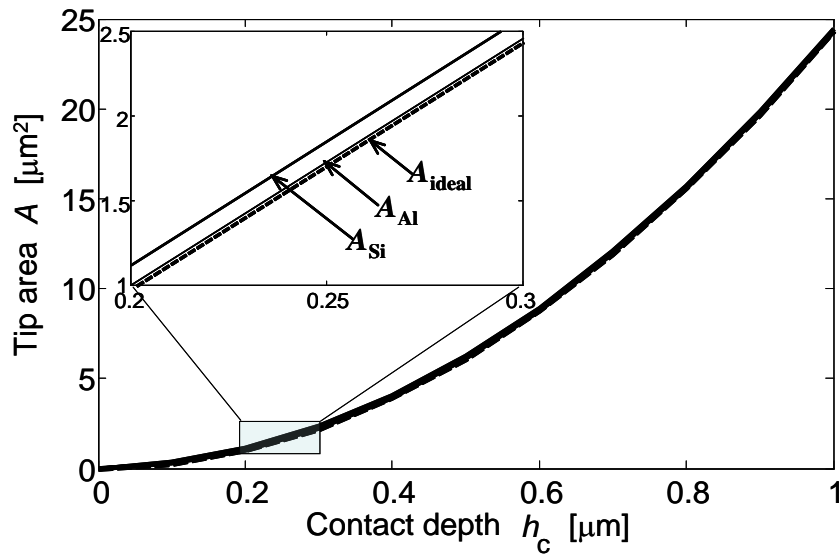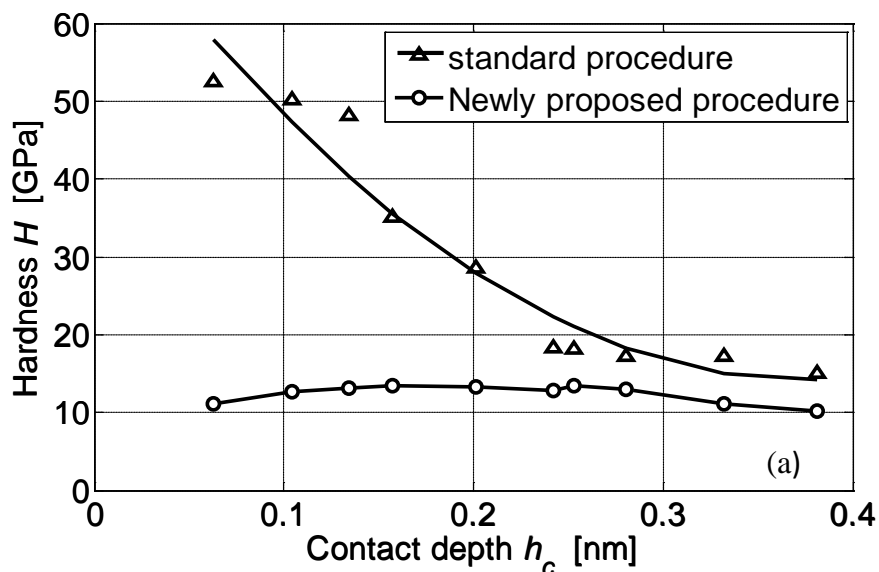Fig. 3.8 Relationships between stiffness and contact depth of (a) Si and (b) Al

Fig. 3.9   Compensated tip area functions

Second, the area function was dependent on materials to be indented. The tip deviation for silicon indentation was found to be larger than that for aluminum. It should be noted that this fact is different from the report made by Oliver and Pharr in [7]. It is more reasonable to consider that different materials have different displacement of the surface h_s at the same indentation load. Consequently, the contact depth h_c, which is given by $h_{max} - h_s$, is material dependent, and so is the tip area function.

The elastic modulus and hardness computed by Eq. (3.1), (3.2) and (3.3) were shown in Fig. 3.10 and Fig. 3.11 where the results obtained by both standard procedure and our newly proposed procedure were plotted for comparison. Very little indentation size effect can be seen from data estimated by the newly proposed procedure. In addition, the estimates of elastic modulus and hardness for both materials were reliable as they were compatible with commonly accepted values [7, 10].

The indentation tests were repeated on silicon specimen by use of the blunted indenter. Obtained (S, h_c) and fitted curves were compared in Fig. 3.12 (a) to see the effect of indenter tip geometry. The corresponding tip area functions were shown in Fig. 3.12 (b). The blunted indenter was found to have larger deviations from ideal geometry of Berkovich indenter as compared with the new indenter.

The horizontal distance between the compensated (estimated) area function and ideal area function, which represented the difference in depth at the same contact area, was a rough indicator of tip wear. For the current case, the results suggested the tip wear of 8.7 nm for the brand new indenter while 130 nm for the blunted indenter. Although the area functions for new and blunted indenters were very much different, the derived elastic modulus (164.14 [GPa] from the new indenter and 151.39 [GPa]
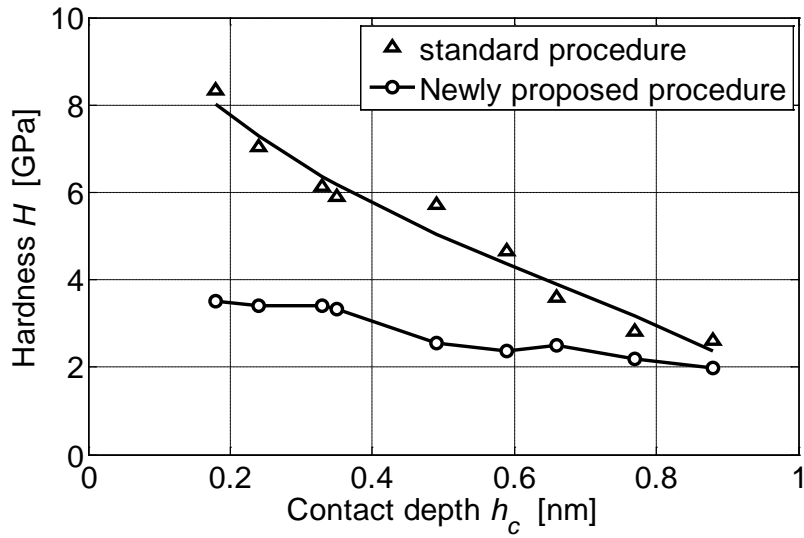

(a)

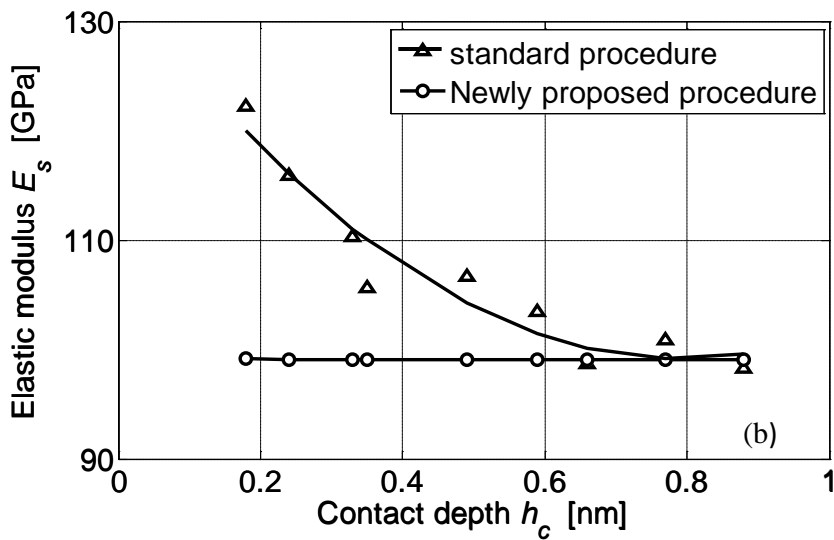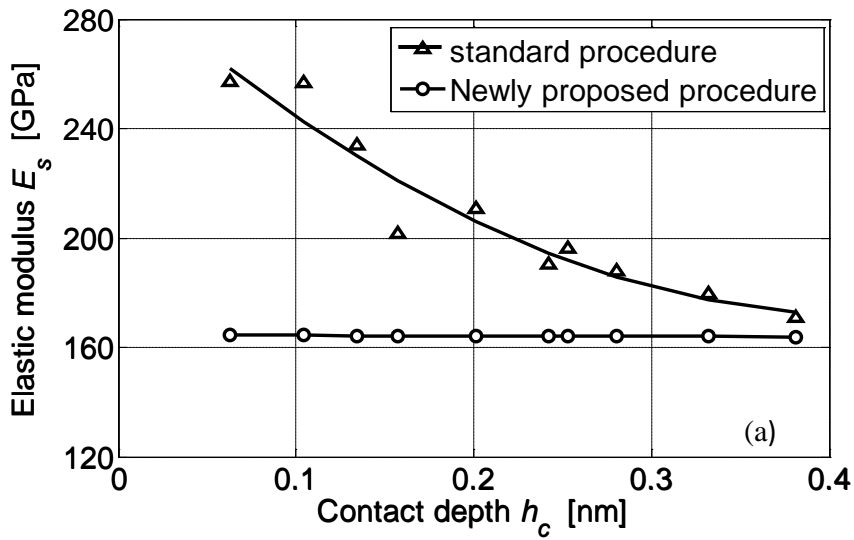Fig. 3.10 Relationship between Hardness H and Contact depth h_c. (a) Si and (b) Al

Fig. 3.11 Relationship between Elastic modulus E_s and Contact depth h_c. (a) Si and (b) Al
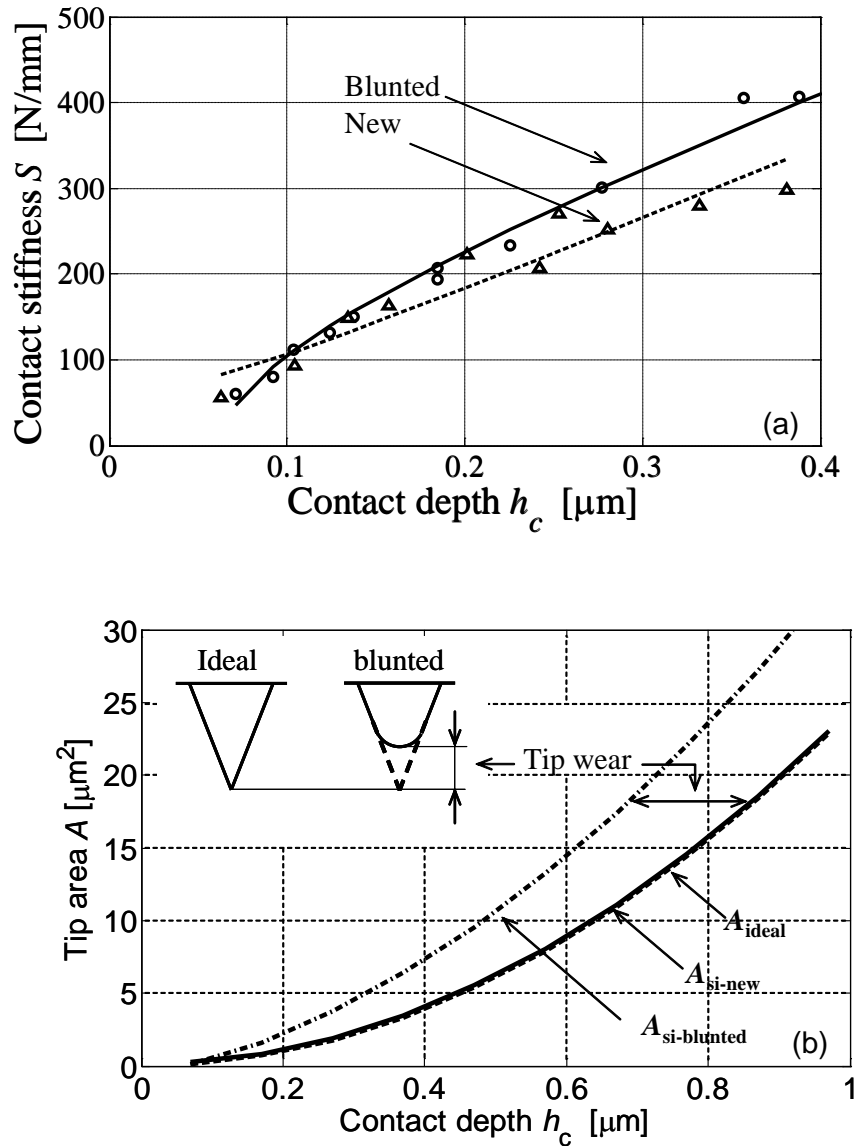
Fig. 3.12(a) Relationships between stiffness and contact depth, (b) corresponding area functions

from the blunted indenter) and the derived hardness (12.41 [GPa] from the new indenter and 11.14 [GPa] from the blunted indenter) were compatible each other. Again, this fact suggests the proposed procedure of data analysis is not only valid for a variety of materials from hard-brittle to soft-ductile, but also robust and applicable to blunted indenters with a certain geometry imperfection.

3.6 Summary

In this chapter proposed a robust procedure of data processing for determining the contact stiffness and contact area in micro/nano indentation. The main results obtained are summarized as follows;

(1) For estimation of contact stiffness, it is found that the approach of curve fitting is most reliable and robust as compared with the standard linear fitting and DWT smoothing followed by linear fitting.

(2) A new procedure of data process for determining the tip area function is proposed based on multivariable estimation via a least square fitting.   The experimental results proved that this procedure is not only valid for a variety of materials from hard-brittle to soft-ductile, but also robust and applicable to indenters with a certain geometry imperfection.

(3) Unlike reported elsewhere, the estimated tip area function by proposed procedure is dependent on materials to be indented.   This result reasonably matches with the commonly accepted fact that different materials have different displacement of the surface at the same indentation load.

(4) The deviation from the estimated to the ideal tip area functions provides a quantitative estimation of tip wear for diamond indenters.

Followed the robust data analysis procedure, the material characterization of LT is presented in the next chapter.

References

[1] Oliver WC, Hutchings R, Pathica, JB: ASTM STP 889. In: Blau PJ, Lawn BR. Editors: American Society of Testing and Materials. Philadelphia, PA, (1986), pp. 90-108.

[2] Doerner MF, Nix WD: "A Method for Interpreting the Data from Depth-sensing Indentation Instruments". *Journal of Material Research*, (1986), pp. 601-16.

[3] Joslin DL, Oliver WC: "A New Method for Analyzing Data From Continuous Depth-sensing Microindentation Tests". *Journal of Material Research,* (1990), pp. 123-26.

[4] Woirgard J, Dargenton JC: "An Alternative Method for Penetration Depth Determination in Nanoindentation Measurements", *Journal of Materials Research,* Vol.12, (1997), pp. 2455-58.

[5] Sneddon IN: "The relation between load and penetration in the axisymmetric boussinesq problem for a punch of arbitrary profile". *International of Journal Engineering Science*, Vol. 3, (1965), pp. 47-57.

[6] Pharr GM, Oliver WC, Brotzen FR: "On the generality of the relationship among contact stiffness, contact area and elastic modulus during indentation". *Journal of Material Research*, Vol. 7, (1992), pp. 613-17.

[7] Oliver WC, Pharr GM: "An improved technique for determining hardness and elastic modulus", *Journal of Material Research,* Vol.7, (1992), pp. 1564-83.

[8] Information on: Shimadzu corporation   http://www.shimadzu.co.jp/.

[9] Zhou L, Ono M, et. al: "Study on Surface Profile Evaluation for Large Si Wafer Measurement". *Journal of Japan Society Precision Engineering*, Vol. 55, (2011), pp. 1165-69.

[10] Panich N, Yong S: "Improved method to determine the hardness and elastic moduli using nano-indentation", *KMITL Science Journal*, Vol.5, (2005),pp. 483-92.

Chapter 4 Material characterization of functional materials

In this chapter, three types of single crystal, LT, Si and sapphire, are chosen for evaluation and comparison. Micro/nano-indentation tests are performed on LT $(01\bar{1}0)$, Si (100) and sapphire (0001, c-plane) wafers to study their behaviors in elastic, plastic (ductile) and brittle regimes respectively. The obtained results are analyzed and discussed to understand their differences in mechanical properties and the influences on their machinability in the machining process.

4.1 Test conditions of micro indentation

In addition to LT crystal $(01\bar{1}0)$, other two kinds of specimens chosen for comparison and study were single crystal sapphire (0001) and Si (100). As shown in Fig. 4.1, the test surfaces of all specimens were mirror finished up to roughness Ra < 6 nm, prior to indentation tests.

The indentation tests were conducted by use of Shimadzu DUH-W201 at room temperature. The indenter was loaded at a constant rate until reaching the specified peak load, held for 5 seconds, and then unloaded at the same rate. For each specimen, separate peak loads ranging from 2.5mN to 1000 mN were investigated. At least 10
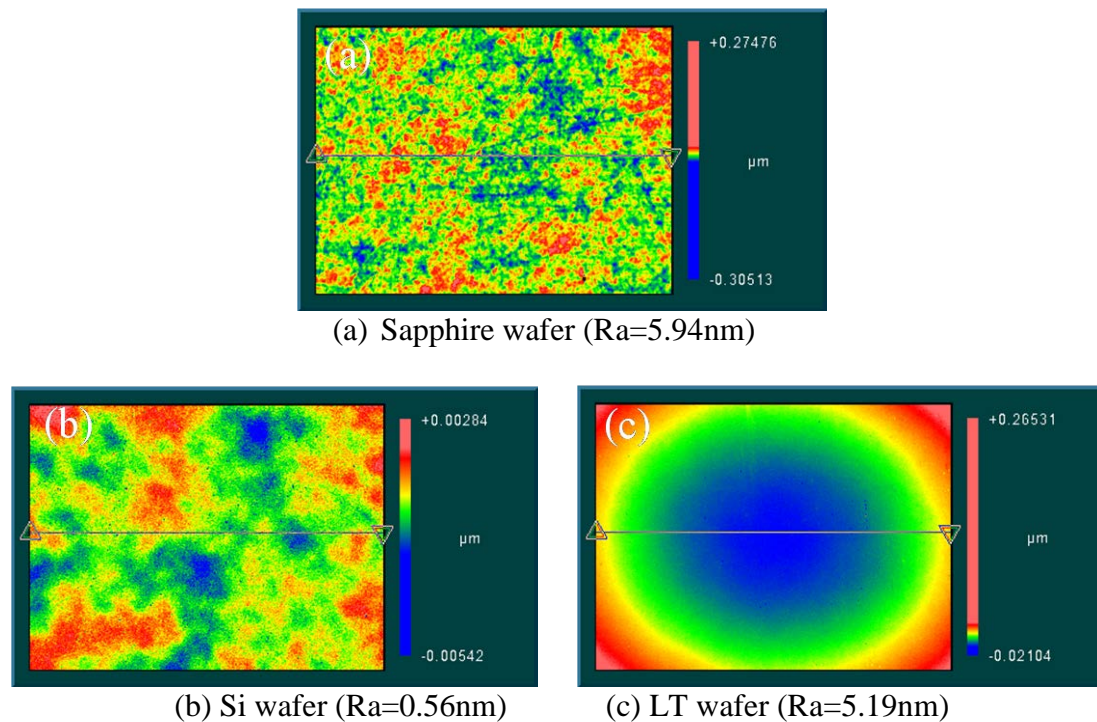

(a) Sapphire wafer (Ra=5.94nm)

(b) Si wafer (Ra=0.56nm)   (c) LT wafer (Ra=5.19nm)

Fig. 4.1 Surface topography of specimens

Table 4.1 Indentation test conditions

Workpiece	Sapphire (0001), Silicon (100) and LiTaO$_3$ (01$\bar{1}$0) (Y-cut)
The type of indenter	Three-side pyramid Berkovich 115°±15'
Applied load (mN)	2.5-1000
Load rate (mN/s)	Applied load/13.89 (when 2.5mN < F_{max} < 40mN)
	2.7 (when 40mN < F_{max} < 1000mN)
Repeated count	10 times for each specified load

indents were performed for each specified load. Each indentation was separated by 10 ~ 25 μm to avoid possible interference between neighboring events. All indent impressions left on specimen surface were finally examined by a FE-SEM (Jeol JSM-6330F) in order to observe the cracks and measure their length accurately. The detailed indentation conditions were listed in Table 4.1.

4.2 Indentation results and discussion

The contact stiffness and contact area are estimated following our proposed procedure, the elastic modulus and hardness are calculated by Eq. (3.6) and (3.7). Once the elastic modulus and hardness has been determined, the fracture toughness K_{IC} can be calculated from the peak load F_{max} and the corresponding crack length C [1].

$$K_{IC} = k \left(\frac{E_s}{H} \right)^{\frac{2}{3}} \left(\frac{F_{max}}{C^{\frac{3}{2}}} \right)$$
(4.1)

where the coefficient $k = 0.011$ for the Berkovich indenter.

Shown in Fig. 4.2 were the typical load-displacement curves and corresponding impression of indentations obtained from sapphire. There was no crack observed at load applied less than 500mN. When the load was increased up to about 700mN, cracks
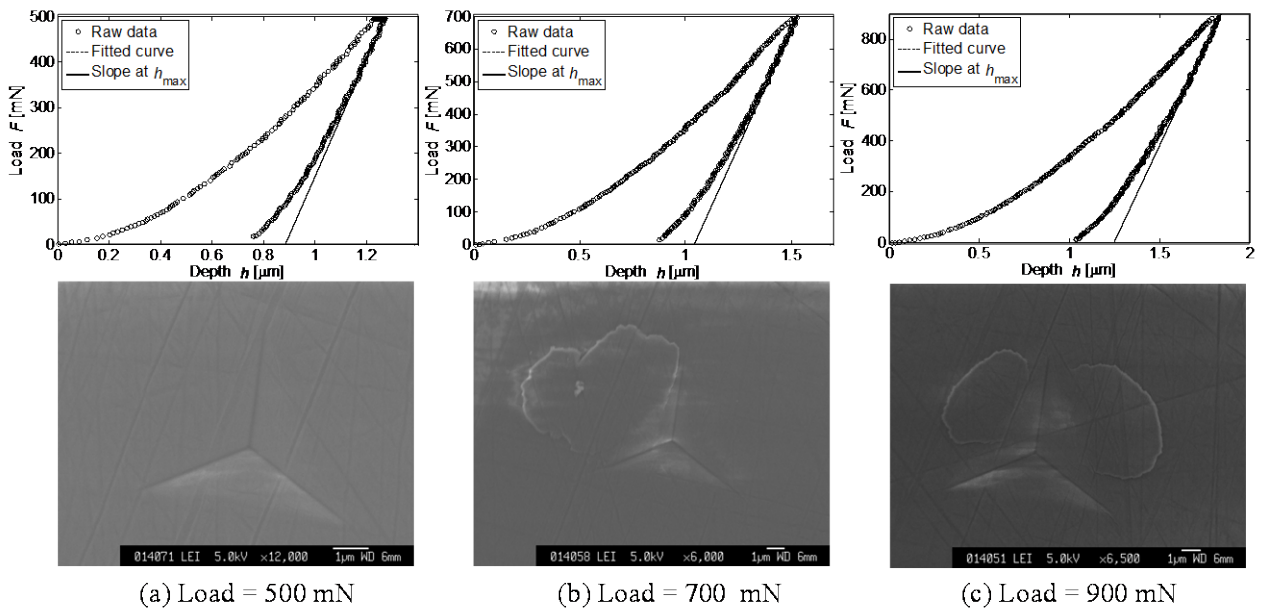

(a) Load = 500 mN　　　　(b) Load = 700 mN　　　　(c) Load = 900 mN

Fig. 4.2 Load-displacement curve and impression of indentation of sapphire

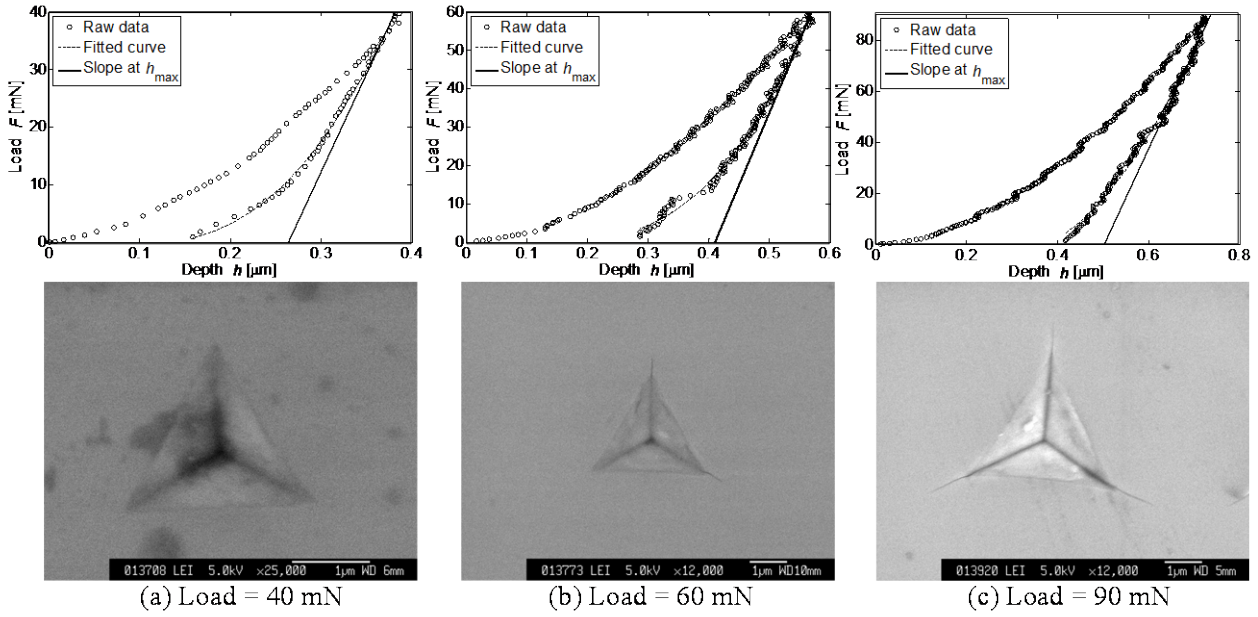(a) Load = 40 mN   (b) Load = 60 mN   (c) Load = 90 mN

Fig. 4.3 Load-displacement curve and impression of indentation of Si

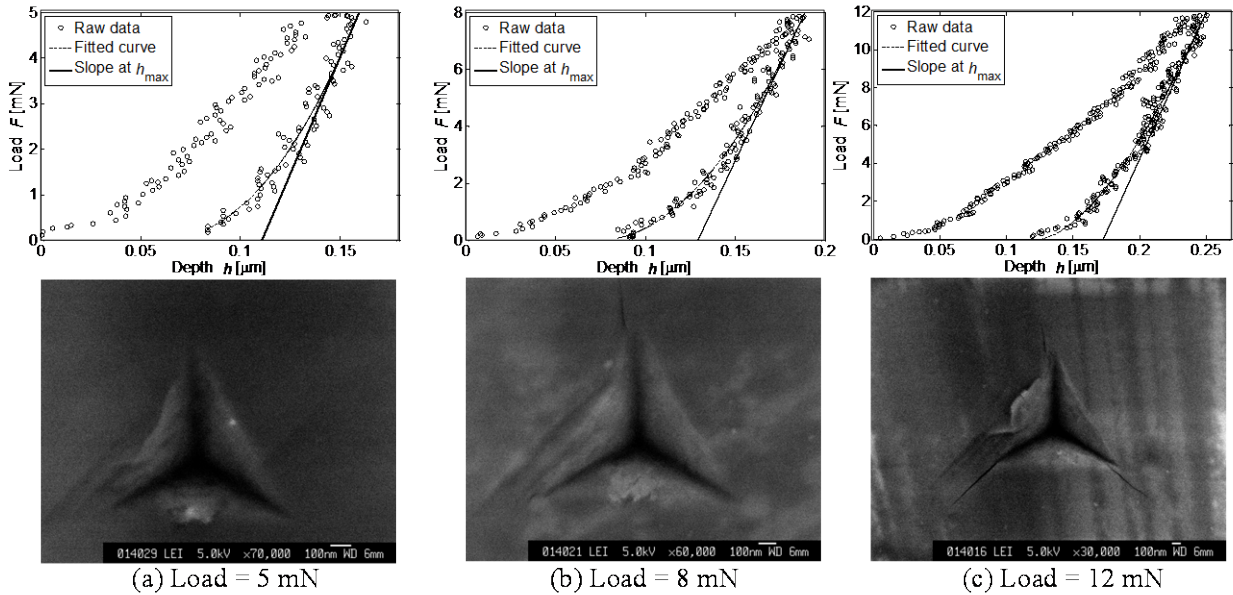(a) Load = 5 mN   (b) Load = 8 mN   (c) Load = 12 mN

Fig. 4.4 Load-displacement curve and impression of indentation of LT

were initiated at the corners of some indents. When the load reaches 900mN, cracks were clearly visible at all three corners of each indentation. The results suggested that the critical load to initiate a crack was about 700mN, and the corresponding critical depth was about 1.5 μm for Sapphire. The load-displacement curves and the corresponding indent impressions were shown in Fig. 4.3 for Si, and in Fig. 4.4 for LT. It was indicating that the critical load and critical depth were about (60mN, 0.55 μm) and (8mN, 0.18 μm) respectively for Si and LT. For each specimen, those load-displacement data below the critical load/depth were used to evaluate the hardness H and the elastic modulus E, while those load-displacement data above the critical load/depth were further used to evaluate the fracture toughness K_{IC}.
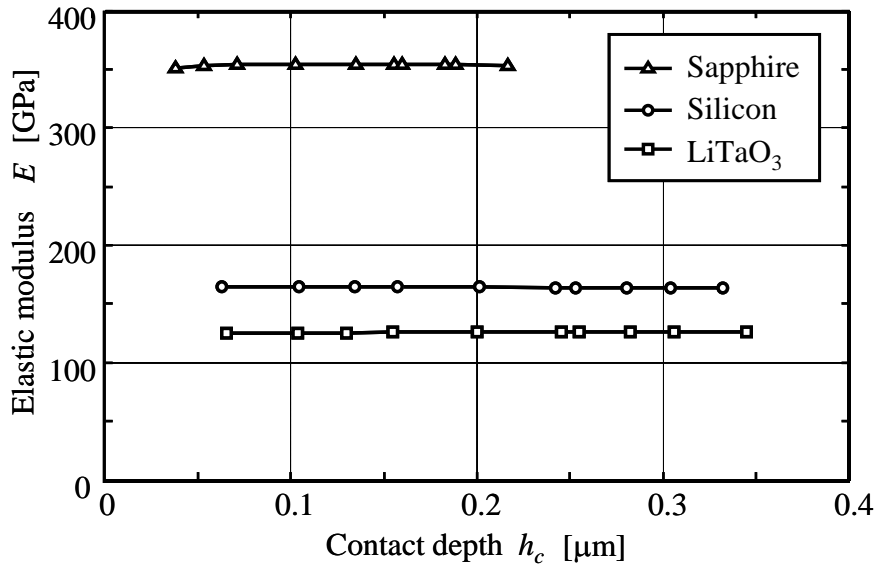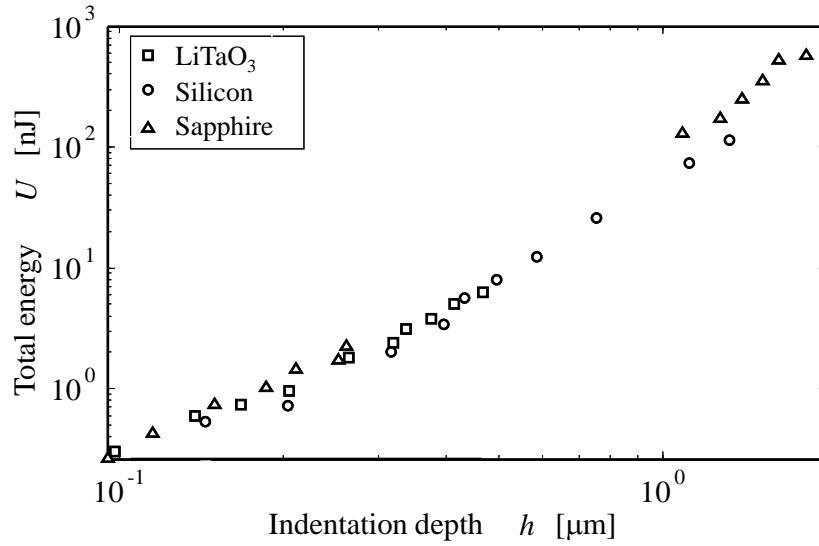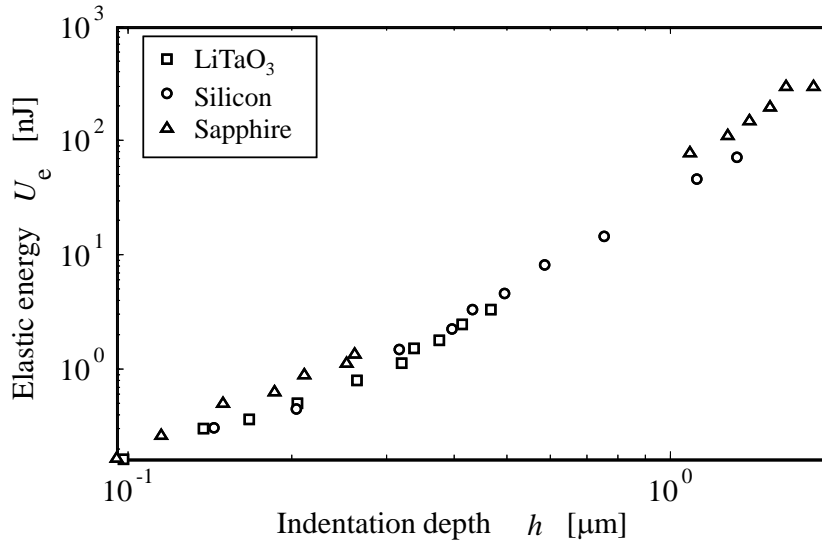
(a) Elastic modulus
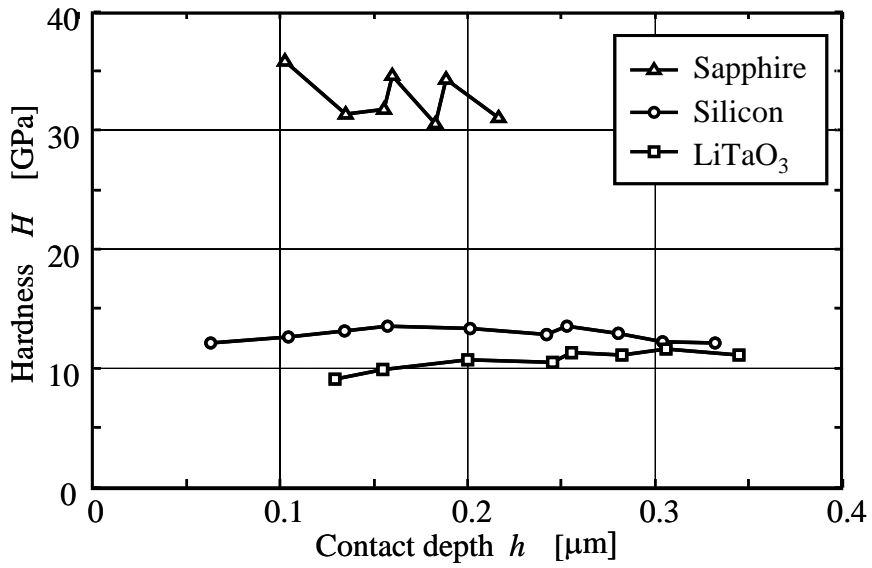
(b) Hardness
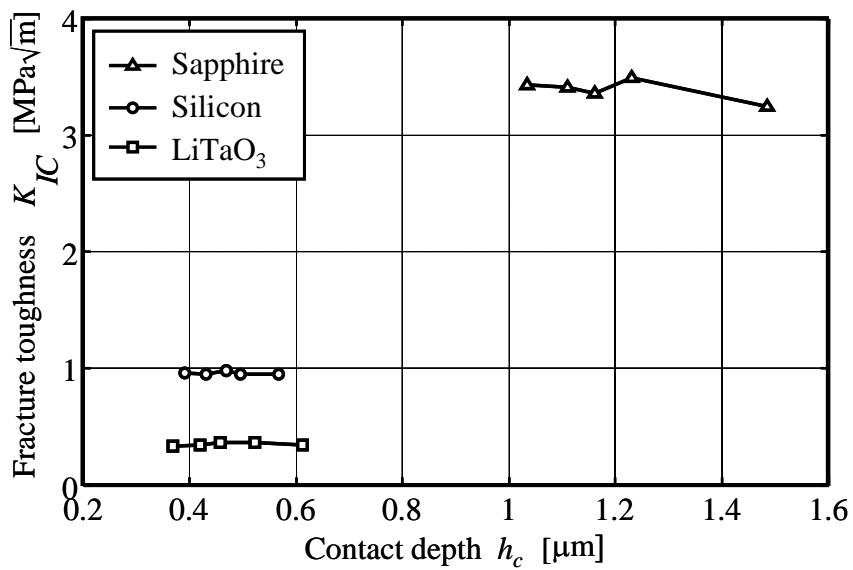
(c) Fracture Toughness

Fig. 4.5 Elastic modulus, Hardness and fracture toughness

(a) Total indentation energy

(b) Elastic energy recovered
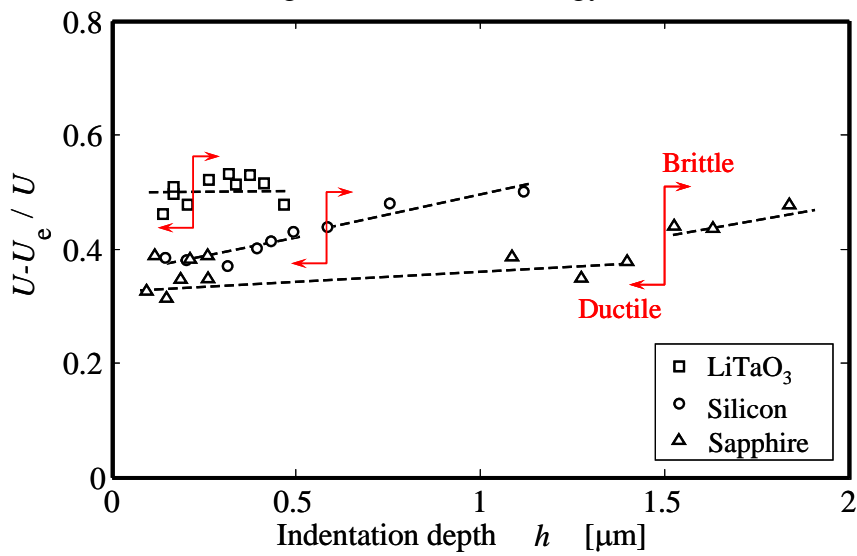Fig. 4.6 Indentation energy

Fig. 4.7 Energy ratio corresponding to material removal

The elastic modulus, the hardness and the fracture toughness of specimens were computed by Eq. (3.1), (3.2), (3.3) and (4.1), and plotted in Fig. 4.5 (a), (b) and (c) respectively as functions of the contact depth. Very little indentation size effect can be seen from results estimated by our newly proposed procedure. In addition, the estimates value of elastic modulus 353GPa for sapphire, 164GPa for Si, and 125GPa for LT were reliable as they are compatible with commonly accepted values [1, 2]. This suggested that the tip area function given in Eq. (3.7) was well compensated at the low load range.

The estimated hardness were 33 ± 3GPa for sapphire, 12 ± 1.1GP for Si and 10 ± 2.3GPa for LT. Among these three crystals, sapphire had both highest elastic modulus and hardness, which stand for the resistances to the elastic deformation and plastic deformation respectively. On the other hand, LT had only one-third of both hardness and elastic modulus of sapphire. This fact characterized LT crystal as a sort of "soft material". In a relative comparison with Si, LT showed resistance to the elastic deformation much less than resistance to plastic deformation, or 14% larger plasticity (rich plasticity).

The fracture toughness KIC of LT was about $0.39\pm0.02\,\mathrm{MPa}\sqrt{\mathrm{m}}$, which was one-third of that of Si, or one-tenth of that of sapphire. This result suggested that LT was a much more "brittle" material in term of crack initiation and propagation, as compared with Si and sapphire. The above analysis led to a conclusion that LT can be characterized as a kind of material with "brittle" and "soft" aspects.

As shown in Fig. 3.1, the total energy consumed in indentation is the integral of load curve from 0 to $h_{\max}$;

$$U = \int_0^{h_{\max}} F_{\text{loading}} \mathrm{d}h \tag{4.2}$$

Upon unloading, a part of U is released together with the elastic recovery.

$$U_e = \int_{h_{\max}}^{h_p} F_{\text{unloading}} \mathrm{d}h \tag{4.3}$$

Shown in Fig. 4.6 were (a) the total energy input into the indentation and (b) elastic energy released upon unloading. Both U and U_e were well matched to a simple power law relation with indentation depth h, despite of the difference in mechanical properties of three crystals.

Shown in Fig. 4.7 was the energy ratio corresponding to material removal. As shown in this figure, LT requires more specific energy for material removal which corresponded to the energy ratio of $(U-U_e)/U$. It was found that the energy ratio below the critical load (where no crack was initiated) for LT was as large as about 50%, while 38% for Si and 32% for sapphire. As a reference of a typical ductile material, aluminum alloy A4043 showed the energy ration as large as 80% [4].

Another fact worthy to note is that the energy ratio for LT was almost kept

constant across the ductile (below the critical load) and brittle (above the critical load) regimes, while the energy ratio for Si and sapphire increased in the brittle regime as compared in the ductile regime. This indicated a fact that LT is so brittle that no or very limited extra energy was demanded to make the cracks propagate once the crack was initiated, while a certain extra energy was required for Si and sapphire to do so.

4.3 Characterization of LT

In order to assess the mechanical property, now, the obtained E, H and K_{IC} of three crystals were plotted in a 3-logarithmic-coordinate as shown by Fig. 4.8 (a), together with some other typical materials like metals (steel and aluminum alloy), ceramics (ZrO_2, Al_2O_3, Si_3N_4, SiC) and amorphous (BK7, soda glass) as references. Those mechanical properties were further projected into (b) K_{IC}-H plane and (c) E-H plane for detailed study of their distribution. From Fig. 4.8 (b), it was noted that the three crystals was distributed much more widely in terms of both hardness and fracture toughness than metals, ceramics and amorphous. Therefore, it is not reasonable to categorize these crystals into one group such as "hard-and-brittle" materials. A new classification is necessary to characterize these crystals like LT. From Fig. 4.8 (c), it was found that those materials clearly fell into two groups; ductile materials (steel, Al) and brittle materials (others). For each group of materials, the hardness was proportional to the elastic modulus logarithmically, which suggested the relationship was possibly described as;

$$H = E^n \tag{4.4}$$

where the power n is an index to address the resistance of material against plastic deformation (hardness) upon its resistance against elastic deformation (elastic modulus). Therefore index n can be used to not only rank those materials in an order of hardness, but also categorize materials into the groups of "ductile" or "brittle".

Fig.4.9 showed the distribution of material properties in map of K_{IC}-n. Those materials fully filled the condition of index $n < 0.2$ and $K_{IC} > 10$ were metals which matches with category of "soft-and-ductile" materials. The materials with $K_{IC} < 10$ were ceramics, crystals and glasses which have been considered as "brittle materials" in engineering field. These "brittle materials" were able to be further classified into two sub-groups subject to their index n and K_{IC}. Those engineered ceramics and sapphire who have $1 < K_{IC} < 10$ and $0.5 < n < 0.7$ belonged to "hard-and-brittle" materials, whereas amorphous and LT could be characterized as a new category of "soft-and-brittle" materials with $K_{IC} < 1$ and $0.2 < n < 0.5$. Silicon crystal fell at the boundary of these two sub-groups.
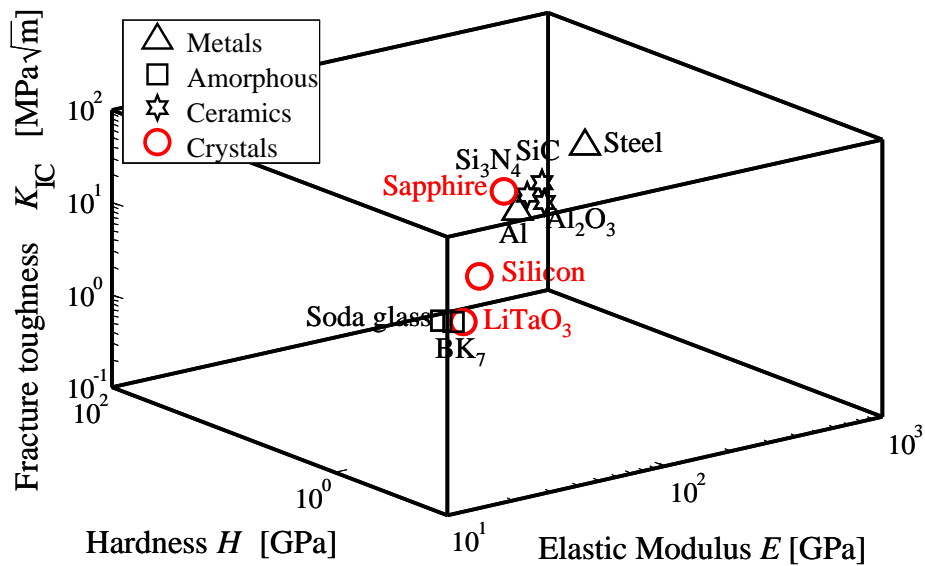
(a) Mechanical properties distribution
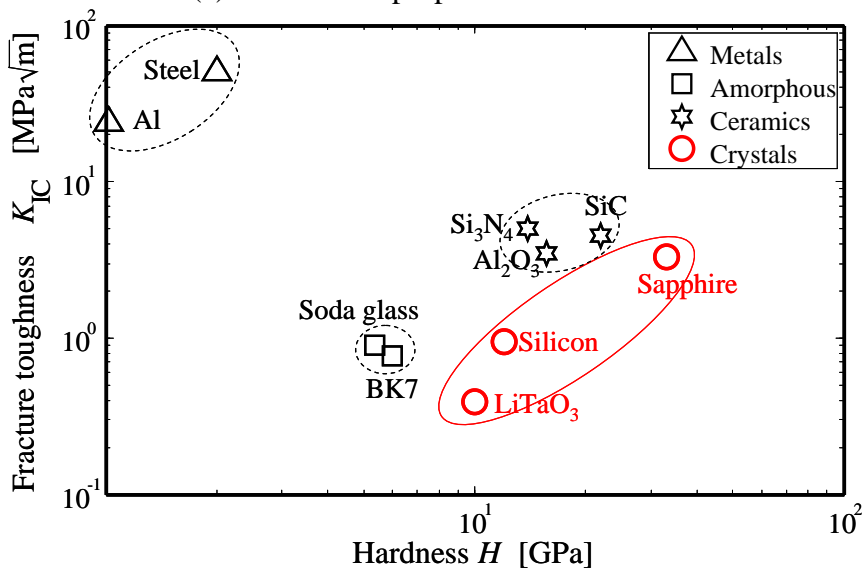
(b) Projection in K_{IC}-H plane
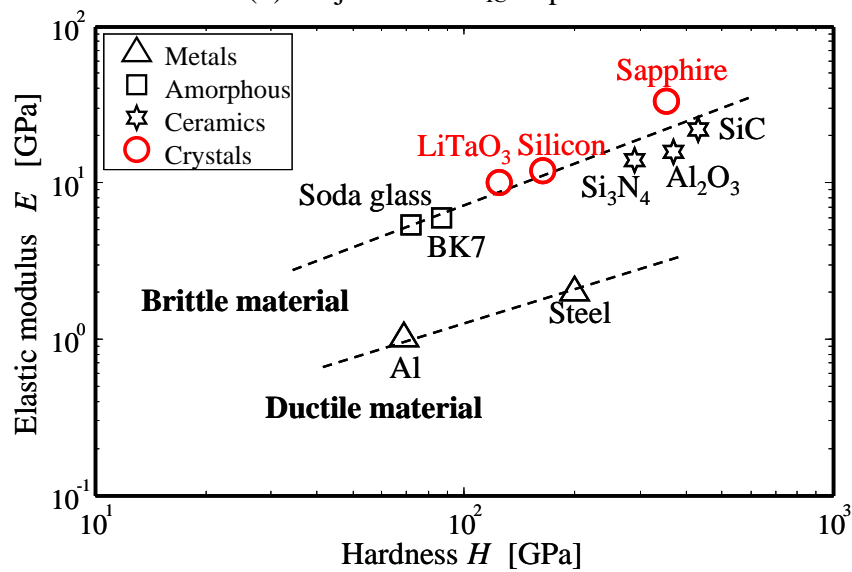
(c) Projection in E-H plane
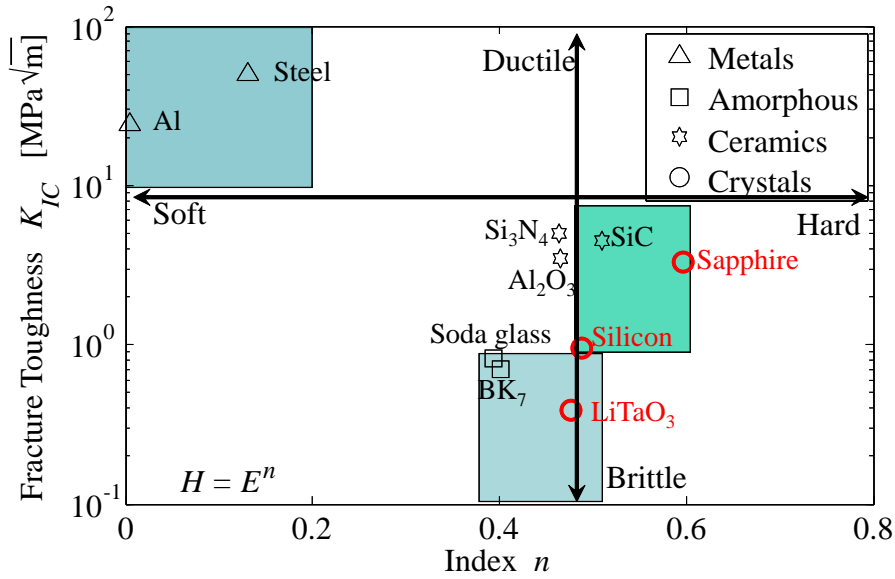Fig.4.8 Mechanical properties distribution
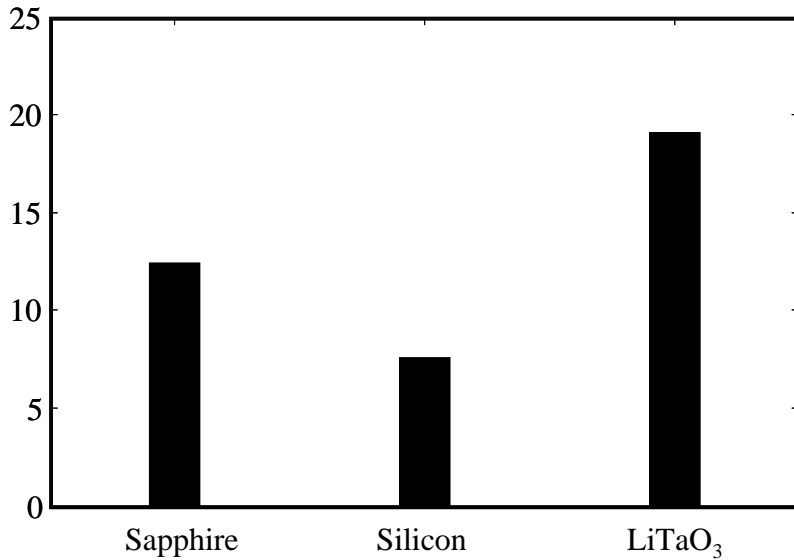
Fig. 4.9 Material classification

Fig. 4.10 Relative comparison of β

Such "soft-and-brittle" materials require special attentions at the machining process, as the knowledge of machining "hard-and-brittle" materials is no longer applicable to this new category of crystals. The most critical issue comes from its brittleness, or extremely low K_{IC}. For most "hard-and-brittle" materials, the critical cutting depth is predicable by Bifano's formula [5];

$$d_c = \beta \frac{E}{H} \left(\frac{K_{IC}}{H} \right)^2 \tag{4.5}$$

where β is a constant subject to the material. Most "hard-and-brittle" materials take $\beta = 0.15 \sim 0.16$ [6]. Assuming that the critical cutting depth d_c is correlated to the critical indentation depth d_I, Fig.4.10 showed a relative comparison of β among three crystals, by take a fraction of $d_I / \frac{E}{H} \left(\frac{K_{IC}}{H} \right)^2$. It was found that LT had the fraction twice higher than other two crystals, which expected the DOC of "soft-and-brittle" materials

is larger than the prediction by Eq. (4.5). However, due to its extremely low K_{IC}, LT requires almost no extra energy to grow the cracks once they are initiated.

The second most critical issue is that LT demands large specific energy for material removal due to its relatively rich plasticity. Because most machining energy is eventually converted into heat, strong anisotropic materials like LT highly risk in thermal crack due to a rapid change in temperature. To achieve high quality machining of LT, it is therefore essential to control and equalize the temperature of workpiece. Two valuable options are expected to be; development and use of high thermal conductive grinding wheels, and effective cooling system. The results will be reported in the chapter 6.

4.4 Summary

In this paper, micro/nano-indentation tests were performed on LT, Si and sapphire wafers to study their mechanical properties and the influences on their machinability in the machining process. The obtained results are summarized as follows:

(1) For most materials including metals, ceramics, crystals and amorphous, the hardness was found to have a simple power law relation with the elastic modulus and described as $H = E^n$. The power n is introduced as a new index which can be used to not only rank those materials in an order of hardness, but also categorize materials into groups of "ductile" or "brittle".

(2) Subject to their index n and K_{IC}, the "brittle materials" are able to be further classified into two sub-groups. Those engineered ceramics and sapphire who have $1 < K_{IC} < 10$ and $0.5 < n < 0.7$ belong to "hard-and-brittle" materials, whereas amorphous and LT can be characterized as a new category of "soft-and-brittle" materials with $K_{IC} < 1$ and $0.2 < n < 0.5$. Silicon crystal fell at the boundary of these two sub-groups.

(3) For "soft-and-brittle" like LT, no or very limited extra energy is demanded to make the cracks propagate once the they are initiated, while a certain extra energy was required for Si and sapphire to do so.

(4) "Soft-and-brittle" like LT expects the depth of cut larger than the prediction by Bifano's formula, and requires particular attention to thermal influence on crack initiation.

Reference

[1] Y.L. Shi, C. Zhang and H. Zhang, et. al: "Low (sub-1-volt) halfwave voltage polymeric electro-optic modulators achieved by controlling chromophore shape", *Science*, Vol. 288, (2000), pp.119-122.

[2] J.J. Worthman, "Young's mudulus, shear modulus and poisson's ratio in silicon and germanium", *Journal of Applied Physical*, Vol. 36, Iss. 1, (1965), pp. 153-156.

[3] G. N. Merberg and J. A. Harrington: "Optical and mechanical properties of single-crystal sapphire optical fibers", *Applied Optics*, Vol. 32, Issue 18, (1993), pp. 3201-3209.

[4] D. L. Joslin and W.C. Oliver: "A new method for analyzing data from continuous depth-sensing microindentation tests", *Journal of Material Research*, Vol. 5, Iss. 1, (1990), pp. 123-126.

[5] T. G. Bifano, T. A.Dow and R. O. Scattergood, "Ductile-regime grinding: A new technology for machining brittle materials", *ASME Journal Engineering for Industry*, Vol. 113, No. 2, (1991), pp. 184-189.

[6] H.T. Young, H.T. Liao and H.Y. Huang:"Novel method to investgate the critical depth of cut of ground silicon wafer", J. Mater. Process. Tech., Vol. 182, 2007, pp. 157-162.W.B. Spillman, Jr..N. A. Sanford and R. A. Soref, "Optical waveguides in LiTaO3 formed by proton exchange", *Optics Letters*, Vol. 8, Issue 9, (1983), pp. 497-498.

Chapter 5 Grinding of LiTaO₃

In this chapter, a grinding model is firstly established for wafer machining process, followed by the theoretical analysis about the calculation the specific energy of material removal and grinding force of "soft-and-brittle" materials according this model. And then, a series of grinding experiments were carried out on LiTaO₃ and Si for the comparison of specific energy and the distribution of grinding force. The experimental results indicate that the physical properties of "soft-and-brittle" material play more important role in the grinding process than the mechanical properties themself.

.

5.1 Wafer grinding model

The most commonly model of wafer grinding is shown in Fig. 5.1, in which the wafer was mounted on the porous ceramic vacuum chuck. During face grinding, the grinding wheel and the wafer rotated about their own rotational axes simultaneously, while the grinding wheel was also moved towards the wafer along the vertical axis. The rotation axis of the grinding wheel was offset by a distance of the wheel radius relative to the rotation axis of the wafer.

The necessary grinding parameters are listed as following:

J_s: The specific energy of material removal in wafer grinding [J/mm³]

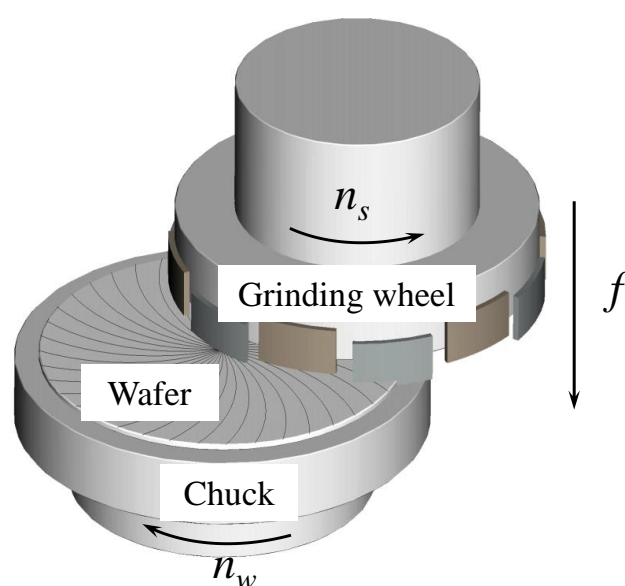f:　down-feed rate [μm/min]

r_s: wheel radius [mm]

Fig. 5.1 The schematic illustration of wheel and wafer configuration during grinding

r_1: The distance between the center of wafer and cutting edge [mm]

r_w: wafer radius [mm]

n_s: rotational speed of wheel [rpm]

n_w: rotational speed of wafer [rpm]

P: the power consumed in wafer grinding [W]

The specific energy J_s is a very important index and defined as removal energy of per unit volume of material removal. The specific energy can be computed from:

$$J_s = \frac{P}{V_{MRR}} \qquad (5.1)$$

where P is power consumed by wheel spindle per unit time and V_{MRR} is the material removal rate. According to the illustration shown in Fig. 5.1, the removal volume is given as:

$$V_{MRR} = \frac{\pi r_w^2 f}{1000} \qquad (5.2)$$

Then the Eq. (5.1) can be rewritten as:

$$J_{s=} \frac{60P}{\pi r_w^2 f} \times 10^3 \qquad (5.3)$$

The consumed power P can be estimated from the experiments, it is noted that the specific energy of material removal can be computed from Eq. (5.3) when r_w is the wafer radius and f is a setting parameter.
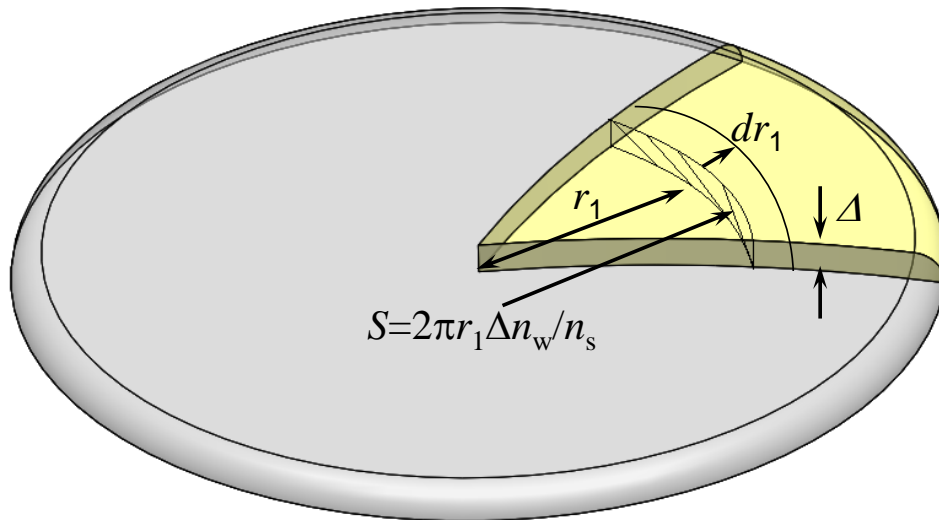

Fig.5.2 The removal mode of wafer grinding in one rotation

The grinding force and its distribution along wafer radius are also very important to the grinding results. And it was also able to be computed from this model. During one rotation of grinding wheel, as showed in Fig. 5.2, the removed material is fan-shaped and marked as white. The short distance along the radius direction for integral calculation is defined as dr_1 and the arc section of fan-shape is defined as S_{rev} and it can be computed as;

$$S_{rev} = 2\pi r_1 \Delta \frac{n_w}{n_s} \tag{5.4}$$

where Δ is the depth of cut in the face grinding model of Fig. 5.1 for the wheel depth of cut is estimated as:

$$\Delta = \frac{f}{n_w} \times 10^{-3} \tag{5.5}$$

Combined with the Eq. (5.5) and (5.6) can be rewritten as the following:

$$S_{rev} = 2\pi r_1 \frac{f}{n_w} \frac{n_w}{n_s} \times 10^{-3} = 2\pi r_1 \frac{f}{n_s} \times 10^{-3} \tag{5.6}$$

The arc section of fan-shape for a unit time removal rate S_{MRR} can be computed by multiplying S_{rev} by the rotational speed of wheel n_s:

$$S_{MRR} = S_{rev} \times n_s = \frac{1}{30}\pi r_1 f \times 10^{-3} \tag{5.7}$$

The material volume removal rate dV_{MRR} at $[r_1, r_1+dr_1]$ can be calculated from the following equation:

$$dV_{MRR} = S_{MRR} \times dr_1 = \frac{1}{30}\pi r_1 f \times 10^{-3} dr_1 \tag{5.8}$$

The power consumed for V_{MRR} is given as:

$$dP = J_s \times dV_{MRR} = \frac{J_s\pi}{30} f r_1 \times 10^{-3} dr_1 \tag{5.9}$$

The linear velocity of wafer is defined as:

$$v = \frac{2\pi r_s n_s}{60} \tag{5.10}$$

According to $= \frac{P}{v}$, combined with Eq. (5.9) and (5.10), the distribution of grinding force is given as:

$$dF_t/dr_1 = \frac{dP}{v} = \frac{J_s}{r_s} \frac{f}{n_s} r_1 \tag{5.11}$$

5.2 Wafer grinding experiments
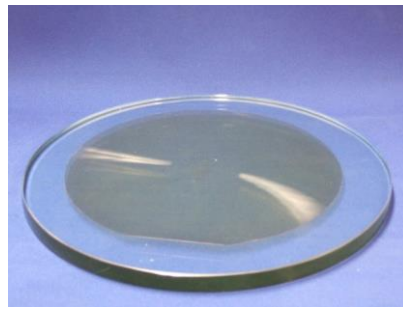
5.2.1. Grinding test conditions

Grinding tests were conducted on a UPG-150H, as shown in Fig. 5.3 (a), which is ultra-precision face grinding machine specially designed for wafer process. A wafer

(a) Grinding machine

(b) Heart-type grinding wheel   (c) 6 inch LiTaO$_3$ wafer   (d) 8 inch Si wafer

Fig. 5.3 The figures of test instruments

Table 5.1 Grinding test conditions

Parameters	Test setting
Grinding wheel	SD3000C160V Heart-diamond
Work piece speed n_w [rpm]	50
Wheel speed n_s [rpm]	1200
Feed rate f [μm/min]	1, 2, 3, 4, 5, 6, 7, 8, 10
Wafer type	6 inch LiTaO$_3$ wafer ($01\bar{1}0$) 8 inch Silicon wafer (100)
Coolant	Pure water
Coolant temperature T [°C]	5

adhered rigidly to substrate was mounted on the porous ceramic vacuum chuck. During face grinding, the grinding wheel and wafer were half overlapped and rotated at their own rotational axes simultaneously, while the diamond wheel was moved towards the wafer at a specified feed rate. As shown in Fig. 5.3 (b), Heart type of diamond cup wheel was employed for grinding experiments based on our previous research report [1]. The heart-type wheel has a better ability to reduce the grinding heat and thermal influence by its effective cooling and self-sharpening ability. Fig. 5.3 (c) showed the workpiece samples of six-inch (150 mm in diameter) LiTaO$_3$ wafer of thickness ranging 350 to 380 μm and eight-inch (200 mm in diameter) Silicon wafer. The coolant temperature was purposely controlled at 5°C. Additionally, a glass plate was chosen as the substrate to host the LT wafers (Fig. 5.3 (c)) for grinding.

Prior to grinding, the diamond wheels were conditioned and dressed on-machine by a very soft GC ring (a Green SiC wheel). Sufficient dressing was performed to ensure that each diamond wheel was well trued and their initial surface status remained consistent [2]. Instead of grinding force, the grinding power of spindle was monitored and recorded through the inverter of wheel spindle motor. The surface roughness of ground wafers was measured by use of an optical surface interferometer (Zygo NewView 200). The rest test conditions were listed in Table 5.1.

5.2.2. Results and discussion

Because of the inverter used for the grinding machine, the current used in the spindle can be recorded in computer via an AD converter. Following the instrument manual, the current can be calculated from recorded date multiply by 4.166666. Meanwhile, three-phase 200 voltage used for the wheel spindle motor, hence, the effective value of voltage is given as $200 \times \frac{\sqrt{2}}{2}$. Finally, the consumed power can be can can be calculated from the following equation;

$$P = 200 \times \frac{\sqrt{2}}{2} \times 4.166666 \times \text{recorded data} \qquad (5.12)$$

Showed in Fig. 5.4 was typical result of consumed power obtained from grinding process of silicon. Due to the high frequency inverter used for the grinding machine, the recorded data of grinding power varied significantly, hence it was filtered and showed as solid line prior to the subsequent analysis.

As shown in Fig. 5.4, in the air-cut stage the consumed power around 323[W] represented the power required to run the wheel spindle. The incremental power above 323[W] was the power consumed for material removal. With increasing the in-feed, the grinding power was stabilized at 953[W] for grinding of Si. As the introduction in
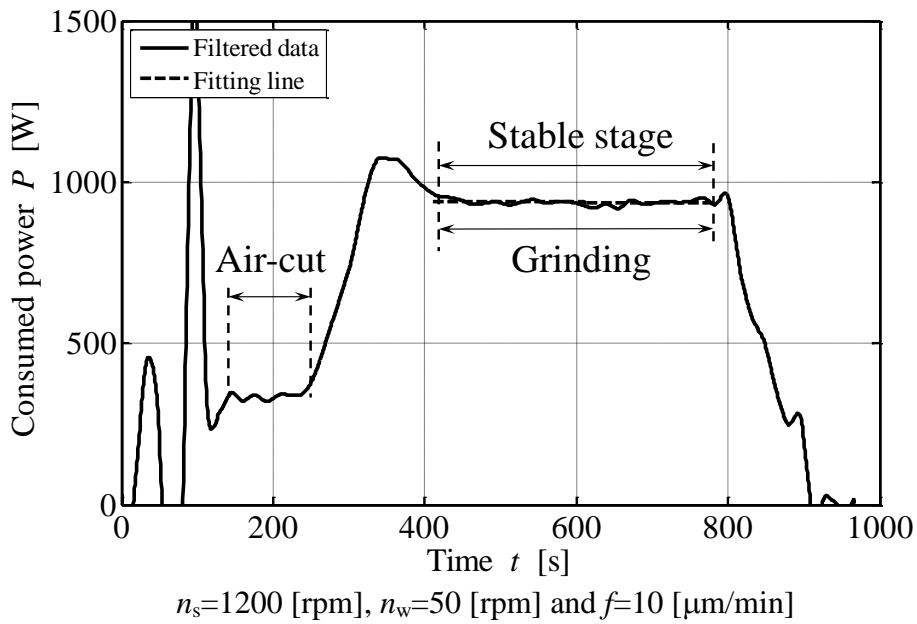
n_s=1200 [rpm], n_w=50 [rpm] and f=10 [μm/min]

Fig. 5.4 The typical consumed power vs. time of silicon test
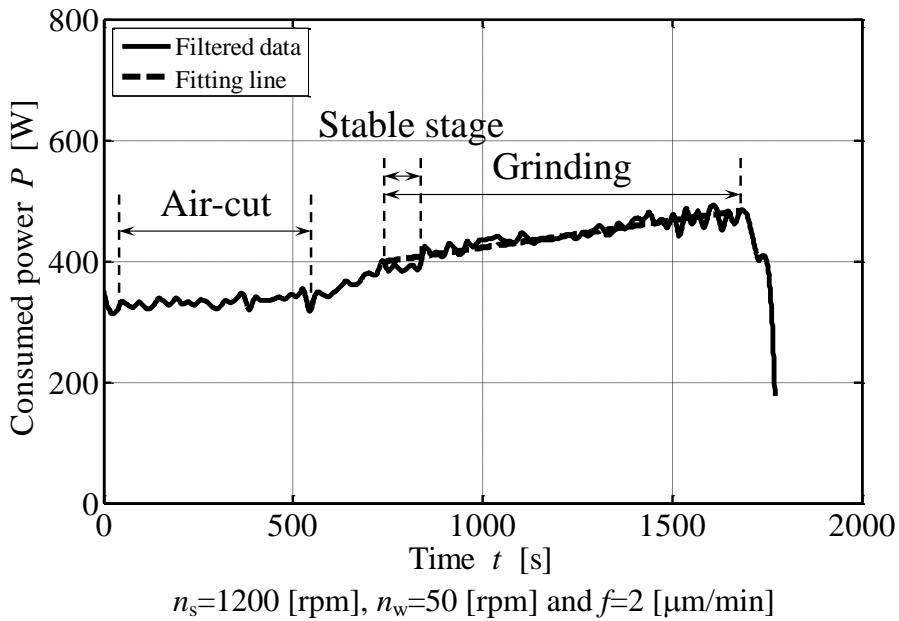

n_s=1200 [rpm], n_w=50 [rpm] and f=2 [μm/min]

Fig. 5.5 The typical consumed power vs. time of LiTaO$_3$ test

previous section, the average power of grinding stage can be used for the calculation of Js. And the slope of fitting line obtained from consumed power at grinding process was equivalent to the increasing rate of tangential grinding force, which is a very important index to evaluate the dynamic behavior of grinding wheel for the subsequent analysis. As shown in Fig. 5.4, the grinding of silicon can be kept stable for a long time until the end of machining process.

Table 5.2 The experimental results of silicon grinding

Feed rate f [μm/min]	Consumed power P [W]	Increasing rate K [W/s]
1	497.74	-0.02
2	552.46	0.02
4	665.04	0.09
5	724.26	0.1
6	847.61	0.06
7	872.38	-0.02
8	921.77	0.06
10	996.13	-0.06
10	953.68	0.02

Table 5.3 The experimental results of LiTaO$_3$ grinding

Feed rate f [μm/min]	Consumed power P [W]	Increasing rate K [W/s]
1	442.34	0.09
2	410.33	0.19
3	421.34	0.24
4 (Cracked)	787.9	0.66
5	525.68	0.29
5	540.38	0.26
6 (Cracked)	793.32	0.65
8 (Cracked)	720.61	0.97

Showed in Fig. 5.5 was typical result of consumed power obtained from grinding process of LiTaO$_3$. Comparison with silicon, the results indicated that the stable stage of LiTaO$_3$ can only be kept for a very limited time and then the grinding power increased continuously. Here, the average data obtained from grinding process was used for evaluation and analysis of machining process for LiTaO$_3$. As the same analysis method used for silicon, the slope of fitting line shown in Fig. 5.5 indicated the incasing rate of tangential grinding force.

Shown in Table 5.2 are the experimental results of silicon. The consumed power and increasing rate of consumed power were listed in this table. In order to confirm the

$$P_{Si}=53.57 \times f+459.54$$

$$P_{LT}=43.11 \times f+337.68$$
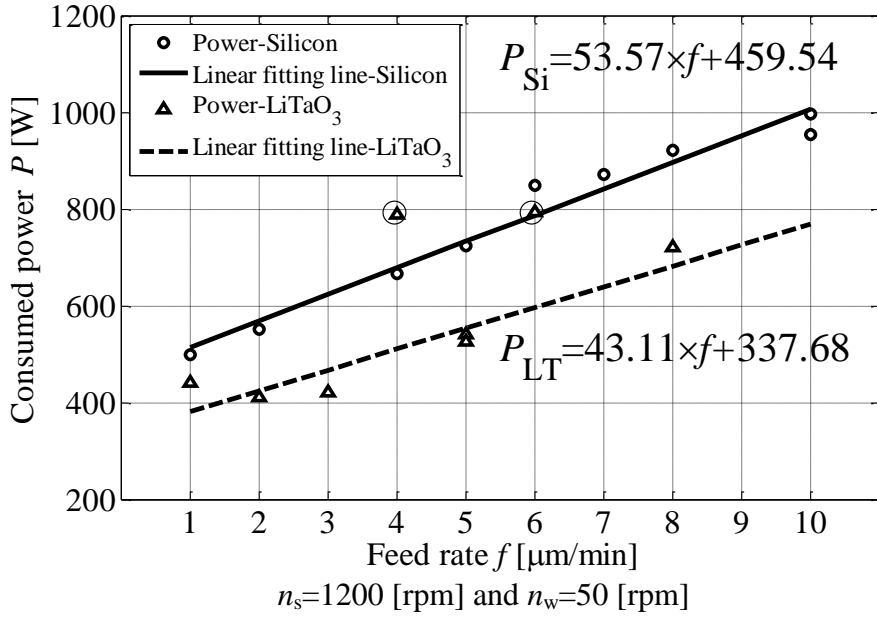
$n_s=1200$ [rpm] and $n_w=50$ [rpm]

Fig. 5.6 The figure of consumed power P vs. feed rate f for LT and Si

repeatability of experiments, the grinding tests were carried out twice at the feed rate of 10μm/min. All these silicon grinding experiments were performed successfully and none cracks were observed on the ground surface.

Shown in Table 5.3 are the experimental results of LiTaO₃, all the grinding tests were carried out only one time except these tests at feed rate of 5[μm/min] which was repeated twice. The cracks were generated on the ground surface when the feed rate is 4, 6 and 8[μm/min].

Shown in Fig. 5.6 are the relationship between consumed power and feed rate for Si and LT, regardless of difference in wafer materials, the consumed power presented a linear relationship with the feed rate as expected, which has a good agreement with the theoretical analysis results in the previous section. However, the consumed power of LT with the feed rate is 4 and 6[μm/min] is unreliable because these wafers were broken during grinnding. Hence, these data are excluded for the subsequent analysis. By linear fitting, the relationship between consumed power P and feed rate f are shown as following:

$$P_{Si}=53.57 \times f \tag{5.13}$$

$$P_{LT}=43.11 \times f \tag{5.14}$$

Combined the Eq. (5.3) with (5.13), the specific energy of Si can be computed as following:

$$J_{s-Si} = \frac{53.57 \times 60}{\pi r_w^2} = 102.31\ [J/mm^3]$$

Here, the r_w is the radius of silicon wafer, r_w=100mm for the 8 inch silicon wafer.
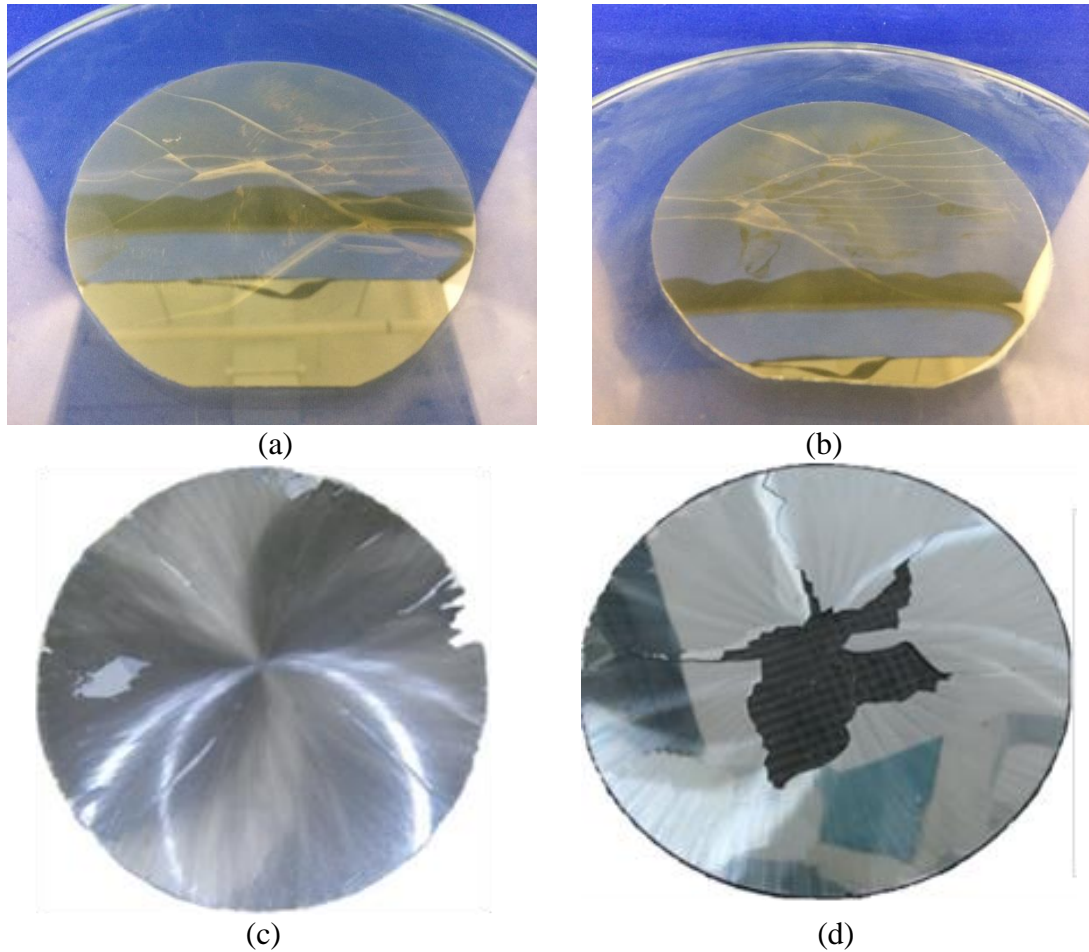
Fig. 5.7 The broken wafers of LT (a, b) and Si (c, d)

Use of the same calculation method for LT, the specific energy of LT can be computed as following:

$$J_{s-LT} = \frac{43.41 \times 60}{\pi r_w^2} = 147.46 \ [J/mm^3]$$

Here, r_w=75mm for 6 inch LT wafer. When we made a comparison between Si and LT, it is noted that the specific energy of LT is larger than that of Si which means LT requires more energy (44% larger than Si) for material removal in the machining process. It provided a good agreement with the results of indentation in chapter 4. From the indentation results, as shown in Fig. 4.7, LT requires more energy (12% larger than Si) for material removal which corresponded to the energy ratio of $(U-U_e)/U$.

Compared with Si, LT shows only 83% in hardness but requires more energy (12% larger than Si) for material removal in the machining process. The reason behind this fact may become an important key of the machining of LT.

The Fig. 5.7 (a, b) and (c, d) are the broken wafers of LT and Si. As shown in Fig. 5.9, it is clearly found that the cracks were fully distributed over the ground LT wafer surface. On the contrary, the cracks only partly distributed on the ground Si wafer
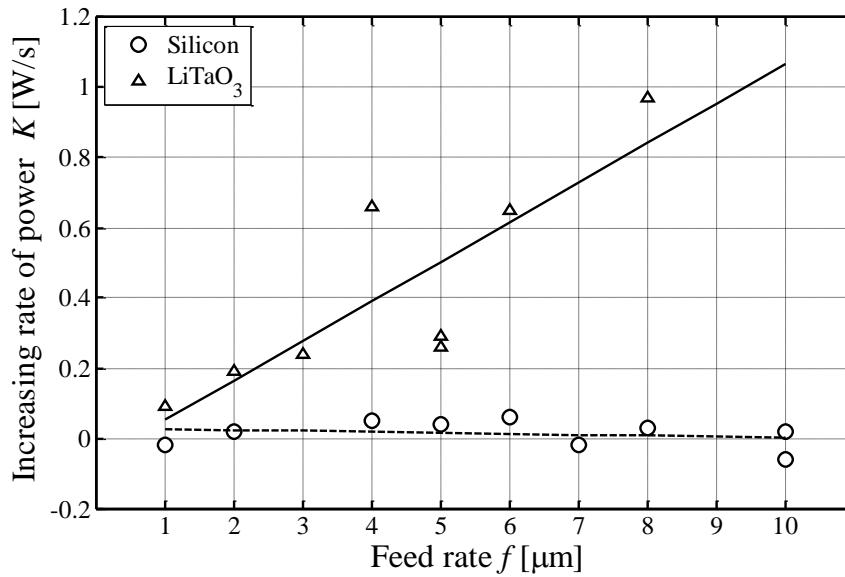
Fig. 5.9 The increasing rate K vs. feed rate f for LT and Si

surface. It indicated a fact that LT is so brittle that no or very limited extra energy was demanded to make the cracks propagate once the crack was initiated, while a certain extra energy was required for Si. It also well agreed with the results of indentation in chapter 4.

According to the Eq. (5.11), the distribution of grinding force f for LT and Si is plotted in Fig. 5.8. The results indicated that the grinding force of LT is larger than that of Si at the same distance from the center of wafer. The grinding force of LT is 42% larger than that of Si when the distance from the center is 60mm.

The Fig.5.9 is the relationship between the increasing rate K of grinding power and feed rate f. As shown in Fig. 5.9, the increasing rate of silicon had little deviation at the range from -0.2 to 0.2W/s which indicated that the grinding power or force of silicon was very stable in the whole grinding stage with no wafer broken. The silicon wafers were resulted in successful grinding. By comparing the grinding results of LT with silicon, it is found that the increasing rate had a linear relationship with the increase of feed rate. Though grinding experiments of LT and Si were carried out at the same conditions, it was also found that the power is always kept increasing in the grinding process of LT. In other words, the increasing rate of LT has a linear relationship with the increasing of feed rate and the cracks were easily generated on the LT ground surface. It was difficult to find an explanation from the mechanical properties of LT based on the traditional knowledge about machining of hard-and-brittle materials. However, LT has some unique properties which introduced in chapter 1. Hence, the physical properties like pyroelectric and piezoelectric properties may play an important role in the grinding process. It needed to consider the influence of physical properties on LT grinding process.

5.3 Summary

In this chapter, a wafer grinding model is firstly established for wafer machining, followed by the theoretical analysis about the calculation of the specific energy of material removal according this model. And then, a series of grinding experiments were carried out on LiTaO$_3$ and Si for the evaluation of specific energy of material removal. The obtained results are discussed in association with results of indentation and summarized as follows:

(1) A grinding model has been proposed and established to derive the specific energy of material removal.

(2) The hardness of LT is only 83% of that of Si, however, the specific energy of LT is 147.46 J/mm^3 or 44% larger than that of Si. This result is well agreed with the indentation results.

(3) Both the grinding and indentation results indicated a fact that LT is so brittle that no or very limited extra energy was demanded to make the cracks propagate once the crack was initiated, while a certain extra energy was required for Si.

(4) The calculation results indicated a fact that the grinding force of LT is larger than that of Si at the same distance from the center of wafer.

(5) The increasing rate of consumed power played a very important role in the machining of LT. When it was above critical line, cracks were initiated and resulted in wafer broken.

(6) Compared with the grinding results of Si, the increasing rate in the LT grinding experiments had a linear relationship with the increase of feed rate at the same experimental conditions which indicated a fact that the physical properties may play a more important role in the grinding process.

Reference

[1] W. Hang, L. Zhou, J. Shimizu, and J. Yuan: "Study on the thermal influence of grinding process on LiTaO$_3$", *Advanced Material Research*, Vol.797, (2013), pp. 252-257.

[2] L. Zhou, T. Shiina, Z. Qiu, J. Shimizu, et. al, "Research on chemo-mechanical grinding of large size quartz glass substrate", *Precision Engieering*, Vol. 33, (2009), pp. 499-504.

[3] K.Shoji ; The grinding processing, (2004), pp. 88.

[4] S.Matsui, K.Shoji: "An Evaluation of Grinding Performance for Abrasive Wheel", Tec. Rept. Toghoku Univ. Vol41,No2 (1976) K. Länge, B. E. Rapp and M. Rapp, "Surface acoustic wave biosensors: a review", *Annual Bioanal. Chemistry*, Vol. 391, (2008), pp:1509-1519.

Chapter 6 The influence of physical properties on LiTaO₃

The theoretical analysis about the influence of physical properties on the crack initiation is firstly presented in this chapter. In order to suppress the piezoelectric and pyroelectric effects induced by polarization during grinding of LT, control of coolant temperature and use of electrolyte solution are purposely tried in this chapter.

6.1 The joint effects of piezoelectric and pyroelectric in grinding of LiTaO₃

As shown in Fig. 6.1, the piezoelectric effect is a unique property of certain crystals and certain ceramics which will generate an internal electric field subjected to physical stress [1]. The word piezoelectricity comes from Greek and means "electricity by pressure" (Piezo means pressure in Greek). This name was proposed by Hankel [2] in 1881 to name the phenomenon discovered a year before by the Pierre and Jacques Curie brothers [3]. They observed that positive and negative charges appeared on several kinds of crystal surfaces. The piezoelectric effect can be understood as conversion from mechanical energy to electrical energy. The reverse piezoelectric effect can also be observed, as shown in Fig. 6.2, when an external electric field applied on the piezoelectric material like LiTaO₃, stress is resulted from the distortion of its structure. In this kind of situation, the energy is transferred from electrical energy to mechanical energy. The explanation given by Tichy [4] for piezoelectric effect is that the application of the mechanical stress changes the total polarization vector due to the
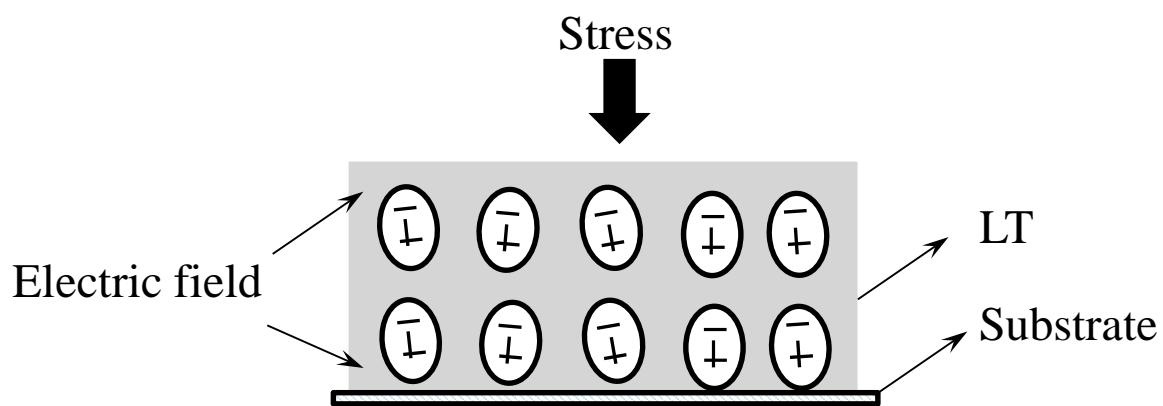
Fig. 6.1 Piezoelectric effect
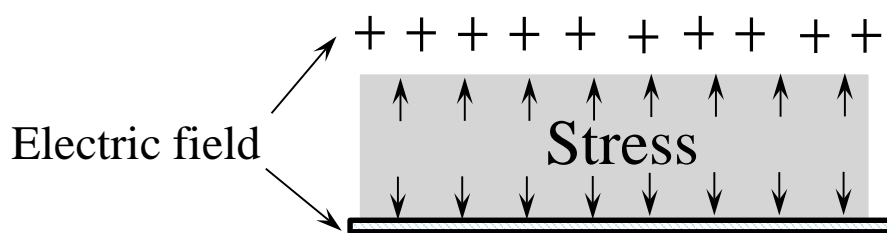
Fig. 6.2 The reverse piezoelectric effect

piezoelectric effect [4].

The piezoelectric effect and its reverse effect are expressed by the following coupling equations:

$$\begin{cases} S = s^E T + dE \\ D = dT + \varepsilon E \end{cases}$$ (6.1)

where the notations are defined as below:

S : strain (%),

T : stress (N/m^2),

E : the strength of electric field (V/m),

D : electric displacement (C/m^2),

s^E : elastic compliance (m^2/N),

d : piezoelectric coefficient (C/N),

ε : dielectric coefficient (F/m).

As shown in Table 6.1, the piezoelectric coefficient of LT at room temperature have been reported by Monchalin [6].

As shown in Fig. 6.3, pyroelectric effect (pyro means fire in Greek) is the ability of certain materials to generate a temporary voltage when the temperature of materials changes [7]. Like the piezoelectric effect has its reverse effect, pyroelectric effect also has reverse effect. As shown in Fig. 6.4, the reverse pyroelectric effect, i.e. the temperature changes according to the external electric field, which is also called electrocaloric effect [8]. The change in temperature modifies the positions of the atoms slightly within the crystal structure, such that the material is polarized. This polarization gives rise to a voltage across the crystal. If the temperature is kept constant for a certain period, the generated pyroelectric voltage gradually disappears due to current leakage.

Every pyroelectric material is necessarily to be piezoelectric material. On the contrary, not all the piezoelectric materials are pyroelectric.

The pyroelectric effect is expressed by the following coupling equations:

$$\begin{cases} D = \varepsilon E + p\Delta\theta \\ \sigma = pE + c\dot{\theta}/\theta \end{cases}$$ (6.2)

Table 6.1 The piezoelectric coefficient of LiTaO$_3$

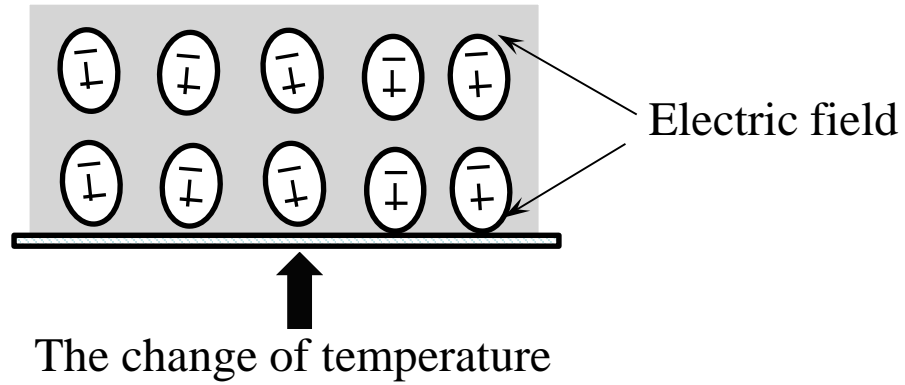| Parameters		
Piezoelectric coefficient d_{ki} (10^{-11}C/N)	d_{15}	2.6
	d_{22}	0.85
	d_{31}	-0.3
	d_{33}	0.92

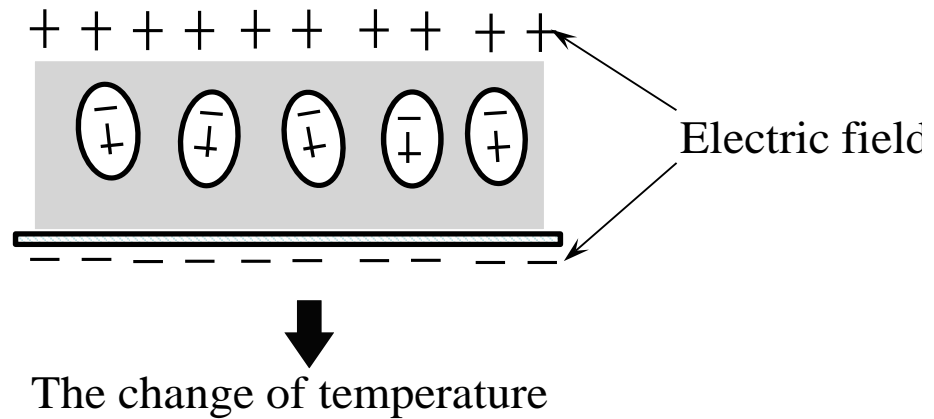Fig. 6.3 The pyroelectric effect

The change of temperature

Fig. 6.4 The reverse pyroelectric effect

where the notations are defined below:

D : electric displacement (C/m^2),

E : the strength of electric field (V/m),

θ : the temperature (ºC),

σ : entropy (J/K),

c: heat capacity (J/C);

The pyroelectric coefficient p of LT at room temperature is listed in Table 6.2 [9].

As the description in the previous chapter LT demonstrates both piezoelectric effect and pyroelectric effect. Hence, the joint effects of piezoelectric and pyroelectric has a strong influence on LiTaO$_3$ during the machining process. The Fig. 6.5 is the schematic illustration of the joint effects of piezoelectric and pyroelectric in grinding of LT. As shown in Fig. 6.5, LT wafer is subject to both external load and heat in grinding process. The internal electrical field is induced and accumulated by polarization.

Table 6.2 The pyroelectric constants of LiTaO$_3$

Parameters	p
Pyroelectric coefficient (10^{-6}C/m^{2}N*ºC^{-1})	-180
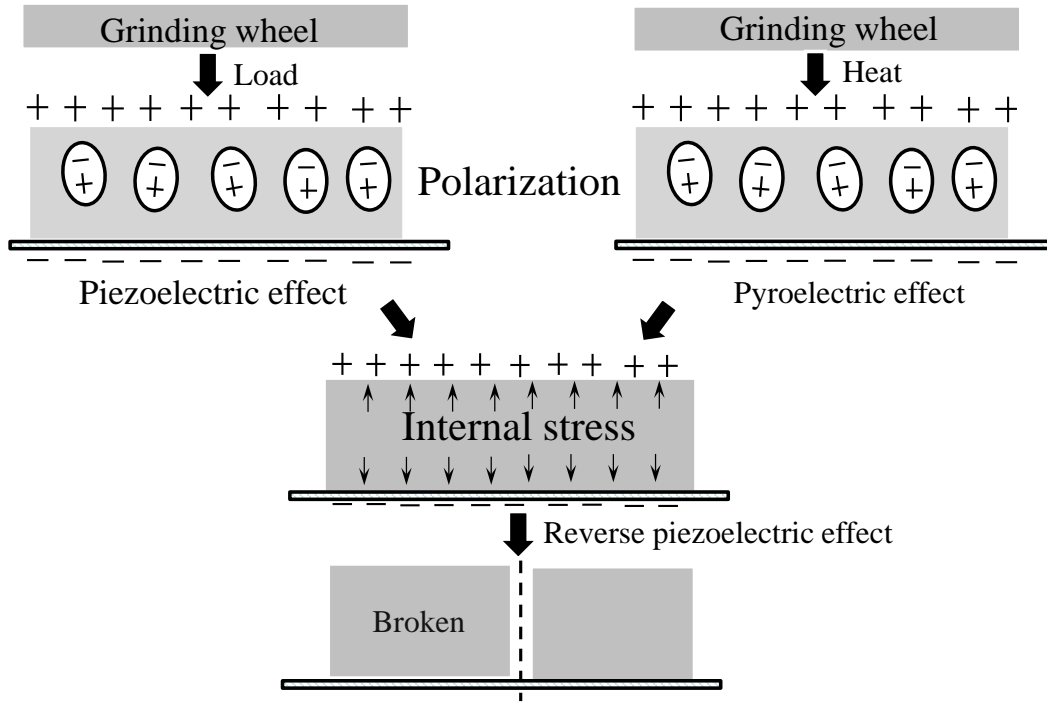
Fig. 6.5 The schematic illustration of joint effects of piezoelectric and pyroelectric in grinding of LiTaO$_3$

Meanwhile,

LT also has reverse piezoelectric effect, internal stress is resulted from the electrical field . The cracks may be iniated by the internal stress.

As shown in Fig. 6.5, both piezoelectric and pyroelectric effect has a influence on LT. By associating with the reverse piezoelectric and pyroelectric effect, the Eq. (6.1) and (6.3) are rewritten as following:

$$\varepsilon E + p\Delta\theta = D = \varepsilon E + dT \qquad (6.4)$$

The internal stress T can be calculated as:

$$T = \frac{p}{d}\Delta\theta \qquad (6.5)$$

Eq. (6.5) suggested that the internal stress is linearly propotional to the change of temperature. When the sum of external stress σ and internal stress T is larger than the strength of material σ_{th}, or $\sigma + T > \sigma_{th}$, the cracks are possibly generated.

The tensile strength of LT is about 38.2 MPa [10]. Fig. 6.6 shows the external stress equired to initiated cracks as a function of temperature change $\Delta\theta$. As shown in Fig. 6.6, it is found that when the the change of temperatureis is 200 ℃, if the external stress is above 15.3 MPa, the wafer will be broken. When the change of temperatureis continu to up to 333 ℃, no external stress is required to initiate cracks on LT wafer surface. Hence for these new functional material like LT, unlike the tradtional knowledge about cracks are usually generatured by the external stress from machining process, the cracks are possible to resulted from the external stress and inner stress
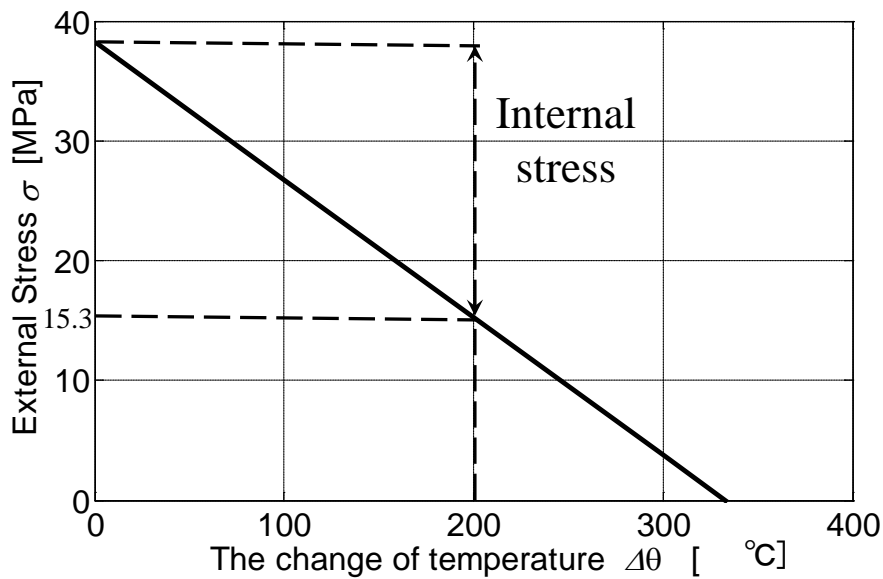
Fig. 6.6 Stress vs. the change of temperature

(a) before heating   (b) after heating
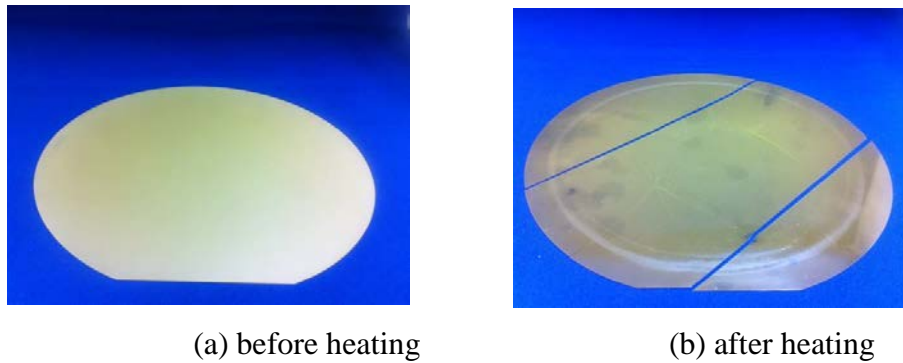
Fig. 6.7 Four inch LiTaO$_3$ wafer

which originated from physical properties. Shown in Fig. 6.7 are four inch LT wafers: (a) before and (b) after heating of 200 ℃ at the load of 40 N. Comparison of these two photos suggests a fact that the cracks can be generated by the change of temperature on LT surface.

As the decription in Chapter 4, LiTaO$_3$ is rich in plasticity and demands larger specific energy for material removal. As the most machining energy is eventually converted into heat, LT undergoes a rapid rise in temperature during the grinding process, thus highly risks in crack iniation by temperature change. In order to suppress the effect of physical properties on the grinding process of LiTaO$_3$, the grinding tests with effective cooling methosds are investigated in next section.

6.2 Experimental details of grinding with effective cooling
6.2.1 Experimental details

Grinding tests were conducted on a UPG-300H, as shown in Fig. 6.8 (a), which is ultra-precision face grinding machine specially designed for wafer process [11].

Six-inch (150 mm diameter) LiTaO$_3$ wafers with thickness ranging 350 to 380 μm were used as work-pieces. Two types of diamond cup wheels were employed for grinding experiments. As shown in Fig. 6.8 (b), both of them are SD3000C160V made by the same manufacturer but with different geometry of tooth type. As compared with conventional segment-type grinding wheel, the heart-type grinding wheel is considered to have lower grinding force and longer dressing interval. The coolant temperature was purposely controlled at 5°C, 15°C, 25°C or 35°C to study its thermal effect. Additionally, two kinds of materials, glass (G) and aluminum alloy (Al) which are 2 digits difference in thermal conductivity, were chosen as the substrates to host the LT wafers (Fig. 6.8 (c)) for grinding.

Prior to grinding, the diamond wheels were conditioned on-machine by a very soft GC ring (a Green SiC wheel). Sufficient dressing was performed to ensure that each diamond wheel was trued and their initial surface status remained consistent. The LT wafer adhered rigidly to substrate was mounted on the porous ceramic vacuum chuck. During face grinding, the grinding wheel and wafer were half overlapped and rotated at their own rotational axes simultaneously, while the diamond wheel was moved towards

(a) Grinding machine
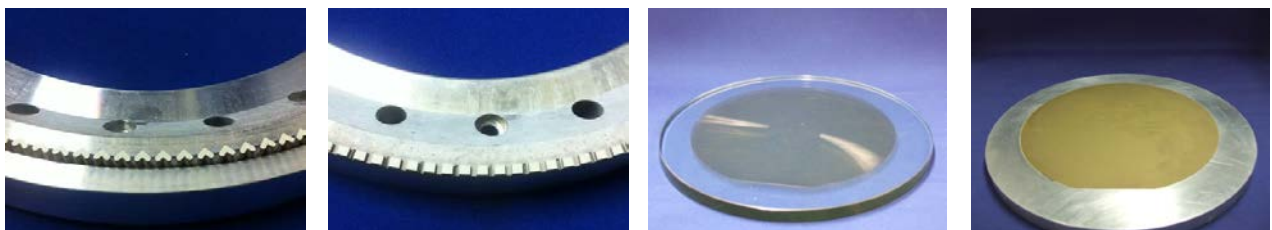
(b) Heart and segment type grinding wheel, (c) six inch LiTaO$_3$ on glass and aluminum substrate

Fig. 6.8 Test instruments of grinding with effective cooling methods

Table 6.3 Test conditions

Parameters	Test settings
Work-piece	6 inch LiTaO$_3$ wafer
Temperature (°C)	5, 15, 25 and 35
Grinding wheel	SD3000C160V
Substrate (Thermal conductivity W/m∗k @25°C)	Glass (1.05) and Al (205)
Grinding wheel speed (rpm)	1300
Work piece speed (rpm)	50
Feed rate (μm/min)	2
Coolant	Pure water

the wafer at a specified   feed rate. Instead of grinding force, the grinding torque was monitored and recorded through the inverter of

wheel spindle motor. The surface roughness of ground wafers was measured by use of an optical surface interferometer (Zygo NewView 200). The rest test conditions were listed in Table 6.3.

6.2.2 Results

Shown in Fig. 6.9 were typical external view of LT wafers ground with coolant of temperature controlled at 35°C. Photo in (a) shows a broken wafer due to cracks with Al substrate and segment wheel type which is hereby marked with (✕). Photo in (b) is a scratched wafer yet to be broken with glass substrate and segment wheel type which is

(a) Broken wafer   (✕)   (b) Scratched wafer   (△)

(c) Succeeded wafer   (○)   (d) Succeeded wafer   (○)
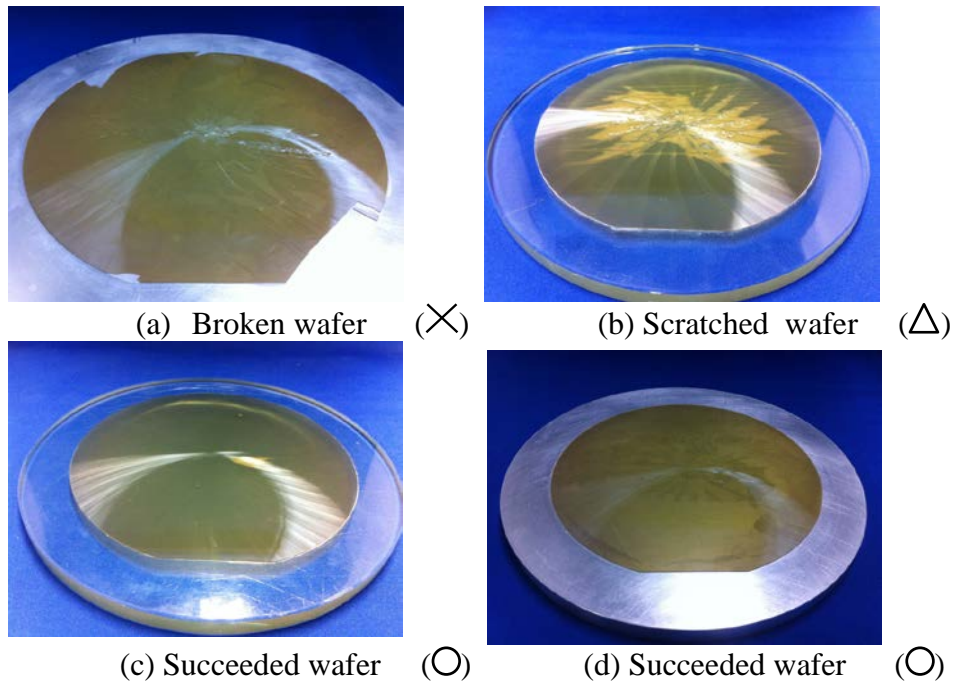
Fig. 6.9 Ground wafers in the experiments with effective cooling methods
(Coolant temperature: 35°C)

Table 6.4 Grinding results of experiments with effective cooling methods

Substrate	Wheel type	Temperature			
		5°C	15°C	25°C	35°C
Glass	Heart	○	○	○	○
Al	Heart	○	×	○	○
Glass	Segment	○	○	×	△
Al	Segment	○	△	×	×

marked with (△). Photos in (c) and (d) show the LT wafers successfully ground on glass and aluminum substrates respectively with heart wheel type. Those succeed wafers, neither cracks no scratches observed on their surfaces, were marked as (○).

Table 6.4 was the summary of grinding results obtained at different test conditions.

$$T_r = 0.6504 \times Z + 1812$$
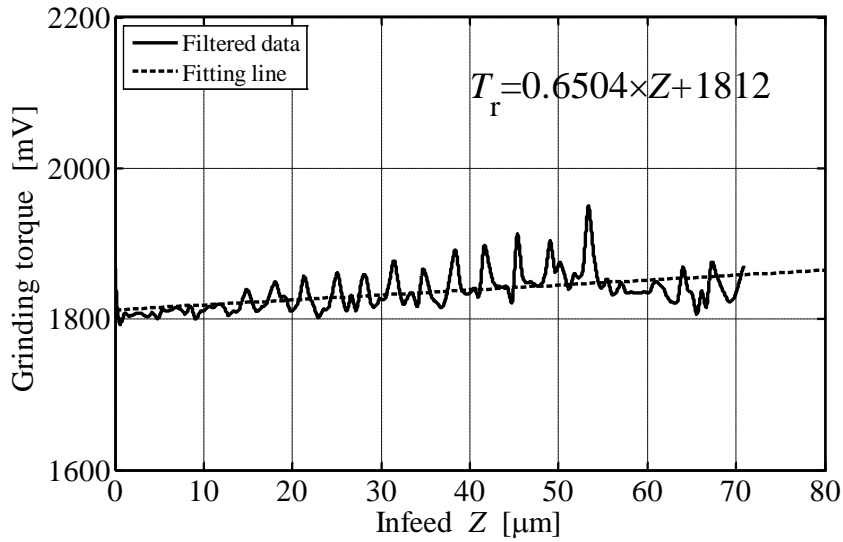
(a) Al substrate, Heart type at 5°C

$$T_r = 2.3189 \times Z + 1791$$
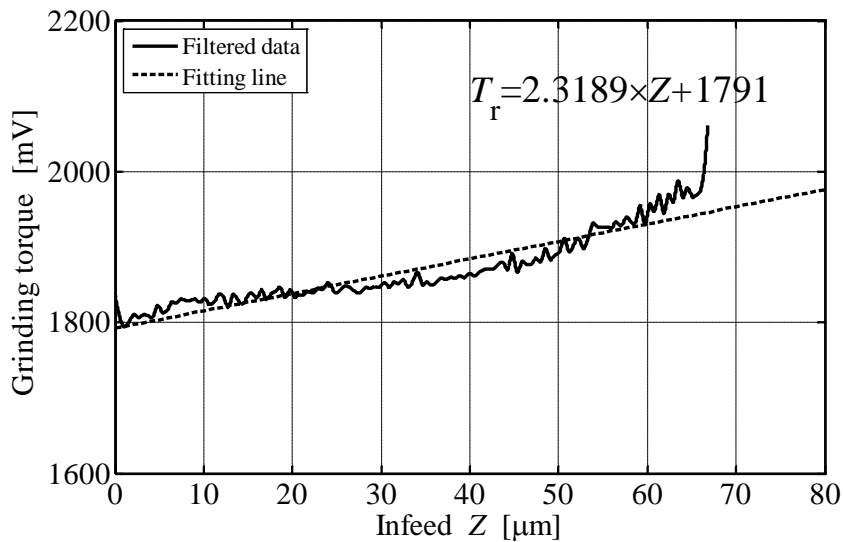
(b) Al substrate, Segment type at 35°C
Fig. 6.10 Typical results of grinding torque

When the coolant temperature was 5°C, all four tests were completed successfully regardless of differences in wheel type and substrate type. When the coolant temperature was increased to 15°C, scratches and cracks were observed on the ground surface by Al substrates. When the coolant temperature was raised to 25°C, wafers were broken with segment-type grinding regardless of the difference in substrate. Similar results were obtained when the coolant temperature further rose up to 35°C. The results suggested that the coolant temperature was critical to successful grinding of pyroelectric crystal like LT. In addition, wheel type also contributed to constrain crack initiation.

Showed in Fig. 6.10 were typical results of grinding torque obtained from grinding process with different substrates, wheel types and coolant temperatures. As the torque measured in this study came from an output port of the spindle motor inverter in the form of voltage, the unit remained as "mV" instead of "Nm" for relative comparison. Due to the high frequency inverter used for the grinding machine, the raw data of grinding torque varied significantly, thus was fitted to a linear line (dashed line) prior to the detailed analysis. The intercept of linear fitting with the vertical axis around 1800 mV represented the power required to run the wheel spindle for air-cut while the incremental power above 1800 mV was the torque consumed for material removal. The slope of fitting line was equivalent to the increasing rate of tangential grinding force, which is a very important index to evaluate the dynamic behavior of grinding wheel and the grinding heat generated during grinding.

Fig. 6.11 showed the relationship between coolant temperature and increasing rate of grinding force (or torque). By associating the results in Fig. 6.9 with Fig. 6.11, it was easy to understand that the increasing rate was a key factor dominating the quality of ground wafers including scratches, cracks and wafer breakage. When the increasing rate was above 1.3 mV/μm, the LT wafer started being scratched. When the increasing rate was further above 2.0 mV/μm, cracks were initiated and resulted in wafer broken. It is therefore essential to control the increasing rate below 1.0mV/μm to make grinding of LT success.

Regardless of changes in wheel type and substrate, it was also noted that the increasing rate remained less than 1.0 mV/μm when the coolant was controlled at low temperature of 5°C. As the temperature of coolant rose, the increasing rate of grinding force was widely divergent, largely dependent on the wheel type or substrate materials.

The reason can be possibly suggested by the influence of joint effects of piezoelectric and pyroelectric on increasing rate of grinding torque. The temperature of LT wafer keeps rising during face grinding. For a piezoelectric and pyroelectric crystal like LT, the internal electrical field is induced and accumulated by polarization which is
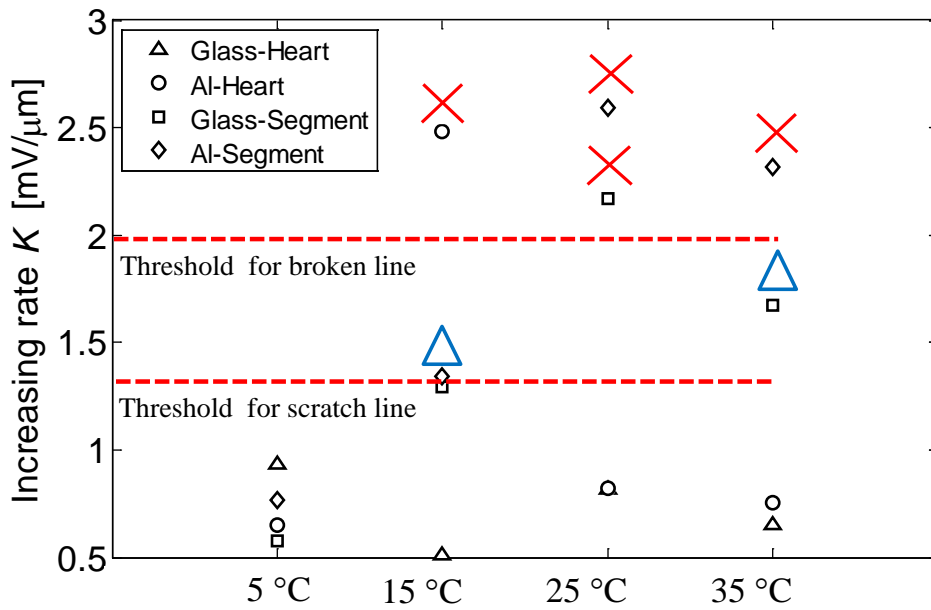
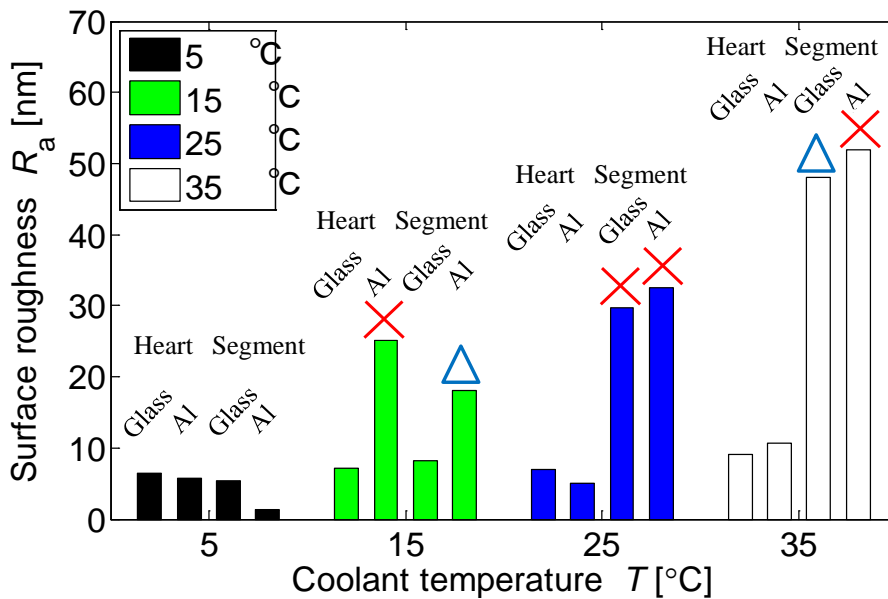Fig. 6.11 Increasing rate of grinding torque

Fig. 6.12 Surface roughness of grinding torque

came from the stress from grinding wheel and the change in temperature. With the influence of joint effects of physical properties, the increasing rate of grinding torque is lager and the wafer turned to be broken easily. Meanwhile, LT also has reverse piezoelectric effect, the internal stress which is resulted from the electrical field was also contributed the generation of cracks. Eventually, the cracks were initiated by enhanced interaction between piezoelectric and pyroelectric effect. It is worthy to note that aspect of LT as a strong piezoelectric material also is an important factor which facilitates the initiation and propagation of cracks. It is therefore essential to constrain

the temperature change and reduce the thermal influence for successful grinding of strong pyroelectric materials like LT crystal.

Fig. 6.12 showed another coolant temperature dependent response, the surface roughness, which is also closely related to the crack initiation. When coolant temperature decreased, the surface roughness became smaller, which in turn was a greater deal of resistance to the crack initiation and propagation. It was found that the R_a was kept less than 10 nm when the coolant temperature was as low as 5°C, and gradually increased and deviated from 20 nm to 50 nm. It can therefore concluded that the surface roughness was an alternative key factor significantly influencing on the quality of ground surface of pyroelectric crystals like LT wafers, including scratches, crack initiation and propagation.

6.2.3 Analysis and discussion

In order to determine the effect of grinding conditions on thermal influence, the above grinding results were analyzed by use of Design of experiment (DOE). The input factors and output responses were listed in Table 6.5, where three factors and two levels full factorial design (2^3 runs of test) was used. The effect of each factor and their interaction on the increasing rate of grinding torque was shown in Fig. 6.13 (a). It can be seen that the highest effect is given by the coolant temperature and followed by the wheel type, while the effect of the substrate is negligible. This result suggested that the low coolant temperature significantly suppresses the pyroelectric effect of LT. The heart type wheel, on the other hand, benefited from its geometry in effective cooling and self-sharpening. The same results also can be found from Fig. 6.13(b), where the effect of each factor and their interaction on the surface roughness was shown. The coolant temperature and the wheel type, again, stood out as the two major factors. Low coolant temperature and heart-type wheel contributed in better surface roughness after grinding.

According to the above results, the coolant temperature and wheel tooth geometry are two most effective factors influencing on the increasing rate of grinding torque and wafer surface roughness after grinding, which in turn dominate the performance of LT wafer grinding. Low coolant temperature is able to constrain the change in temperature

Table 6.5 Design of experiments

Parameters	Description	Test settings		Output (Y)
		-	+	Increasing rate
X_1	Wheel type	Heart	Segment	
X_2	Substrate	Glass	Al	Roughness
X_3	Temperature (°C)	5	25	
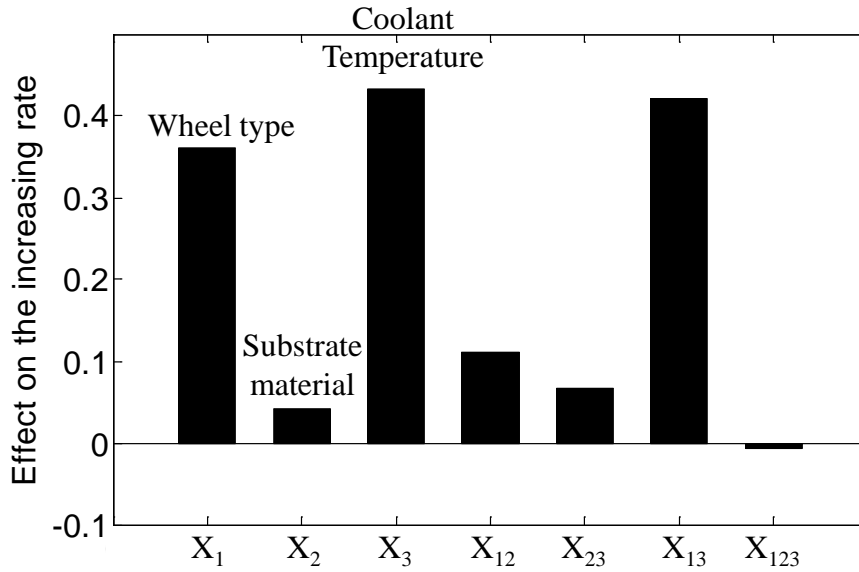
(a) Effect on the increasing rate
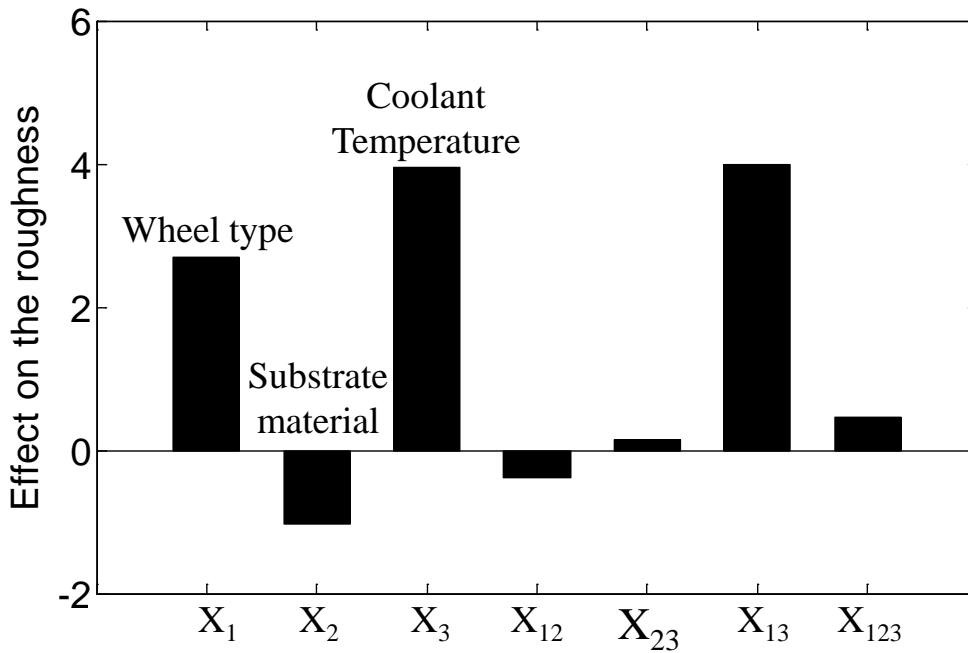
(b) Effect on the roughness

Fig. 6.13 Effect analysis on increasing rate of grinding torque and surface roughness

and the pyroelectric effect of LT crystal, while the heart-type wheel helps to further reduce the grinding heat and thermal influence by its effective cooling and self-sharpening ability. On the other hand, the themal conductivity of substrate has little effect on either the increasing rate of grinding torque or the surface roughness. One possible reason may come from an fact that the thermal conductivity of LT wafer itself is extremely low. Another possible reason is thermal conductivity of bonding wax which between the wafer and substrate is also very low.   Therefore, the heat was transferred out through the substrate was very limited.

6.3 Experimental details of grinding with electrolyte coolant

In order to suppress the piezoelectric and pyroelectric effects induced polarization during grinding of LT, the use of electrolyte solution was carried out in this section. The Fig. 6.14 is the schematic illustration of function of electrolyte solution. As shown in Fig. 6.14(a), the internal electrical field is induced and accumulated by polarization during the grinding process. By the application of electrolyte solution in the grinding process as shown in Fig. 6.14(b), the internal electrical field will has a short circuit and these positive and negative charges are neutralized.

6.3.1 Experimental details

The grinding tests with electrolyte coolant were conducted on a UPG-150H, as shown in Fig. 6.15 (a), which is also ultra-precision face grinding machine specially designed for wafer process. Based on the previous results of this chapter, as shown in Fig. 6.15(b), heart type diamond wheel was employed for grinding experiments. As shown in Fig. 6.14(c), four-inch (100 mm diameter) LiTaO$_3$ wafers which thickness ranging 300 to 320 μm were used as work-pieces. The CH$_3$COOH solution was chosen

(a) Polarization

(b) Short circuit
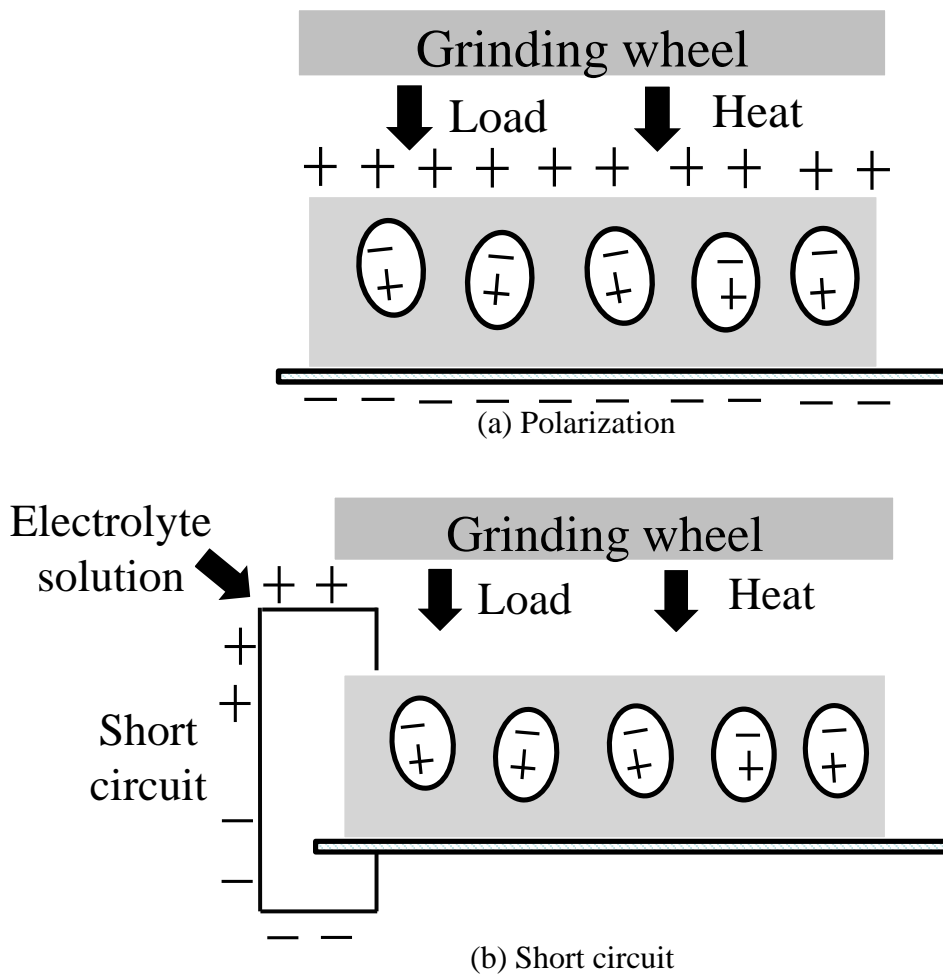
Fig. 6.14 The schematic illustration of the use of electrolyte solution

(a) Grinding machine

(b) Heart type grinding wheel
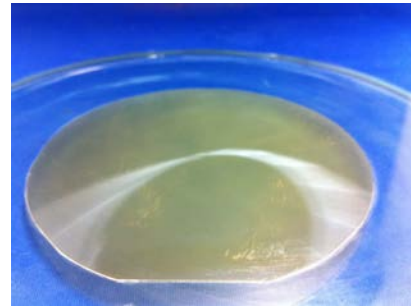
(c) 4 inch LT wafer

Fig. 6.15 Test instruments

as the coolant because of its high solubility. The coolant temperature was purposely controlled at 5°C.

   With the same machining procedure, the diamond wheels were conditioned on-machine by a very soft GC ring (a Green SiC wheel). The LT wafer adhered rigidly to substrate was mounted on the porous ceramic vacuum chuck. During face grinding, the grinding wheel and wafer were half overlapped and rotated at their own rotational axes simultaneously, while he diamond wheel was moved towards the wafer at a specified feed rate. Instead of grinding force, the grinding power was monitored and recorded through the inverter of wheel spindle. The surface roughness of ground wafers was measured by use of an optical surface interferometer (Zygo NewView 200). The rest test conditions were listed in Table 6.6.

Table 6.6 Test conditions

Parameters		Test settings					
Grinding wheel		SD3000C160V Heart type diamond					
Concentration	[Vol.%]	0	0.1	0.2	0.3	0.4	0.5
Electrical conductivity	[μs/cm]	182	218	282	313	382	452
Grinding wheel speed n_s [rpm]		1200					
Work piece speed n_w [rpm]		50					
In-feed $\varDelta$ [μm]		70					
Feed rate f [μm/min]		2					
Work-piece		4 inch LiTaO$_3$ wafer					
Coolant		CH$_3$COOH solution					
Temperature T [°C]		5					
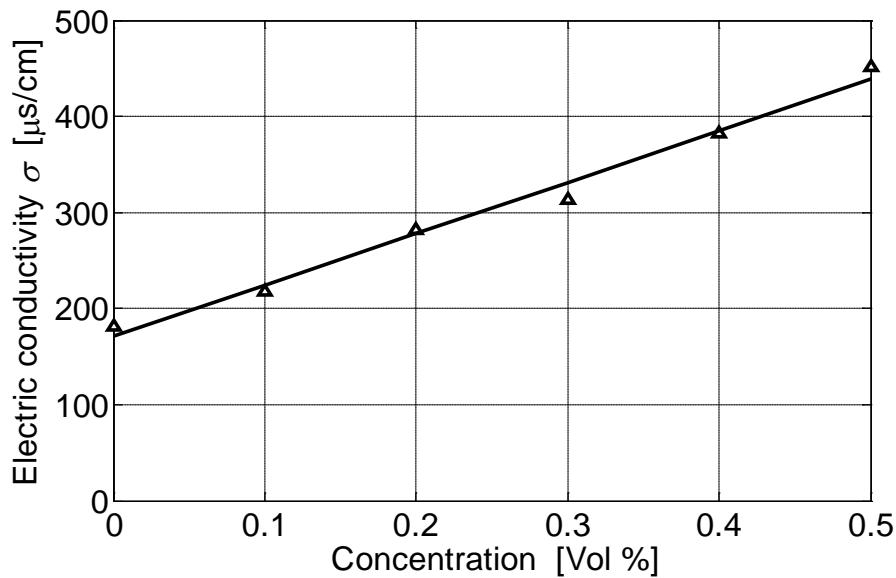
Fig. 6.16 The relationship between concentration and electrical conductivity

The Fig. 6.16 is the relationship between concentration and electrical conductivity. As shown in Fig. 6.16, the electrical conductivity has a linear relationship with the concentration of CH$_3$COOH solution. Because of the huge consumption of coolant used in the experiments, the concentration of coolant is used less than one percent. Hence, the electrical conductivity of coolant varies between 182-452 μS /cm.

6.3.2. Grinding results
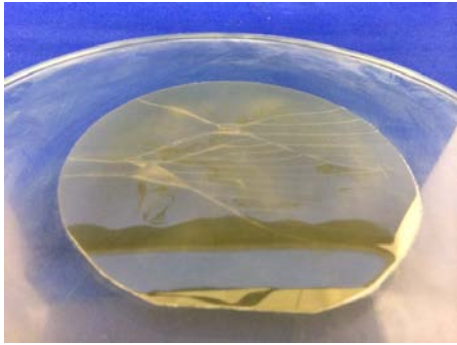
Con. =0%   Broken
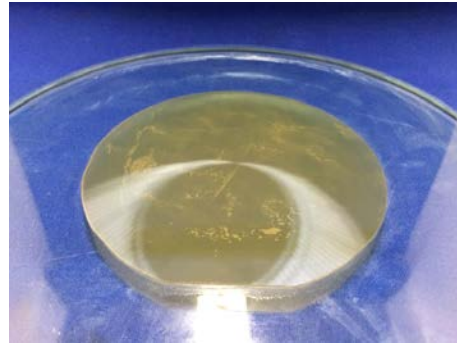
Con. =0.1%   Successfully
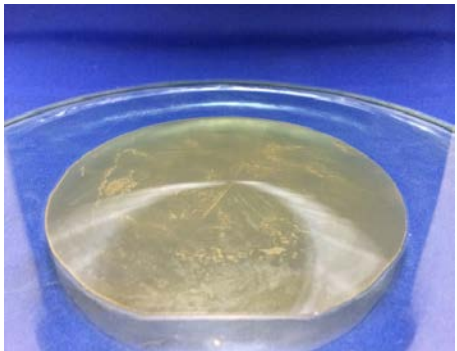
Con. =0.2%   Successfully
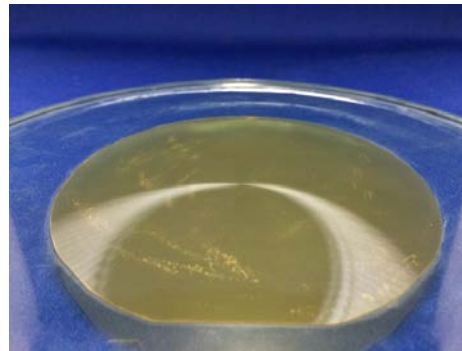
Con. =0.3%   Successfully
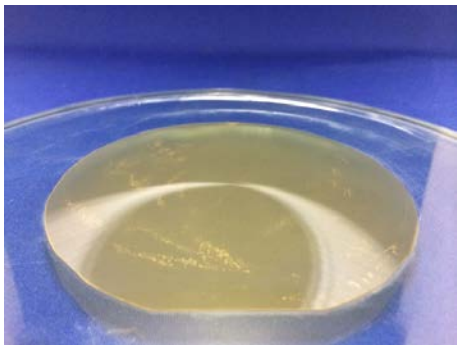
Con. =0.4%   Successfully

Con. =0.5%   Successfully

Fig. 6.17 Ground wafers in the experiments with different concentration of electrolyte coolant
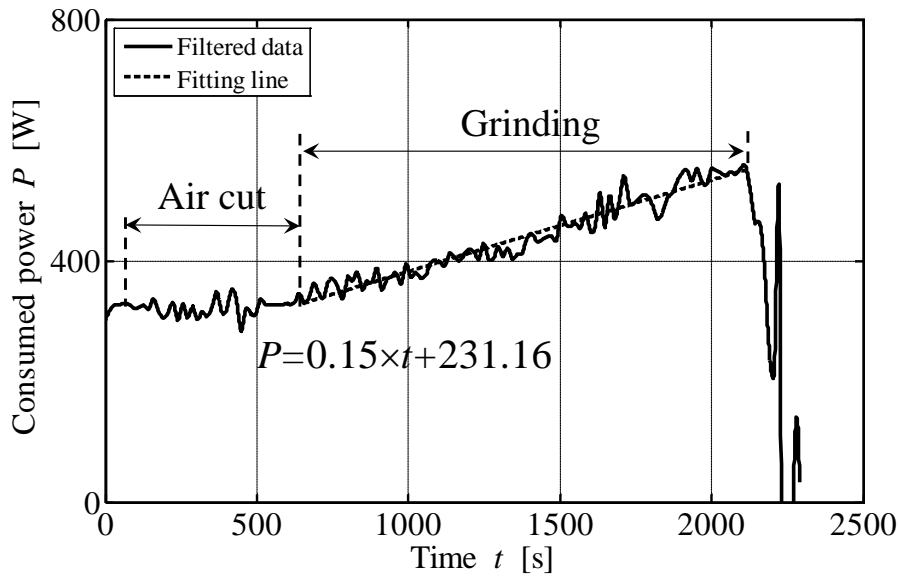
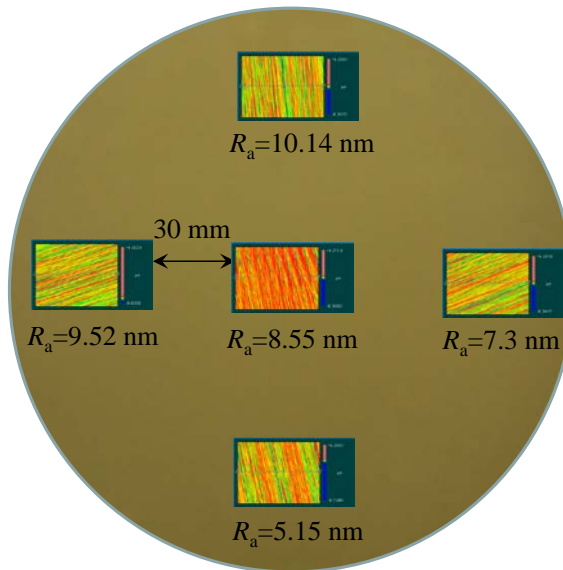(a) Concentration =0 [Vol. %] and Electrical conductivity=182 [μs/cm]
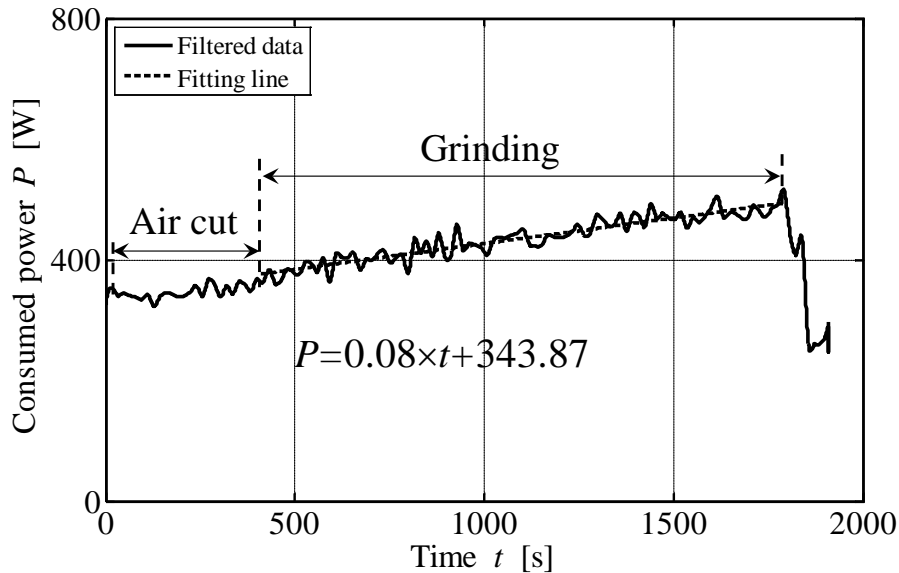
(b) Concentration =0.4 [Vol. %] and Electrical conductivity=382 [μs/cm]

Fig. 6.18 The consumed power P vs. Time T

Shown in Fig. 6.17 were typical external view of LT wafers ground in this research. When there is no electrical solution used in coolant, the cracks were observed on two tests. When electrical solution used in coolant, the other LT wafers were ground successfully, neither cracks no scratches were observed on their surfaces.

Showed in the Fig. 6.18 (a) and (b) were typical filtered results of consumed power vs. time which were obtained from grinding process with different concentration. Due to the high frequency inverter used for the grinding machine, the raw data of grinding power varied significantly, thus was filtered prior to the detailed analysis. As same as the previous analysis method, the slope of grinding power was equivalent to the increasing rate of tangential grinding force, which is a very important index to evaluate

Concentration =0 [Vol. %], Electrical conductivity=178 [µs/cm] and R_{ave}= 8.13 [nm]
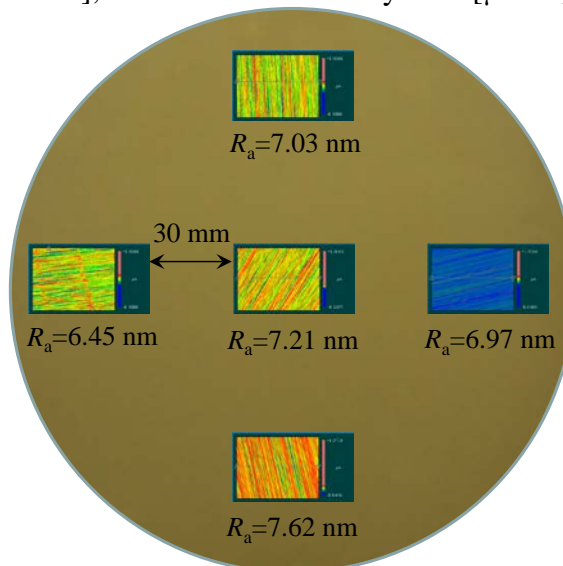
Concentration =0.4 [Vol. %], Electrical conductivity=382 [µs/cm] and R_{ave}= 7.06 [nm]

Fig. 6.19 The typical ground topographs

Table 6.7 The summary of experimental results

Concentration [Vol. %]	Electrical conductivity [µS/cm]	Increasing rate K [W/min]	Surface roughness R_a [nm]
0	178	9	9.13
0.1	218	7.2	6.69
0.2	282	4.8	6.73
0.3	313	6.6	7.72
0.4	382	4.8	7.06
0.5	452	4.7	6.5

the dynamic behavior of grinding wheel. The increasing rate of consumed power were 0.15 and 0.08[W/s] refer to the electrical conductivity of electrical solution is 178 and 382[μs/cm] respectively. As shown is Fig. 6.16, when the increasing rate of consumed power is 0.15[W/s], the cracks were observed on the LT wafer. It was also noted that the increasing rate is important key which dominates the grinding performance.

Shown in Fig. 6.19 were typical ground surface topographies of LT wafers with the electric conductivity is 178 and 382[μs/cm] which were measured by Zygo. The surface roughness was measured at five different positions on each ground LT wafer. Each position is distanced about 30 mm.

Table 6.7 was the summary of grinding results obtained at different test conditions. When the concentration varied from 0 to 0.5%, the electrical conductivity increased from 182 to 452 μs/cm, the increasing rate of consumed power was decreased from 9 to 4.8 W/min and the surface roughness was improved from 5.69 to 11.9 nm.

6.3.3. Analysis and discussion

Fig. 6.20 showed the relationship between increasing rate and electrical conductivity. As same as the results in the previous section, it was easy to understand that the increasing rate is a key factor which dominates the wafer grinding performance. When the increasing rate was above 8 W/min, cracks were initiated and resulted in wafer broken. When the increasing rate was below 8 W/min, these ground LT wafers were ground successfully. And when the electrical conductivity increased from the electrical conductivity increased from 178 to 452 μs/cm, the increasing rate decreased from 9 to 4.8 W/min, and the propagation of cracks were obviously suppressed when the electrical conductivity across the threshold line around 200 μs/cm even the
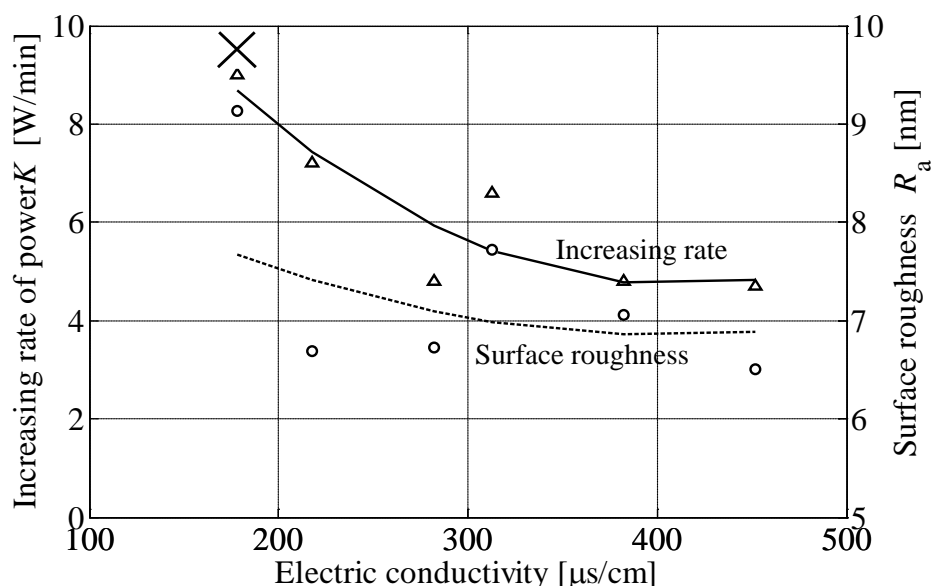

Fig. 6.20 The increasing rate K and surface roughness R_a vs. Electrical conductivity
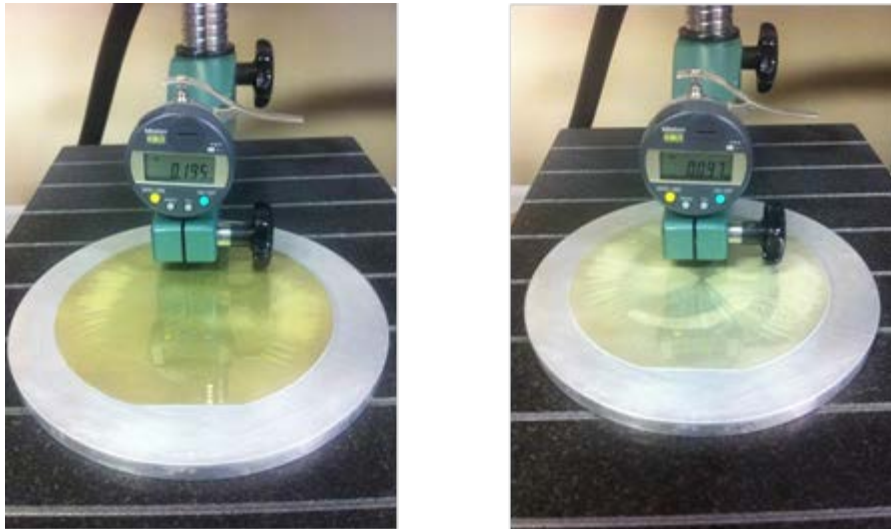
Fig. 6.21 The grinding results of LiTaO$_3$

increasing rate was above 0.1 W/min. The influence of increasing rate on LT grinding performance was suppressed. The possible reason may come from a fact that the influence of physical properties was suppressed with the increase of electrical conductivity. Therefore, the application of electrolyte solution present obviouse improve LT grinding performance.

The Fig. 6.20 also shown the surface roughness R_a vs. Electrical conductivity. When the electrolyte solution was used as a coolant, the surface roughness of LT was decreasd with the increase of electric conductivity. As the decription in the last section, surface roughness was also a key fators which dominate the wafer grinding results. The possible reason may also come from that the influence of physical properties on surface roughness was suppressed by the use of electrolyte solution.

Following the effective cooling method and the use of electrolyte solution which were introduced in this chapter. As shown in Fig. 6.21, the LT wafer was finally ground successfully with the thickness less than 100μm.

6.4 Summary

The content in this chapter is firstly focuses on the physical properties of LT like piezoelectric and pyroelectric effects and their influence on grinding performance. In order to suppress the piezoelectric and pyroelectric effects induced by polarization during grinding of LT, control of coolant temperature and use of electrolyte solution are were purposely tried in this chapter. The obtained results are discussed and summarized as follows:

(1) According to the theoretical analysis, for LiTaO$_3$, the cracks were possible to generated by internal stress resulted from joint effect of piezoelectric and pyroelectric properties.

(2) According to the results of grinding tests with effective cooling method, it can be concluded that the increasing rate of grinding torque (or force) and surface roughness are two key factors which dominate the wafer grinding performance, including scratches, cracks and wafer breakage.

(3) The joint effect of physical properties has an obvious influence on increasing rate and surface roughness.

(4) With the application of effective cooling methods and electrolyte solution, the influence of joint effect of physical properties on increasing rate and surface roughness was obviously suppressed.

References

[1] Holler, F. James; Skoog, Douglas A; Crouch, Stanley R. Principles of Instrumental Analysis. *Cengage Learning*, (2007), pp. 9.

[2] Harper, Douglas. "Piezoelectric". *Online Etymology Dictionary*.

[3] Manbachi, A. and Cobbold R.S.C: "Development and Application of Piezoelectric Materials for Ultrasound Generation and Detection", *Ultrasound*, Vol. 19, Iss.4, (2011), pp. 187–196.

[4] Gautschi, G. Piezoelectric Sensorics: "Force, Strain, Pressure, Acceleration and Acoustic Emission Sensors", Materials and Amplifiers. *Springer*, (2002).

[5] Information on http://en.wikipedia.org/wiki/Piezoelectricity.

[6] J.-D. Aussel and J.-P Monchalin: "Precision laser-ultrasonic velocity measurement and elastic constant determination", *Ultrasonics*, Vol. 27, Iss. 3, (1989), pp. 165-177.

[7] Webster, John G: The measurement, instrumentation, and sensors handbook, (1999), pp. 32–113.

[8] Diverse observations de la physique generale:" Histoire de l'Académie des Sciences (1717).

[9] Yamada T, Iwasaki H and Niizeki N: "Piezoelectric and elastic properties of LiTaO3 tempersture characteristics", *Japan Journal of Physical*, Vol. 8, (1969), pp.1127-1132.

[10] N. Miyazaki and N. Koizumi: "Analysis of cracking of lithium tantalate (LiTaO3) single crystal due to thermal stress", *Journal of Material Science,* Vol.41, No.19, (2006), pp.6313-6321.

[11] W. Hang, L. Zhou, J. Shimizu, T. Yamamoto and J. Yuan: "Study on micronano-indentation of typical soft-brittle materials", *Key Engineering Material*, Vol.523-524, (2012), pp.7-12.

Chapter 7 Conclusion

As a typical multi-functional material, single crystal lithium tantalate ($LiTaO_3$ or LT) exhibits its excellent electro-optical, piezoelectric and pyroelectric properties. However, detailed summaries of its mechanical properties and machinability are not readily available yet. Hence, the objective of this Ph. D thesis is to characterize properties of LT crystal and understand its influence on the grinding process. The main conclusions are summarized as follows;

(1) Data analysis procedures

Aiming to determination of the mechanical property of LT, a new robust data analysis procedure is proposed for indentation tests. Following this data analysis procedure, the mechanical properties of materials can be computed accurately at μN ~ mN range of load which is essential for "soft-and-brittle" materials like LT. The experimental results proved that this procedure is not only valid for a variety of materials from hard-brittle to soft-ductile, but also robust and applicable to indenters with a certain geometry imperfection. The deviation from the estimated area functions to the ideal tip one provides a quantitative estimation of tip wear for diamond indenters.

(2) Characterization of LT

In order to clarify and understand the fundamental mechanical properties of LT, micro/nano indentation tests were conducted to evaluate elastic modulus, hardness and fracture toughness. After the discussion of materials classification, it is found that for most materials including metals, ceramics, crystals and amorphous, the hardness was found to have a simple power law relation with the elastic modulus and described as $H = E^n$. The power n is introduced as a new index which can be used to not only rank those materials in an order of hardness, but also categorize materials into groups of "ductile" or "brittle". Subject to their index n and K_{IC}, the "brittle materials" are able to be further classified into two sub-groups. Those engineered ceramics and sapphire who have $1 < K_{IC} < 10$ and $0.5 < n < 0.7$ belong to "hard-and-brittle" materials like sapphire, whereas amorphous and LT can be characterized as a new category of "soft-and-brittle" materials with $K_{IC} < 1$ and $0.2 < n < 0.5$. Silicon crystal fell at the boundary of these two sub-groups.

(3) Grinding of $LiTaO_3$

A grinding model has been proposed and established to derive the specific energy of material removal. And then, a series of grinding experiments were carried

86

out on LiTaO$_3$ and Si for the evaluation of specific energy of material removal. After discussed in association with results of indentation, it is found that the hardness of LT is only 83% of that of Si, however, the specific energy of LT is 147.46 J/mm^3 and 44% larger than that of Si which had a well agreed with the indentation results.   Both the grinding and indentation results indicated a fact that LT is so brittle that no or very limited extra energy was demanded to make the cracks propagate once the crack was initiated, while a certain extra energy was required for Si.   The increasing rate of consumed power played a very important role in the machining of LT.   When it was above critical line, cracks were initiated and resulted in wafer broken.   Compared with the grinding results of Si, the increasing rate in the LT grinding experiments had a linear relationship with the feed rate at the same experimental conditions which indicated a fact that the physical properties may play a more important role in the grinding process.

(4) Physical properties and Effective machining methods

Unlike our traditional knowledge about machining process, the mechanical properties are the key factors which dominate the machining performance.   The theoretical analysis provide strong supporting evidence that physical properties like pyroelectric and piezoelectric effect play more important role than its mechanical properties in crack initiation and propagation on LT surface.

In order to suppress the piezoelectric and pyroelectric effects induced polarization during grinding of LT, the use of effective cooling and electrolyte solution are purposely carried out in this thesis.   The results indicated that machining methods like control of coolant temperature and use of electrolyte solution was able to suppress the influence of piezoelectric and pyroelectric properties on LT grinding performance.   The thickness of LT wafers can be able to controlled less than 100 μm following these methods.

Acknowledgements

Thank you very much!   Wish you all the best in the future!

Wei Hang
Jan. 29 2014